

Received April 13, 2017, accepted April 24, 2017, date of publication May 8, 2017, date of current version July 31, 2017.

Digital Object Identifier 10.1109/ACCESS.2017.2702066

# A Smartwatch Step Counter for Slow and Intermittent Ambulation

**VINCENZO GENOVESE, ANDREA MANNINI, AND ANGELO M. SABATINI, (Senior Member, IEEE)**

BioRobotics Institute, Scuola Superiore Sant'Anna, 56127 Pisa, Italy

(Corresponding author: Andrea Mannini (a.mannini@santannapisa.it))

This work was supported in part by the EC Funded Project I-SUPPORT ICT-Supported Bath Robots under Grant H2020 PHC-19 643666).

**ABSTRACT** The ambulatory monitoring of human movement can provide valuable information regarding the degree of functional ability and general level of activity of individuals. Since walking is a basic everyday movement, automatic step detection or step counting is very important in developing ambulatory monitoring systems. This paper is concerned with the development and the preliminary validation of a step counter (SC) designed to operate also in conditions of slow and intermittent ambulation. The SC was based on processing the accelerometer data measured by a Gear 2 smartwatch running a custom wearable app, named ADAM. A data set of eight users, for a total of 80 trials, was used to tune ADAM. Finally, ADAM was compared with two different commercial SCs: the native SC running on the Gear 2 smart watch and a waist-worn SC, the Geonaute ONSTEP 400. A second data set of eight additional users for a total of 80 trials was used for the assessment study. The three SCs performed quite similarly in conditions of normal walking over long paths (1%–3% of mean absolute relative error); ADAM outperformed the two other SCs in conditions of slow and intermittent ambulation; the error incurred by ADAM was limited to 5%, which is significantly lower than errors of 20%–30% incurred by the two other SCs.

**INDEX TERMS** Accelerometer, elderly, inertial sensor, pedometer, smartwatch, step counting, walking, wrist.

## I. INTRODUCTION

Ageing of the population and the concurrent increase of the number of people who spend a large part of their daily time at home, motivates the development of ambulatory monitoring systems that are capable to evaluate the level of physical activity in conditions of restrained mobility [1]. Because of the importance of walking for a healthy lifestyle, step detection and counting is believed to convey valuable information about the complex relationships existing between health and physical activity [2].

A large number of devices and applications have been developed for the purpose of physical activity monitoring [3]–[5]. Accelerometry is the technology of choice for wearable devices to measure and assess physical activity, with several applications documented, including gait and balance quality evaluation for fall risk assessment [6], [7], sleep assessment [8], fall detection and prevention [9]. Albeit the importance of a reliable strategy for activity assessment in free living conditions for the elderly is widely recognized, the available technological solutions are not generally ready for deployment: there is not enough evidence to support the assumption that those solutions, validated by testing on young

adults data, can be used without proper consideration that elderly people move differently from younger people. Age related changes in gait patterns and characteristics such as speed or duration of walking episodes are known [10] and have been observed to affect inertial sensor data processing [11], [12]. Thus, dedicated strategies have to be designed and developed with the specific aim of an effective activity monitor for the elderly. In this paper, we moved a first step in this direction, by carrying out experimental tests in which young volunteers were asked to walk, with different styles and speeds, including slow and intermittent ambulation, so as to stress the capabilities of the novel step detection and counting method we propose. The method was implemented in a smart watch; its performances were compared with the ones given by the native app running in the device, and by a commercially available waist-worn step counter (SC).

## A. WEARABLE TECHNOLOGY FOR STEP COUNTING

An SC – the device used for recording the number of walked steps – counts each step by detecting the motion of the person's arm or hip and it is considered a valid option for assessing physical activity in research and practice [13], [14].

Differently from past switch-based devices, modern SCs are based on Micro-Electro Mechanical Systems (MEMS) accelerometers. There are several factors that can limit the accuracy of SCs, including placement site, intensity of walking, counting errors due to non-ambulatory activities [15]–[17]. The most common placement site of SCs is the waist: devices are attached to the waistband or belt by means of a clip. Measuring the acceleration in all directions in the three-dimensional space relieves the wearer from the need to accurately position the device in relation to an anatomical reference frame, which can be influenced by body fat and clothing [15], [17]. User comfort and acceptability are generally high, since the freedom of movement is not restricted and donning-doffing is easy and convenient. Whereas counting errors due to non-ambulatory activities may not be critical to their performance, waist-worn SCs are grossly inaccurate when the walking speed is low [1], [18].

Recent technological advances, in particular the development of mobile devices (namely, smartphones) that are endowed with inertial sensors, have motivated further research in the field. The problem with smartphone-based SCs is that the mobile devices are not necessarily taken in the same location at all times, and in the same position relative to the body (e.g., trouser pocket and bags) [19]. In contrast with waist-worn SCs, smartphone-based SCs are also more sensitive to the influence of non-ambulatory activities, albeit interesting results have been recently reported as for the recognition of activity and the estimation of spatio-temporal parameters of gait [20], [21]. Moreover, movements of the upper arm when the smartphone is carried in the hand are not necessarily correlated with walking. An interesting avenue of research concerns the creation of signal processing methods that can help reduce the sensitivity of step-counting algorithms to the issue of placement and non-ambulatory activities [19], [22], [23]. Anyway, in a similar fashion to waist-worn SCs, smartphone-based SCs suffer from accuracy degradations when the walking speed is slow. In the attempt to improve the performance of smartphone-based SCs, embedded MEMS gyroscopes have also been considered as an alternative to accelerometers [24].

## B. SMARTWATCH TECHNOLOGY FOR STEP COUNTING

The reluctance to accept and to routinely use new technologies is an important issue for the development of wearable sensor systems, such as activity monitors and SCs. Lack of interest or motivation in using them is highly predictive of later refusal. In this regard, a new generation of mobile devices may ease a change of habits. The compliance with the use of a device worn at the wrist (namely, a smartwatch) would be generally high, which is one reason for the increasing interest devoted to this technology. Recent works involving long-term monitoring in large cohorts of users highlighted that using wrist-worn sensor devices can grant longer wear times [25]–[27]. Moreover, smartwatches provide unprecedented opportunity for collection of large datasets of

continuous measurement of physiological parameters (e.g., heart rate, galvanic skin resistance and temperature), and activity-related data (e.g., built-in accelerometer recordings). All these data can be used for longitudinal monitoring of health status and for quantimetric self-tracking, as advocated by the Quantified Self movement [22], [28]–[31].

The problem of the reliability of measurements is cited as a major obstacle to a wider use of wearable health monitoring devices such as smartwatches. Not dissimilarly from smartphones, processing the accelerometer data from smartwatches for activity recognition is challenging because of the wrist gesticulation and variability in movement, compared with other placement sites such as waist or ankle [32]. The wrist may move differently during the same activity, depending on what is in the hand and what the hand is holding or stabilizing. It is expected that these difficulties may affect step counting using a wrist-worn SC, although arm movements are generally well correlated with leg movements during steady walking.

In the case of intermittent ambulation activities, a critical issue is the number of missed steps that may occur due to the irregular signal patterns from the built-in accelerometer, regardless of the placement site. For instance, consider the problem of estimating a few steps interspersed with frequent stops and restarts. In this scenario, acceleration peaks correlated with steps are expected to be distributed irregularly both in amplitude and in time; hence, any predictive mechanism embedded in the algorithm of step counting is likely to perform poorly, due to the difficulty to specify and match template patterns describing the events occurring during any single step. Another element of difficulty is that data windowing itself would be a critical process in conditions of slow and intermittent walking (low time-resolution issue) [19]. A wristwatch SC that would search for the periods inherent in the cyclical nature of walking would require indeed long signal windows for extracting, e.g., the frequency-domain features needed for step identification.

The literature existing on the application of wrist-worn accelerometry to the problem of step counting is still scarce, and scattered, especially in conditions of slow and intermittent ambulation, [33], [34]. This paper is an initial attempt to fill the gap. Previous research on smartphone step counting showed that frequency-domain or correlation approaches did not accrue substantial benefits compared with windowed peak detection (WPD) methods for step counting in conditions of normal walking [19]; on the other hand, WPD methods are easier to implement and present reduced computational loads. Therefore, we developed an adaptive WPD algorithm for wristwatch-based step counting using the built-in accelerometer of a commercial smartwatch. We compared the performance of the proposed algorithm, the native app running in the smartwatch for step counting, and a waist-worn commercial SC. Experimental tests included steady walking at several speeds, jogging, non-ambulatory activities, and intermittent and slow ambulation.

## II. EXPERIMENTAL SECTION

### A. SYSTEM DESIGN AND IMPLEMENTATION

The technological solution we propose and describe in this paper can be considered just as a module of a full suite of devices and algorithms of a multi-purpose Body Sensor Network (BSN) for monitoring and assessing (elderly) individuals involved in several of their daily-life activities, see Fig. 1. Within the framework of this platform, algorithms for fall risk assessment [30], gait and balance assessment [35], fall detection [36], activity recognition [32], [37] and gait alteration detection [38], [39] have been and currently being conceived and deployed.

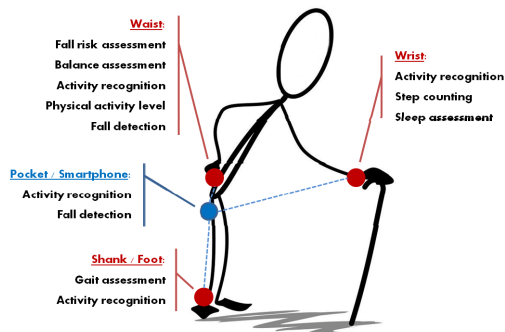


**FIGURE 1.** Multi-purpose BSN for monitoring and assessing (elderly) individuals in daily-life activities.

Given the scope of this paper, the development of a single sensor unit is targeted, aiming specifically at providing solutions to the problem of step counting. The smartwatch is thus just another node that was integrated in the BSN, with all sensor and processing resources needed to perform step counting.

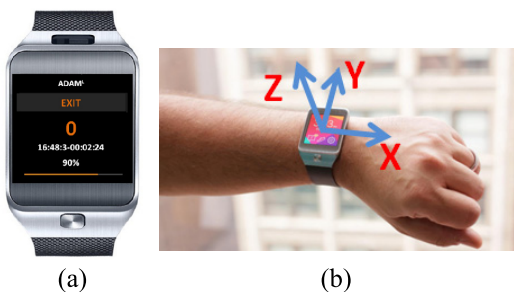


**FIGURE 2.** (a) The Gear 2 smartwatch used for ADAM development; (b) The mobile reference frame aligned with the sensitivity axes of the embedded accelerometer.

The developed algorithm was implemented in a wearable app named ADAM (Advanced Daily Activity Monitor) running on a commercial Tizen smartwatch (Gear 2, Samsung Electronics Co., Ltd.), Fig. 2. ADAM was written in HTML5 using the IDE Tizen SDK for Wearable (version 1.0.0). The smartwatch provided acceleration components  $a_x$ ,  $a_y$ ,  $a_z$  at the sampling frequency  $f_s = 25$  Hz (sampling interval  $T_s = 40$  ms), normalized to the gravitational acceleration  $g$ ,  $g = 9.81 \text{ m/s}^2$ , relative to the mobile reference frame shown

in Fig. 1b. Additionally, a tri-axial gyroscope was available to measure the angular velocity. However acceleration data only were included in the SC algorithm.

### B. EXPERIMENTAL PROTOCOL

Two sets of experimental trials were performed, with the aim to build one dataset for tuning the parameters needed by the step counting algorithm (training dataset), and another dataset for assessing its performance (testing dataset). Although field tests involving elderly users are surely needed for a thorough validation of the proposed approach, just two groups of healthy adult subjects participated in the preliminary experimental phase reported in this paper. All participants signed an informed consent before starting experimental sessions. Research procedures were in accordance with the Declaration of Helsinki. All subjects wore the Gear 2 smartwatch on the non-dominant hand wrist and a commercial SC (Geonaute ONSTEP 400), which was clipped to the waist belt at the right anterior iliac spine. During experimental sessions, subjects were free to wear their preferred shoes. Although the testing was not done in truly naturalistic conditions, we took care of minimizing experimental biases, by asking subjects to move as naturally as they could. Moreover, they did not receive verbal or any other feedback information about the SC output, only start and stop messages were issued to them. The device initialization required a 2-s interval when the subject was asked to stand still in the so-called neutral standing posture, which allowed to recognize whether the smartwatch was worn on the left or right wrist. Because of the absence of elderly participants in the subject pool, particular care was devoted to the definition of the experimental study protocol, which also involved conditions of slow and intermittent ambulation typical of walking habits of elderly people. After initialization took place, subjects were instructed to walk at their preferred speed (free-selected speed), slower, or much slower, than normal and faster than normal, being free to interpret the speed at their own convenience. An activity named “In-home task” was also considered, figure 3. The full set of activities considered for training ADAM and for testing ADAM, the Gear 2 and the Geonaute SCs, is reported in Table 1. The experimenter observed the participants while performing activities and counted the number of steps walked in each trial, so as to compute the reference step count  $N_{\text{ref}}$  used for algorithm performance assessment.

The training dataset included the accelerometer data acquired from group 1-subjects asked to perform the *Walk – turn – walk* activity, with all variants indicated in Table 1. Eight subjects (5 males and 3 females) participated in the training phase. Age ranged from 28 to 55 years ( $38.5 \pm 11.8$  years) and height from 160 to 185 ( $172.8 \pm 10.5$  cm). The testing dataset included the accelerometer data acquired from group-2 subjects asked to perform all activities in Table 1. Eight subjects (3 males and 5 females) participated in the testing phase. Age ranged from 29 to 54 years ( $37.2 \pm 9.7$  years) and height from 158 to 187 ( $172.1 \pm 9.5$  cm).

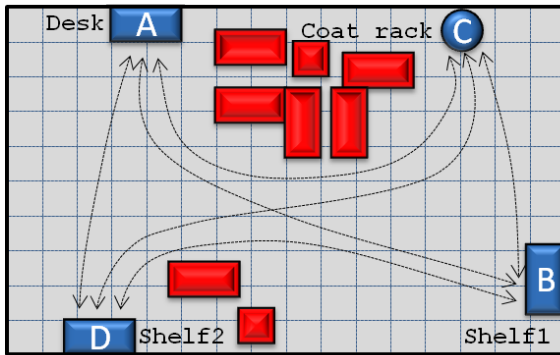


**FIGURE 3.** Room layout, with the furniture location for the In-home task activity. The red shapes are fixed obstacles to be avoided. The blue shapes are the target points. The grid size is 60 cm × 60 cm.

**TABLE 1.** Activity types and description.

Type	Description
Walk-turn-walk	Walk ten steps along a straight path, including a half-turn to walk ten steps in the opposite direction so as to return to the initial location (a rest of two seconds allowed before and after the half-turn). Repeat at four different speeds: slower than normal, normal (i.e., free-selected), faster than normal, jogging.
Slow and steady walk	Walk 500 steps at constant, slow speed (level walking); directional changes are allowed.
Variable-speed walk	Walk 500 steps at variable speed (level walking), with walking speed being freely changed (slower than normal, normal, faster than normal); directional changes and stops-starts are allowed.
Very slow walk	Walk 100 steps at very low speed (level walking), with minimal trunk and head oscillations; directional changes and stops-starts are allowed.
Jog	Jog 100 steps; directional changes and stops-starts are allowed.
Going up-and-down stairs	Climb a staircase of 11 steps (16-cm high), including a half-turn to the higher floor; walk downstairs along the same staircase, so as to return to the initial location.
In-home task	Subjects were asked to do a predefined sequence of actions in a structured room, walking at their own preferred speed (see Fig. 3): a) Take a box placed on the desk at point A and place it on the top of the shelf at point B ( $d = 7.8 \text{ m}$ ) b) Reach the coat rack at point C and pick up a bag ( $d = 3.6 \text{ m}$ ) c) Carry the bag on the top of a second shelf at point D using the smartwatch side arm ( $d = 8.4 \text{ m}$ ) d) Reach the shelf at point B and recoup the box ( $d = 7.2 \text{ m}$ ) e) Bring the box on the desk at point A ( $d = 7.8 \text{ m}$ ) f) Reach the shelf at point D and recoup the bag ( $d = 4.2 \text{ m}$ ) g) Carry the bag to the coat rack at point C using the left arm ( $d = 8.4 \text{ m}$ ) h) Reach the point A ( $d = 6.6 \text{ m}$ ) The distance walked in each section from a) to h) is denoted with d. Between each section, subjects were asked to rest for two seconds.

### C. THE STEP COUNTING ALGORITHM

A standard calibration procedure was employed to calibrate the built-in tri-axial accelerometer [40]. The computed values

of offset and scale factor along the three sensitivity axes were used to compensate for calibration errors before processing the accelerometer measurements by ADAM.

The acceleration magnitude

$$A_m = \sqrt{a_x^2 + a_y^2 + a_z^2} \quad (1)$$

was computed from the acceleration components. An 8-point moving average filter was applied to the acceleration magnitude, following a 3-point moving median filter, in the combined effort to remove the high-frequency noise and mitigate the effects of outlying measurements. If the absolute difference between the current sample and the previous sample at the output of the moving median filter was less than a small threshold ( $\lambda_M$ ), the current sample was clipped to the previous sample, yielding  $A_{mL}$ . A high-pass filtered version of  $A_{mL}$  was obtained, namely  $A_{mH}$ , by subtracting an 8-point moving averaged version of  $A_{mL}$  from  $A_{mL}$  itself. On a separate conditioning line, the acceleration components  $a_x, a_y, a_z$  were filtered using a 16-point moving average filter, yielding  $a_{xL}, a_{yL}, a_{zL}$ .

#### 1) DYNAMIC THRESHOLDING

In accordance to previous studies, we hypothesized that local maxima of the acceleration magnitude correlated with foot contacts at the beginning of each gait step, provided that such peak values were high enough and were not determined by acceleration measurement noise [41]. Hence, each peak of  $A_{mL}$  whose value exceeded some threshold value  $\lambda_D$  could increase the step count by one unit, depending on the outcome of the step validation procedure described in the following. We propose to determine the threshold value in on-line conditions (i.e., dynamic thresholding) by time-shifting  $A_{mL}$  of  $\tau_d = K_d T_s$  seconds and clipping its value to a prefixed minimum value (to reduce the effects of the device vibrating very rapidly or very slowly from a cause other than walking). The rationale behind this choice was explained, first, by analyzing the shortcomings of a popular means to compute  $\lambda_D$  [41]:

$$\lambda_D = \frac{\max \{A_{mL}\}_{\tau_w} + \min \{A_{mL}\}_{\tau_w}}{2}. \quad (2)$$

The adaptive threshold was computed as the arithmetic mean between the maximum and the minimum values of  $A_{mL}$  occurring in a signal window of length  $\tau_w$  that extended from the current  $A_{mL}$  sample backwards, respectively:  $\max \{A_{mL}\}_{\tau_w}$  and  $\min \{A_{mL}\}_{\tau_w}$ ; the threshold was then clipped to a minimum value  $A_{\min}$ . The peak was searched in the time interval from the positive crossing time (rising time), i.e., when  $A_{mL}$  crossed  $\lambda_D$  with positive slope, to the negative crossing time (falling time), i.e., when  $A_{mL}$  crossed  $\lambda_D$  with negative slope. In the example reported in Fig. 4,  $\lambda_D$  was computed over different time windows according to (2), and clipped to  $A_{\min}$  ( $A_{\min} = 1.033 \text{ g}$ ). When  $A_{mL}$  exceeded the dynamic threshold  $\lambda_D$ , the SC state was set to *armed* (*notarmed* otherwise).

In the example, it is noted that the step annotated as P4 was not detected when  $\tau_w = 1 \text{ s}$ , yielding a false negative in the

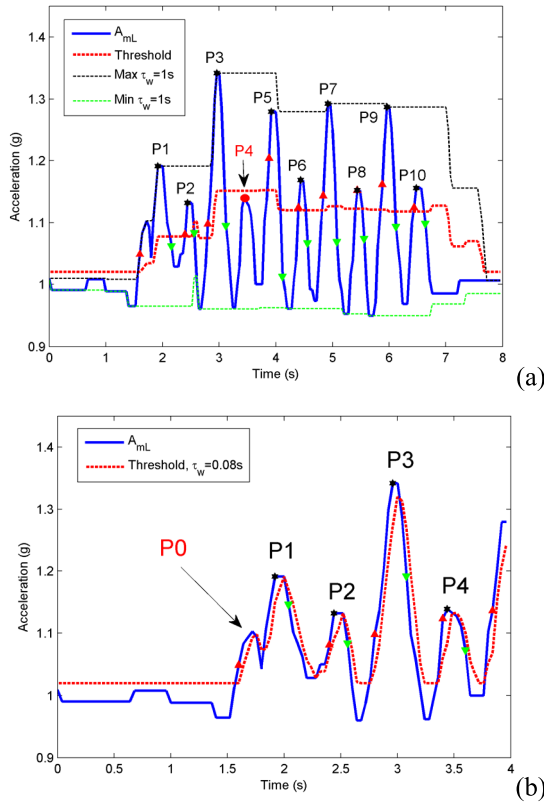


**FIGURE 4.** The time functions of  $A_{mL}$  (blue) and  $\lambda_D$  (red) are reported for a representative walking bout from activity Walk-turn-walk. (a)  $\tau_w = 1$  s; (b)  $\tau_w = 0.08$  s. Red and green triangular markers indicate the samples within which the dynamic threshold is crossed in rising and falling directions, respectively.

step detection process (Fig. 4a). This behavior was quite typical, especially when the peak values of  $A_{mL}$  differed markedly during consecutive steps, namely when left and right steps were not symmetric. Slight asymmetries are typical even of healthy gait as highlighted by analyzing data from waist-worn sensors [42] and they are likely to exist as far as the motion of the upper arm is considered. Intermittent ambulation (e.g., frequent stops and starts, abrupt directional changes) would further exacerbate the problem. In the effort to make the dynamic threshold adapting faster to the signal shape,  $\tau_w$  could be reduced, as in Fig. 4b, where  $\tau_w = 0.08$  s. The peak at P4 was correctly detected, however we observe a false positive occurring in the case of the peak at P0. It is also noted that reducing the window's length  $\tau_w$ , the time function of the dynamic threshold  $\lambda_D$  tended to a delayed replica of  $A_{mL}$ . Let us suppose that the time window was narrowed down to the point when  $\tau_w = T_s$ , in which case the dynamic threshold turned out to be  $A_{mL}$  delayed by one sample. Following the reasoning above, the algorithm would become highly responsive, with the consequence that several false positives might arise, especially when the (wrist) acceleration patterns were irregular. In our WPD implementation, our proposal was to design the dynamic threshold using a deliberate time-shift of  $A_{mL}$  by  $K_d > 1$  samples, in the effort to avoid proliferation of false positives, whilst retaining

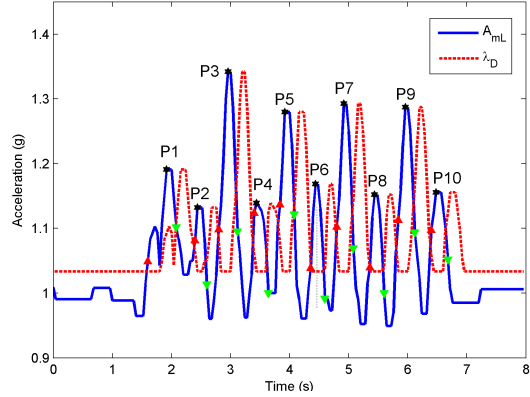


**FIGURE 5.** The time functions of  $A_{mL}$  (blue) and  $\lambda_D$  (red) are reported for the same walking bout from activity Walk-turn-walk in Fig. 4.

good adaptation properties. Hence,  $\lambda_D$  was computed as the clipped (to  $A_{\min}$ ) and time-shifted (by  $\tau_d = K_d T_s$  seconds) replica of  $A_{mL}$ . We hypothesize that this approach may ensure fast adaptation to any change of the underlying signal shape. Fig. 5 shows the results for the same example as in Fig. 4:  $\lambda_D$  was computed by delaying  $A_{mL}$  by four samples, and the result was then clipped to  $A_{\min}$ .

In this particular example, the peak at P4 was correctly detected, without introducing false positives in the step detection process. However, successful peak identification did not imply that the step count be increased necessarily by one unit; the detected step-related event must be further validated for achieving better robustness to false positives. In preparation for the step validation phase, the following quantities were computed. The step time, expressed in seconds, was computed as the difference between successive occurrences of the  $A_{mL}$  peaks that were identified by dynamic thresholding. The cadence, expressed in Hz, was computed by inverting the average step time, which was estimated from a specified number of step times. Finally, the Root Mean Square of  $A_{mH}$  (RMS<sub>H</sub>) was calculated in a window of length  $\tau_s$  extending backward from the current sample of  $A_{mH}$ .

## 2) STEP VALIDATION

The step validation was intended as a set of algorithmic prescriptions used to reduce the rate of wrong detections incurred by the step-counting process. In particular simple heuristics were implemented, which helped improving performance by enforcing reasonable constraints of walking [43]. Throughout the various stages of the step validation process, the SC status was determined based on the values of two parameters: the total number of steps counted since the beginning of the current counting process ( $N_{step}$ ), and the number of peaks that were recognized as valid, up to the current time ( $Cont_{step}$ ) since last stop. A block scheme of the proposed algorithm is reported in figure 6.

The set of rules and the related parameters as implemented in the block scheme are illustrated in Table 2 and briefly explained in the following. In particular, on a sample-by-sample basis, Rule #1 was applied to avoid false

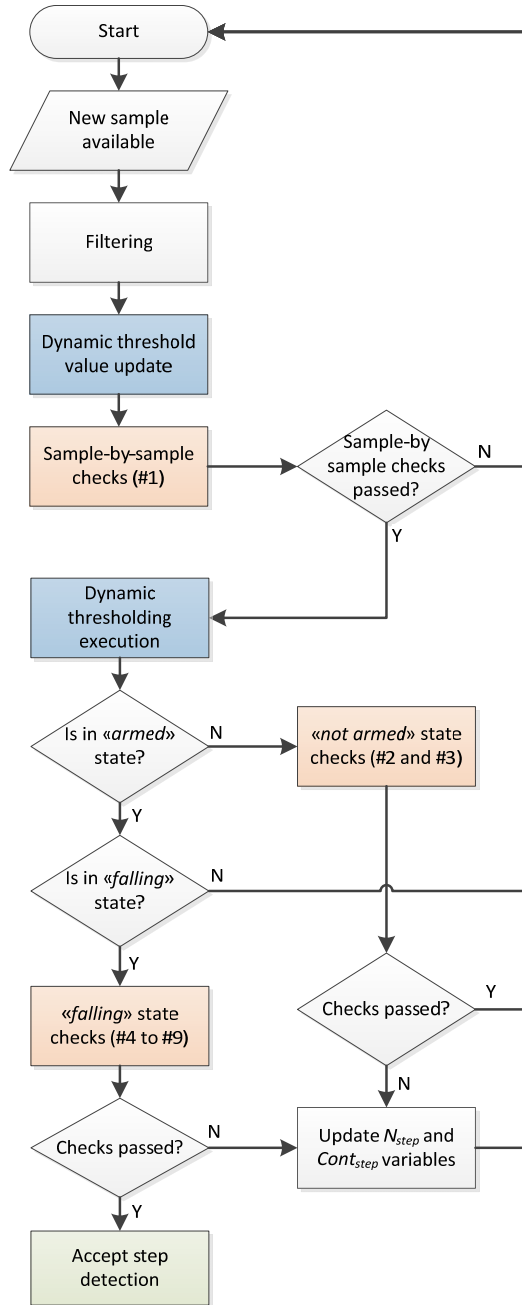


**FIGURE 6.** Block diagram showing the algorithm of step validation in action. Blocks colored in blue refer to dynamic thresholding, blocks colored in orange refer to different stages of the step validation procedure. The numbers reported within the orange blocks correspond to the IDs of the rules described in Table 2.

positives that were likely to occur due to arm swinging during the last step before a walk stop:  $A_{x,min}$ ,  $A_{y,min}$ ,  $A_{z,min}$ ,  $A_{z,max}$  were the values of thresholds applied to single acceleration data channels, tuned to discard signals that were not compatible with the walking-related arm swing. A second group of rules (#2 and #3) was applied in the case when dynamic thresholding indicated an “armed” condition, i.e. the threshold was crossed upwards, but it was not yet crossed in the opposite direction. Rule #2 reset the  $Cont_{step}$  value to zero in

**TABLE 2.** Step validation rules.

Rule ID	Description	SC state
1	Suspend thresholding if $Cont_{step} \geq 2 St_{min}$ , or the step counter is armed or one of the following four conditions is satisfied: $a_{xL} \geq A_{x,min}$ $a_{yL} \leq A_{y,min}$ $a_{zL} \geq A_{z,min}$ $a_{zL} \leq A_{z,max}$	Sample by sample
2	If the time elapsed from last valid step ( $ElapsedTimeFromLastStep$ ) exceeds $Tst_{max}$ , then $Cont_{step} = 0$	Not armed
3	If the following conditions are satisfied: 1. $RMS_H \geq St_{RMS}$ 2. $ElapsedTimeFromLastStep \geq Tst_{max}$ 3. $Cont_{step} \geq St_{min}$ 4. $N_{step} > 0$ then $N_{step} = N_{step} - 1$ , and $Cont_{step} = 0$	Not armed
4	Wait updating $N_{step}$ until $Cont_{step} \geq St_{min}$	Falling
5	If step time $\leq Tst_{min}$ or step time $\geq Tst_{max}$ , then $Cont_{step} = 0$	Falling
6	If cadence $\geq Stf_{max}$ , then $Cont_{step} = 0$ (cadence is computed from the last $St_{min}$ steps)	Falling
7	If $\max(A_{mL}) \geq Acc_{max}$ , then $Cont_{step} = 0$	Falling
8	If $\max(A_{mL}) \leq Acc_{min}$ , then $Cont_{step} = 0$	Falling
9	If $A_{mL}$ exceeds $\lambda_D$ for a time less than $\Delta T$ , then $Cont_{step} = 0$	Falling

case of long time intervals elapsed from the last valid step, based on the threshold  $Tst_{max}$ . Rule #3 detected sudden stops of walking and was designed to reject false positives related to arm swinging occurring in the course of the last step before a walk stop. In order to detect such conditions a joint check was carried on the  $RMS_H$  of the signal by means of the  $St_{RMS}$  threshold, on the time elapsed from the last step (threshold  $Tst_{max}$  as in Rule #2), on the value of  $Cont_{step}$  (this had to be greater than its minimum value  $St_{min}$ ) and on the value of  $N_{step}$ .

Rules from #4 to #9 acted at the time instant of step detection, which occurred when the dynamic threshold was crossed downwards (“falling” state, see figure 7). Depending on the outcome of rules from #4 to #9, we were in the position to accept the step or not. Rule #4 was related to the assumption that a steady walking activity required at least some consecutive steps to occur [41]. In particular, the update of the  $N_{step}$  value was inhibited until  $Cont_{step}$  value reached the threshold value  $St_{min}$ . Rules #5 and #6 coded the intuitive notion that a gait step cannot have abnormal durations (neither too long nor too short), and must be characterized by a significant acceleration footprint [43]. These rules were driven by the parameters  $Tst_{max}$ ,  $Tst_{min}$  (maximum and minimum step time),  $Stf_{max}$  (maximum cadence),  $Acc_{max}$  (maximum value of  $A_{mL}$ ),  $Acc_{min}$  (minimum value of  $A_{mL}$ ) and  $\Delta T$  (minimum duration of a step-related acceleration burst).

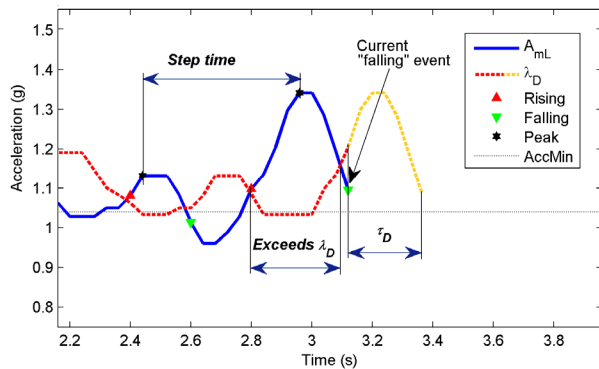


**FIGURE 7.** Schematic description of parameters used in the step validation rules that were applied in the “falling” state (green marker). In particular, rules #5 and #6 of Table 2 were applied to stride time and cadence evaluated starting from peaks (black markers), rules #7 and #8 referred to the amplitude of the signal ( $Acc_{min}$ , black dashed line),  $Acc_{max}$  is not reported (2.5 g). Rule #9 was applied to the time interval in which  $A_{mL}$  exceeded the dynamic threshold  $\lambda_D$  (red dashed line). In orange, the dynamic threshold that will be applied to the  $K_d$  samples of the  $A_{mL}$  signal following the current sample.

**TABLE 3.** Input parameters of ADAM.

Processing	
$\lambda_M, g$	0.017
Dynamic thresholding	
$K_d$	4
$A_{min}, g$	1.033
Step validation	
$St_{min}$	6
$Tst_{min}, s$	0.30
$Tst_{max}, s$	1.50
$Sf_{max}, Hz$	3.00
$A_{x,min}, g$	0.25
$A_{y,min}, g$	0.15
$A_{z,min}, g$	-0.36
$A_{z,max}, g$	0.80
$Acc_{max}, g$	2.50
$Acc_{min}, g$	1.04
$T, s$	0.12
$\tau_s, s$	3.00
$St_{RMS}, g$	0.08

#### D. ALGORITHM TRAINING

As explained in the Experimental Protocol section, two datasets (with different subjects involved in each) were considered for the purpose of training and testing the algorithm. In addition to the activities prescribed by the protocol in Table 1, we performed several other tests with the subjects wearing the smartwatch; they were asked to freely perform sedentary activities (i.e., answering phone calls, drinking, typing a keyboard, gesticulating while speaking) and exercise breaks (i.e., outstretching the arms in different spatial orientations) – total recording time: 30 min per subject.

The training procedure was then implemented in two steps. First, the parameters, whose actual setting was verified to significantly affect the algorithm performance, namely  $\lambda_M$ ,  $K_d$ ,  $A_{min}$  and  $St_{min}$ , were identified. The remaining parameters were given default values that were found acceptable in the current scenario. In the second step, the parameters

**TABLE 4.** Number of complete failures for each method.

Activity	ADAM	Samsung SC	Geonaute SC
Walk-turn-walk (slow)	0	3	8
Walk-turn-walk (normal)	0	3	8
Walk-turn-walk (fast)	0	6	8
Walk-turn-walk (jogging)	0	5	7
Slow and steady walk	0	0	0
Variable-speed walk	0	0	0
Very slow walk	0	4	2
Jog	0	0	0
Going up-and-down stairs	0	0	0
In-home task	0	0	5
Total	0/80	21/80	38/80

$\lambda_M$ ,  $K_d$ ,  $A_{min}$  and  $St_{min}$  were tuned offline by implementing a grid search for determining their optimal value. Empirically, we verified that they were important in determining the algorithm performance, especially the time delay  $K_d$ , which turned out to be the essential element of the proposed WPD method. Compared with the case when  $K_d = 4$ , a too small value tended to increase the detection sensitivity at the expense of the specificity; conversely, a too high value (say,  $K_d > 8$ ) tended to improve the detection specificity, at the expense of the sensitivity. Overall, the parameter setting we choose (Table 3) turned into 100% specificity, including analysis of data from sedentary activities and exercise breaks. It goes without saying that the native Samsung SC accumulated several counts in the same situation where ADAM was not affected by false positives.

#### E. METRIC OF PERFORMANCE

The Count Error ( $CE$ ) was defined as follows ( $i$ -th activity,  $j$ -th subject):

$$CE(i, j) = N_{step}(i, j) - N_{ref}(i, j), \quad i = 1, \dots, 10; j = 1, \dots, 8. \quad (3)$$

The Mean Absolute Relative Error ( $MARE$ ) was also considered as performance metric:

$$MARE(i) = 100 \cdot \frac{1}{8} \sum_{j=1}^8 \left| \frac{CE(i, j)}{N_{ref}(i, j)} \right|, \quad i = 1, \dots, 10. \quad (4)$$

$CE$  and  $MARE$  are the metrics to investigate the accuracy of the three SCs. Henceforth, the term *complete failure* will be used to denote when one method was 100% inaccurate, in the sense that it could not register any valid step in a particular activity.

#### III. RESULTS AND DISCUSSION

ADAM was trained using the  $CE$ -statistics generated from the training dataset. Table 3 shows the resulting setting of the input parameters needed by the algorithm. Table 4 reports the data concerning the complete failures of each SC. Not surprisingly, the Geonaute SC performed worse in conditions when the number of consecutive steps walked before any stop was not high enough for step validation (*Walk-turn-walk* and *In-home task*); moreover, it suffered from

**TABLE 5.** Statistics of the performance metric CE.

Activity	ADAM				Gear SC				Geonaute SC			
	Mean	Max	Min	Std	Mean	Max	Min	Std	Mean	Max	Min	Std
Walk-turn-walk (slow)	0.7	4	-1	1.5	-3.0	-2	-4	1.0	NA	NA	NA	NA
Walk-turn-walk (normal)	0.6	3	-1	1.4	-1.8	1	-4	2.1	NA	NA	NA	NA
Walk-turn-walk (fast)	1.0	4	-2	2.0	-1.0	-1	-1	0.0	NA	NA	NA	NA
Walk-turn-walk (jogging)	2.7	7	-3	3.2	2.3	7	-7	8.1	4.0	4	4	0.0
Slow and steady walk	-4.9	3	-20	7.1	-4.5	0	-17	5.5	-4.8	3	-18	8.3
Variable-speed walk	-11.1	18	-84	30.9	-4.6	23	-50	20.8	4.4	36	-10	14.1
Very slow walk	-2.9	8	-17	7.1	-21.5	0	-76	36.4	-30.0	1	-82	38.5
Jog	0.0	5	-3	2.8	-5.5	15	-63	24.0	4.0	17	-4	6.4
Going up-and-down stairs	-0.1	3	-2	1.6	-1.3	1	-4	2.1	0.8	3	0	1.0
In-home task	-5.5	1	-26	9.0	-10.5	10	-42	19.0	-61.0	2	-103	55.6

**TABLE 6.** Values of the performance metric MARE.

Activity	ADAM	Samsung SC	Geonaute SC
Walk-turn-walk (slow)	5	15	NA
Walk-turn-walk (normal)	6	11	NA
Walk-turn-walk (fast)	9	5	NA
Walk-turn-walk (jogging)	18	35	20
Slow and steady walk	1	1	1
Variable-speed walk	3	2	2
Very slow walk	5	21	30
Jog	2	12	5
Going up-and-down stairs	2	3	2
In-home task	6	17	61

some difficulties even during the activity *Very slow walk*. The explanation is that the factory calibration of the Geonaute SC was likely tailored to continuous walking at free selected walking speeds. The Samsung SC performed better than the Geonaute SC in our experiments, with the exception of the *Very slow walk* activity. The same comment concerning the factory calibration is pertinent to explain the behavior of the Samsung SC.

Limiting the statistical analysis to the trials in which the methods did not undergo complete failure, Table 5 reports the *CE* statistics for each activity, averaged across subjects (mean value, standard deviation, minimum value, maximum value). The two commercial devices, particularly the Samsung SC, tended to undercount steps, especially when the walking conditions differed to some extent from those assumed for the factory calibration. Conversely, ADAM performed acceptably. Due to an outlying subject performing the *Variable-speed walk* activity, namely one subject for which ADAM heavily undercounted steps, the mean error and the standard deviation were slightly greater than those achieved by the two other methods.

Finally, Table 6 reports the *MARE* values scored by the three SCs. The three tested SCs performed similarly during the extended walks of *Slow and steady walk*, *Variable-speed walk* and during *Going up-and-down stairs*; conversely, ADAM outperformed the two other step counters in all conditions when the movement was very slow (i.e., during *Very slow walk*) and more intermittent [*Walk-turn-walk* (except jogging) and *In-home task*]. *Walk-turn-walk (jogging)* was the only activity where the three methods performed poorly, although ADAM was better even in this case (no complete failures and lower *MARE* values).

The complete failures and the errors incurred by the three methods, and especially by the Geonaute SC, during the activity *Walk-turn-walk*, in all conditions of walking speed, can be partly explained as the consequence of the built-in assumption of registering a step only after that a certain number of consecutive steps have been observed. This assumption is common to all tested methods. In the absence of documented information about the behavior of the two commercial devices, we can only conjecture which value of the parameter  $St_{min}$  they have ( $St_{min} = 10$ , we believe). The approach we propose to dynamic thresholding allowed reducing  $St_{min}$  without substantial performance degradation, provided that the time delay  $K_d$  was suitably chosen.

From inspecting the performance data reported in Tables 4–6, the Samsung SC outperformed the Geonaute SC; ADAM outperformed both during *Walk-turn-walk* (in all variants) and *In-home task*. Moreover, the two wrist-worn SCs tended to perform better than the waist-worn SC when the walking speed was slower than normal, with the preference to be given to ADAM. We can conclude that the two commercial SCs were not probably designed to perform accurate step counting in those situations (slow and intermittent walking) where ADAM suited better. The data reported in Table 6 indicate *MARE* values incurred by ADAM lower than 5% during continuous walking across a range of speeds, which increased to 5%-18% when short walking bouts were considered. We consider the results of this paper in connection with the results reported by Cheng *et al.*, who analyzed step counts using a custom smartphone algorithm and a commercial waist-band SC when two healthy subjects walked 500 consecutive steps, [44]. The custom smartphone algorithm outperformed the waist-band SC, showing performance comparable to ours (activities *Slow and steady walk* and *Variable-speed walk*). However, they taped together the smartphone and the waist-band SC and fixed them at the L3 level (lower trunk). In these conditions, trunk accelerometry is widely regarded as a feasible technique to accurately measure spatio-temporal parameters of gait, including step time and cadence [45], [46]; however, serious concerns exist for its suitability when gait is pathologic, the gait speed is low, or both [47]. This same difficulty was recognized by Cheng *et al.*, in experiments involving COPD (Chronic Obstructive Pulmonary Disease) patients that performed the

Six Minutes Walking Test (6MWT), [44]; a discussion on the trend of state-of-the-art SCs to undercount steps in conditions of slow walking is also reported by Turner *et al.*, [48]. We verified the same behavior for either the Samsung or the Geonaute SC, which sometimes also completely failed to count at slow walking speeds. On the other hand, the undercount bias of ADAM was generally small. We consider therefore the ADAM error rate, particularly during the activity *Very slow walk*, a very promising result.

It is noted that ADAM and the Samsung SCs are two apps that run on the smartwatch, sharing the same raw accelerometer data. The ADAM step counting loop works at the rate of 25 samples per second; in the absence of any further information, we believe that the sampling rate is the same for the Samsung SC. In terms of power consumption, we verified that the time from full charge to complete discharge of the battery system is approximately 72 hours (low-power screen-off mode) and 5 hours (screen-on mode), irrespective of whether the Samsung SC runs alone or ADAM works in conjunction with it (the Samsung SC is a permanent application that cannot be aborted). The computational load of ADAM is therefore similar to that of the Samsung SC, and both apps drain only a limited amount of battery power, compared with the battery draining due to, e.g., the screen condition. Of course, any further consideration about the battery life must consider that smartwatches are devices that can be used for fulfilling many functions, including, e.g., telephony, e-mailing, Bluetooth connectivity, which all are known to be greedy of battery power. In this sense, the power requirements and the battery charging policies of a smartwatch would not be too dissimilar from those of a smartphone.

#### IV. CONCLUSIONS AND OUTLOOK

This paper was concerned with the development and the preliminary validation of a step counter that was designed for applications when ambulation can be slow and intermittent. The step counter was based on processing the accelerometer data measured by a commercial smartwatch using a custom wearable app (ADAM). Compared with either the native SC running in the smartwatch or a waist-worn SC, ADAM exhibited similar accuracy levels in conditions of normal walking, and was superior in conditions of slow and intermittent ambulation. The WPD algorithm developed in this paper for step counting can be ported to any wrist-worn mobile device that embeds a tri-axial accelerometer to measure wrist acceleration. Our novel approach to dynamic thresholding might be useful even in the implementation of WPDs for step counting using other accelerometer placement sites, although we have not tested it yet. As for the wrist, the experimental results shown in the paper offer promise for a robust solution to the problem of step counting in the difficult conditions of slow and intermittent walking.

The availability of a step counter that can detect slow and intermittent walking allows to overcome the limitations of currently available commercial devices. As a consequence, the proposed ADAM app has the potential to improve the

reliability of the objective quantification of mobility, physical activity level and fall risk in the elderly.

#### REFERENCES

- [1] K. L. Storti, K. K. Pettee, J. S. Brach, J. B. Talkowski, C. R. Richardson, and A. M. Kriska, "Gait speed and step-count monitor accuracy in community-dwelling older adults," *Med. Sci. Sports Exercise*, vol. 40, no. 1, pp. 59–64, 2008.
- [2] F. A. Storm, B. W. Heller, and C. Mazzà, "Step detection and activity recognition accuracy of seven physical activity monitors," *PLoS ONE*, vol. 10, no. 3, p. e0118723, 2015.
- [3] C.-C. Yang and Y.-L. Hsu, "A review of accelerometry-based wearable motion detectors for physical activity monitoring," *Sensors*, vol. 10, no. 8, pp. 7772–7788, 2010.
- [4] G. Fortino, R. Giannantonio, R. Gravina, P. Kuryloski, and R. Jafari, "Enabling effective programming and flexible management of efficient body sensor network applications," *IEEE Trans. Human-Mach. Syst.*, vol. 43, no. 1, pp. 115–133, Jan. 2013.
- [5] G. Fortino, R. Gravina, W. Li, and C. Ma, "Using cloud-assisted body area networks to track people physical activity in mobility," in *Proc. 10th EAI Int. Conf. Body Area Netw.*, 2015, pp. 85–91.
- [6] J. Howcroft, J. Kofman, and E. D. Lemaire, "Review of fall risk assessment in geriatric populations using inertial sensors," *J. NeuroEng. Rehabil.*, vol. 10, no. 1, p. 91, 2013.
- [7] M. Marschollek *et al.*, "Sensors vs. experts—A performance comparison of sensor-based fall risk assessment vs. conventional assessment in a sample of geriatric patients," *BMC Med. Inform. Decision Making*, vol. 11, p. 48, Dec. 2011.
- [8] V. T. van Hees *et al.*, "A novel, open access method to assess sleep duration using a wrist-worn accelerometer," *PLoS ONE*, vol. 10, no. 11, p. e0142533, 2015.
- [9] S. Chaudhuri, H. Thompson, and G. Demiris, "Fall detection devices and their use with older adults: A systematic review," *J. Geriatric Phys. Therapy*, vol. 37, no. 4, pp. 178–196, 2014.
- [10] P. A. Hageman and D. J. Blanke, "Comparison of gait of young women and elderly women," *Phys. Ther.*, vol. 66, no. 9, pp. 1382–1387, 1986.
- [11] J. J. Kavanagh and H. B. Menz, "Accelerometry: A technique for quantifying movement patterns during walking," *Gait Posture*, vol. 28, no. 1, pp. 1–15, Jul. 2008.
- [12] T. Asai, S. Misu, R. Sawa, T. Doi, and M. Yamada, "The association between fear of falling and smoothness of lower trunk oscillation in gait varies according to gait speed in community-dwelling older adults," *J. Neuroeng. Rehabil.*, vol. 14, p. 5, Jan. 2017.
- [13] C. Tudor-Locke, J. E. Williams, J. P. Reis, and D. Pluto, "Utility of pedometers for assessing physical activity: Convergent validity," *Sports Med.*, vol. 32, no. 12, pp. 795–808, 2002.
- [14] M. McCarthy and M. Grey, "Motion sensor use for physical activity data: Methodological considerations," *Nurs. Res.*, vol. 64, no. 4, pp. 320–327, 2015.
- [15] S. J. Duncan, G. Schofield, E. K. Duncan, and E. A. Hinckson, "Effects of age, walking speed, and body composition on pedometer accuracy in children," *Res. Quart. Exercise Sport*, vol. 78, pp. 420–428, Dec. 2007.
- [16] S. Horvath, D. G. Taylor, J. P. Marsh, and D. J. Kriellaars, "The effect of pedometer position and normal gait asymmetry on step count accuracy," *Appl. Physiol., Nutrition, Metabolism*, vol. 32, no. 3, pp. 409–415, 2007.
- [17] E. L. Melanson *et al.*, "Commercially available pedometers: Considerations for accurate step counting," *Preventive Med.*, vol. 39, no. 2, pp. 361–368, 2004.
- [18] C. J. Dondzila, A. M. Swartz, N. E. Miller, E. K. Lenz, and S. J. Strath, "Accuracy of uploadable pedometers in laboratory, overground, and free-living conditions in young and older adults," *Int. J. Behavioral Nutrition Phys. Activity*, vol. 9, p. 143, Dec. 2012.
- [19] A. Brajdic and R. Harle, "Walk detection and step counting on unconstrained smartphones," in *Proc. ACM Int. Joint Conf. Pervas. Ubiquitous Comput.*, 2013, pp. 225–234.
- [20] M. Susi, V. Renaudin, and G. Lachapelle, "Motion mode recognition and step detection algorithms for mobile phone users," *Sensors*, vol. 13, no. 2, pp. 1539–1562, 2013.
- [21] V. Renaudin, M. Susi, and G. Lachapelle, "Step length estimation using handheld inertial sensors," *Sensors*, vol. 12, no. 17, pp. 8507–8525, 2012.
- [22] M. A. Case, H. A. Burwick, K. G. Volpp, and M. S. Patel, "Accuracy of smartphone applications and wearable devices for tracking physical activity data," *J. Amer. Med. Assoc.*, vol. 313, no. 6, pp. 625–626, 2015.

- [23] A. Mannini, A. M. Sabatini, and S. S. Intille, "Accelerometry-based recognition of the placement sites of a wearable sensor," *Pervas. Mobile Comput.*, vol. 21, pp. 62–74, Aug. 2015.
- [24] S. Jayalath and N. Abhayasinghe, "A gyroscopic data based pedometer algorithm," in *Proc. 8th Int. Conf. Comput. Sci. Edu. (ICCSE)*, 2013, pp. 551–555.
- [25] *Category 2 Enhanced Phenotyping at Baseline Assessment Visit in Last 100-150,000 Participants*, UK Biobank, Coordinating Centre, Stockport, U.K., 2009.
- [26] R. Troiano and J. Mc Clain, "Objective measures of physical activity, sleep, and strength in U.S. National Health and nutrition examination survey (NHANES) 2011–2014," in *Proc. 8th Int. Conf. Diet Activity Methods*, Rome, Italy, 2012, p. 24.
- [27] A. Doherty et al., "Large scale population assessment of physical activity using wrist worn accelerometers: The UK Biobank study," *PLoS ONE*, vol. 12, no. 2, p. e0169649, 2017.
- [28] G. Appelboom et al., "Smart wearable body sensors for patient self-assessment and monitoring," *Arch. Public Health*, vol. 72, p. 28, Aug. 2014.
- [29] R. Rawassizadeh, B. A. Price, and M. Petre, "Wearables: Has the age of smartwatches finally arrived?" *Commun. ACM*, vol. 58, no. 1, pp. 45–47, 2014.
- [30] A. Mannini and A. M. Sabatini, "A smartphone-centered wearable sensor network for fall risk assessment in the elderly," in *Proc. 10th EAI Int. Conf. Body Area Netw.*, 2015, pp. 167–172.
- [31] M. S. Patel, D. A. Asch, and K. G. Volpp, "Wearable devices as facilitators, not drivers, of health behavior change," *J. Amer. Med. Assoc.*, vol. 313, no. 5, pp. 459–460, 2015.
- [32] A. Mannini, S. S. Intille, M. Rosenberger, A. M. Sabatini, and W. Haskell, "Activity recognition using a single accelerometer placed at the wrist or ankle," *Med. Sci. Sports Exercise*, vol. 45, no. 11, pp. 2193–2203, 2013.
- [33] Y. R. Modi, "Wrist pedometer step detection," U.S. Patent 0074431, Mar. 13, 2014.
- [34] R. Sourabh, "Adaptive step detection," U.S. Patent 0191069 A1, Jul. 25, 2013.
- [35] A. Mannini and A. M. Sabatini, "Walking speed estimation using foot-mounted inertial sensors: Comparing machine learning and strap-down integration methods," *Med. Eng. Phys.*, vol. 36, no. 10, pp. 1312–1321, 2014.
- [36] A. M. Sabatini, G. Ligorio, A. Mannini, V. Genovese, and L. Pinna, "Prior-to- and post-impact fall detection using inertial and barometric altimeter measurements," *IEEE Trans. Neural Syst. Rehabil. Eng.*, vol. 24, no. 7, pp. 774–783, Jul. 2016.
- [37] A. Mannini, M. Rosenberger, W. Haskell, A. M. Sabatini, and S. S. Intille, "Activity recognition in youth using single accelerometer placed at wrist or ankle," *Med. Sci. Sports Exercise*, vol. 49, no. 4, pp. 801–812, Apr. 2017.
- [38] A. Mannini et al., "Automatic classification of gait in children with early-onset ataxia or developmental coordination disorder and controls using inertial sensors," *Gait Posture*, vol. 52, pp. 287–292, Feb. 2017.
- [39] A. Mannini, D. Trojaniello, U. D. Croce, and A. M. Sabatini, "Hidden Markov model-based strategy for gait segmentation using inertial sensors: Application to elderly, hemiparetic patients and huntington's disease patients," presented at the 37th Annu. Int. Conf. IEEE Eng. Med. Biol. Soc., Milan, Italy, 2015.
- [40] E. Bergamini, G. Ligorio, A. Summa, G. Vannozzi, A. Cappozzo, and A. M. Sabatini, "Estimating orientation using magnetic and inertial sensors and different sensor fusion approaches: Accuracy assessment in manual and locomotion tasks," *Sensors*, vol. 14, no. 10, pp. 18625–18649, 2014.
- [41] N. Zhao, "Full-featured pedometer design realized with 3-axis digital accelerometer," *Analog Dialogue*, vol. 44, pp. 1–5, Jun. 2010.
- [42] R. Moe-Nilssen and J. L. Helbostad, "Estimation of gait cycle characteristics by trunk accelerometry," *J. Biomech.*, vol. 37, no. 1, pp. 121–126, 2004.
- [43] R. C. González, A. M. López, J. Rodriguez-Uría, D. Álvarez, and J. C. Alvarez, "Real-time gait event detection for normal subjects from lower trunk accelerations," *Gait Posture*, vol. 31, no. 3, pp. 322–325, Mar. 2010.
- [44] Q. Cheng, J. Juen, Y. Li, V. Prieto-Centurion, J. A. Krishnan, and B. R. Schatz, "GaitTrack: Health monitoring of body motion from spatio-temporal parameters of simple smart phones," in *Proc. Int. Conf. Bioinform., Comput. Biol. Biomed. Informat.*, 2013, p. 897.
- [45] W. Zijlstra and A. L. Hof, "Assessment of spatio-temporal gait parameters from trunk accelerations during human walking," *Gait Posture*, vol. 18, no. 2, pp. 1–10, Oct. 2003.
- [46] S. Nishiguchi et al., "Reliability and validity of gait analysis by Android-based smartphone," *Telemed. e-Health*, vol. 18, no. 4, pp. 292–296, 2012.
- [47] D. Trojaniello, A. Cereatti, and U. D. Croce, "Accuracy, sensitivity and robustness of five different methods for the estimation of gait temporal parameters using a single inertial sensor mounted on the lower trunk," *Gait Posture*, vol. 40, no. 4, pp. 487–492, Sep. 2014.
- [48] L. J. Turner, L. Houchen, J. Williams, and S. J. Singh, "Reliability of pedometers to measure step counts in patients with chronic respiratory disease," *J. Cardiopulmonary Rehabil. Prevention*, vol. 32, no. 5, pp. 284–291, 2012.

**VINCENZO GENOVESE** received the M.Sc. degree in electronic engineering from the University of Pisa and the Ph.D. degree in robotics from the Scuola Superiore Sant'Anna, Pisa, Italy. He is currently a Research Assistant with the BioRobotics Institute, Pisa.



**ANDREA MANNINI** was born in Empoli, Italy, in 1984. He received the M.Sc. degree in biomedical engineering from the University of Pisa, Pisa, Italy, in 2009 and the Ph.D. degree in innovative technologies from Scuola Superiore Sant'Anna, Pisa, in 2013. Since then, he has been a Research Assistant with the BioRobotics Institute, Pisa. In 2012, he joined as a Visiting Scholar the College of Computer and Information Science, Northeastern University, Boston, MA, USA. He has authored two book chapters and 16 international journal papers. His current research interests include machine learning algorithms applied to the human movement recognition and analysis.

Dr. Mannini was a recipient of the Italian Bioengineering Group Award for the best master thesis in 2009 and the best Ph.D. thesis in 2013 and the Italian Society for Movement Analysis best methodological paper and best young researcher paper in 2011.



**ANGELO M. SABATINI** (M'92–SM'06) received the M.Sc. degree in electronic engineering from the University of Pisa, Pisa, Italy, in 1986, and the Ph.D. degree in robotics from the Scuola Superiore Sant'Anna (SSSA), Pisa, in 1991. He was an Assistant Professor of biomedical robotics, SSSA, from 1992 to 2001. Since then, he has been an Associate Professor of biorobotics with SSSA, where he currently leads the Sensor Signals and Information Processing Area within the BioRobotics Institute. His research interests are in the field of wearable sensor systems, human motion analysis, and related computational methods.

Received 2 February 2024, accepted 18 February 2024, date of publication 21 February 2024, date of current version 29 February 2024.

Digital Object Identifier 10.1109/ACCESS.2024.3368394



## RESEARCH ARTICLE

# Design and Measurement of a Compact Millimeter Wave Highly Flexible MIMO Antenna Loaded With Metamaterial Reflective Surface for Wearable Applications

**B. G. PARVEEZ SHARIFF<sup>ID1</sup>, (Graduate Student Member, IEEE), TANWEER ALI<sup>ID1</sup>, (Senior Member, IEEE), PALLAVI R. MANE<sup>1</sup>, (Senior Member, IEEE), MOHAMMED GULAM NABI ALSATH<sup>ID2</sup>, (Senior Member, IEEE), PRADEEP KUMAR<sup>ID3</sup>, SAMEENA PATHAN<sup>ID4</sup>, AHMED A. KISHK<sup>ID5</sup>, (Life Fellow, IEEE), AND TAIMOOR KHAN<sup>ID6</sup>, (Senior Member, IEEE)**

<sup>1</sup>Department of Electronics and Communication Engineering, Manipal Institute of Technology, Manipal Academy of Higher Education, Manipal 576104, India

<sup>2</sup>Department of Electronics and Communication Engineering, College of Engineering Guindy, Anna University, Chennai 603110, India

<sup>3</sup>Discipline of Electrical, Electronic and Computer Engineering, Howard College Campus, University of KwaZulu-Natal, Durban 4041, South Africa

<sup>4</sup>Department of Information and Communication Technology, Manipal Institute of Technology, Manipal Academy of Higher Education, Manipal 576104, India

<sup>5</sup>Department of Electrical and Computer Engineering, Concordia University, Montreal, QC H3G 1M8, Canada

<sup>6</sup>Department of Electronics and Communication Engineering, National Institute of Technology Silchar, Silchar, Assam 788010, India

Corresponding author: Tanweer Ali (tanweer.ali@manipal.edu)

**ABSTRACT** This article presents a flexible four-element MIMO antenna designed on a thin polyimide substrate to operate at 30.50 GHz for wearable applications. The antenna element structure is a combination of circular rings combined with T-shape stubs. The MIMO antenna isolation is enhanced through a novel decoupling structure consisting of a rectangular stub, four open-ended horizontal strip lines, and two vertical strip lines connecting the ground plane. It provides 22.5 dB isolation, even with conformal orientation. A metamaterial (MTM) reflective surface of  $9 \times 9$  unit cells is designed and placed below the antenna to improve its radiation characteristics, bandwidth, gain, and specific absorption rate (SAR). The metamaterial unit cell provides a double negative property with a wide stop-band range of 26.27–36.49 GHz. With an MTM surface, the measured bandwidth is 25.2–33 GHz with a maximum broadside gain of 8.90 dBi. The resulting SAR is reduced from 1.71 W/kg to 0.86 W/kg by incorporating MTM reflective surface. The MIMO antenna with MTM improves the bandwidth by 56%, gain by 32.5%, and radiation from bidirectional to broadside, compared to the MIMO antenna without MTM. Also, the antenna is measured and validated for diversity parameters such as Envelope correlation coefficient (ECC), Diversity gain (DG), Channel coefficient loss (CCL), Total active reflection coefficient (TARC), and Mean effective gain (MEG). The reduced SAR and improved antenna performance suggest the proposed MIMO antenna with an MTM reflective surface is suitable for on-body wearable applications in IoT devices, smart watches, headwear, and footwear devices.

**INDEX TERMS** Decoupling structure, flexible substrate, metamaterial, MIMO, millimeter wave, SAR measurement, wearable antenna, on-body measurement.

## I. INTRODUCTION

With the increased number of wearable users globally, the market valuation stands at 61.30 billion USD as of 2022. Demand is estimated to rise exponentially, with a compound

The associate editor coordinating the review of this manuscript and approving it for publication was Luyu Zhao<sup>ID</sup>.

annual growth rate (CAGR) of 14.6% from 2023 to 2030 [1]. In wearable devices, wristwear dominates the global market, and other products such as eyewear, headwear, and footwear are also slowly trending. The wristwear devices focus on health monitoring for sports or patients by observing the change in body metabolism, which is measured through sensors. Seamless connectivity with a high data rate is essential for these devices to log data continuously with the other connected devices/systems. For this purpose, various wearable antennas are designed and developed to operate at sub-6 GHz [2], [3]. However, bandwidth at sub-6 GHz is restricted to <100 MHz [4]. The International Telecommunication Union (ITU) allocated a millimeter wave (mmWave) spectrum 30-300 GHz range to enhance the channel capacity, in that K-band (18-27 GHz) and Ka-band (26.5-40 GHz) are least prone to atmospheric conditions [5]. For wearable devices, the flexible antenna should satisfy the following criteria against conformal orientation: minimum operational bandwidth of 1 GHz, a specific absorption rate (SAR) < 1.6 W/kg (Federal Communication Commission (FCC) standard)/ < 2 W/kg (European Union (EU) standard), and stable bandwidth and radiation. For flexible antenna design, highly conformal substrates such as polyethylene terephthalate (PET) [6], flexible printed circuit board (FPCB) [7], liquid crystal polymer [8], and polytetrafluoroethylene (PTFE) are used with thickness ranging from 0.2 to 0.1 mm.

In order to cater higher data rate for wearable technology at mmWave, the MIMO antenna is a preferred choice [9]. However, the design of a flexible MIMO antenna has several challenges against conformal orientation, such as: maintaining good isolation, stable bandwidth, and directional radiation. There are various techniques by which good isolation can be obtained, such as decoupling structures [10], [11], artificial magnetic conductors [12], metamaterial structures [13], self-isolating radiators [14], parasitic elements [15], and hybrid structures (combination of above methods) [16]. Any modification to the antennas ground plane to improve the isolation adversely affects the radiation pattern, generating bidirectional or omnidirectional radiation. In such cases, the human body is exposed to electromagnetic radiation from the antenna, resulting in a higher SAR value. Therefore, the directivity and SAR of a MIMO antenna at mmWave can be improved by incorporating a metasurface/ metamaterial reflectors [17], a split ring resonator (SRR) [18], and a metasurface lens [19], [20] (for directivity).

In [21], a two-element MIMO antenna is proposed for wearable applications where the radiator is a slotted circular patch with defected ground plane structure operating from 24-31 GHz. The slots in the radiator induced the effect of circular polarization. However, in the above design, the substrate used is semi-flexible, and the radiation pattern is omnidirectional. In another two-element flexible MIMO antenna [22], an electromagnetic bandgap (EBG) layer is placed below the antenna to improve the directivity and reduce the SAR. Though the EBG has slightly enhanced the gain from 4.5 to

5.7 dBi, the bandwidth remains narrow. In [13], an 8-element modified antipodal Vivaldi antenna incorporated the SRR and mender line to improve the isolation to 22 dB. However, the design has the limitation of a large antenna profile and SAR of 2.25 per 1g at 28/38 GHz. Another design proposed an eight-element MIMO antenna operating from 4.8-30 GHz for breast cancer detection [23]. However, the above design has limitations of complex design and poor isolation.

The above literature shows that quite a few MIMO antenna designs exist for wearable applications. The MIMO antennas in [13], [21], [22], and [23] have a large antenna profile. In [24] and [25], the design has poor impedance matching with high SAR. The structures in [26] and [27] have low gain. The [22] and [28] have low bandwidth, and the [23] have poor isolation.

Therefore, the above limitations are addressed in this paper by developing a novel, compact, flexible MIMO antenna structure. In addition, a novel decoupling structure is proposed in the ground plane, consisting of a rectangular stub, four open-ended strip lines, and two strip lines connecting the ground planes, achieving isolation greater than 22.5 dB.

The MIMO antenna performance is further improved by incorporating a  $9 \times 9$  flexible metamaterial (MTM) reflective surface. Though an MTM reflective surface increases the antenna profile, it offers plenty of advantages, such as enhanced bandwidth, gain, and radiation pattern. Also, it aids in suppressing the radio frequency (RF) energy exposure to the human body with reduced SAR. The overall MIMO antenna profile with MTM reflective surface is  $22 \times 22 \times 3.45$  mm<sup>3</sup>. In terms of wavelength at 30.5 GHz, it is  $2.25\lambda_0 \times 2.25\lambda_0 \times 0.35\lambda_0$  indicating that the height of the antenna profile is just 15.5% compared to its length and width. Relatively, the overall antenna profile is comparable with the other existing designs.

For flexible antennas, the choice of substrate greatly defines its performance. Because the flexible/wearable antenna undergoes conformal orientation, the chosen substrate should have good electrical and mechanical properties. There are various flexible substrates used in the literature to design antenna, such as felt-textile [2], liquid crystal polymer (LCP) [8], silicone rubber [27], polyester [29], jeans [30], etc. The detailed analysis of flexible substrates is presented in [31]. Out of these, the polyimide substrate has gained attention in the early 90s to design microcircuits for biomedical applications [32]. Later, polyimides are used in the design of flexible antennas due to their high flexibility, robustness, good electrical and mechanical properties, and high-temperature stability [33]. Therefore, based on the literature, the antenna design in this article uses a polyimide substrate for MIMO design and a metamaterial reflective surface.

The 3D representation of a four-element MIMO antenna and metamaterial reflective surface separated by a distance  $d_{gap}$  is shown in Fig. 1(a). Fig. 1(b) shows a photograph of the fabricated prototype antenna. The MIMO antenna with

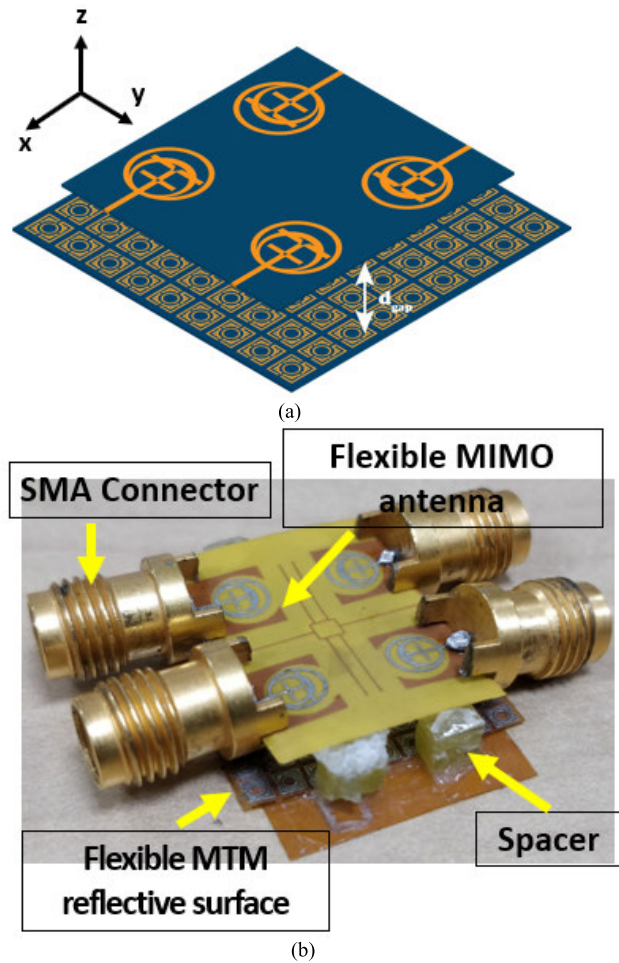


**FIGURE 1.** (a) 3D sketch of the four-element MIMO antenna above a metamaterial reflective surface and (b) An image of the fabricated antenna with MTM reflective surface below.

an MTM reflective surface achieved 25.2–33 GHz bandwidth, 8.9 dBi gain, directional radiation, and 0.86 W/kg of SAR.

The main contribution of the article is as follows:

1. For a four-element MIMO antenna, the coupling effect is studied through the model current vector diagram, which is minimized by a proposed decoupling structure.
2. A  $9 \times 9$  metamaterial reflective surface is proposed to improve the antenna performance in terms of bandwidth, gain, radiation pattern, and SAR.
3. Performed on-body measurement to verify the real-time variation in the reflection coefficient and further mimicked the phantom model to measure the radiation pattern.

## II. DESIGN OF SINGLE-ELEMENT ANTENNA

The design uses a polyimide substrate with a thickness of 0.1 mm, permittivity of 3.5, and a loss tangent of 0.008, which is highly flexible and robust [33]. The antenna is designed to resonate at  $f_0 = 30.50$  GHz. The single-element

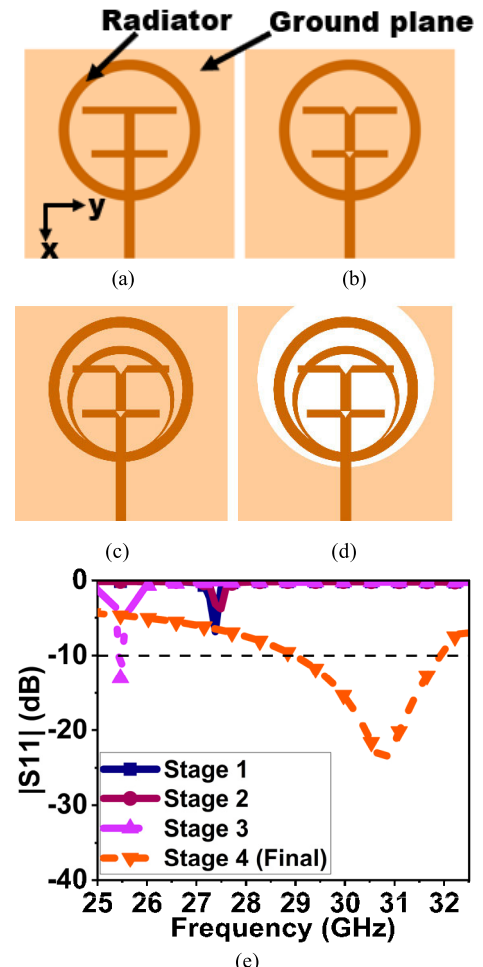


**FIGURE 2.** Evolution stages of the single-element antenna and its S-parameter. (a) Stage 1, (b) Stage 2, (c) Stage 3, (d) Stage 4 (Final), and (e) Reflection coefficient of single-element at respective stages.

evolved through four stages. Stage 1 combines a concentric ring with two T-shape structures and has a complete ground plane (Fig. 2(a)); Stage 2 introduces slit/slots onto the radiator (Fig. 2(b)); Stage 3 adds an inverted crescent to a radiator (Fig. 2(c)), and in Stage 4 a circular slit is etched in the ground plane (Fig. 2(d)).

The detailed analysis of this single-element antenna is presented in [34] using characteristic mode analysis to better understand the structural and radiation behavior. However, this section briefly explains the theoretical analysis of single-element antenna.

At stage 1 and stage 2 (Figs. 2(a & b)), the impedance matching is poor with low bandwidth, as shown in Fig. 2(e). Adding an inverted crescent in stage 3 (Fig. 2(c)) increases the conductive area, resulting in a downshift of resonance at 25.5 GHz with better impedance matching and reflection coefficient  $|S_{11}|$  of 14 dB. To improve the bandwidth and upshift the resonance frequency, a portion of the conductive area is etched from the ground plane in the final stage (stage 4) (Fig. 2(d)) [35], [36]. Therefore, in the final

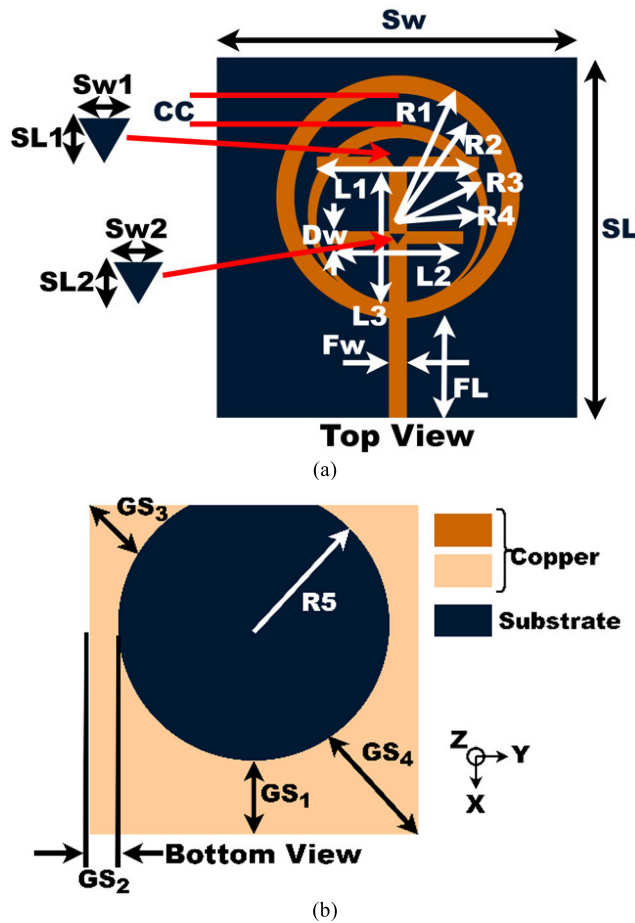


**FIGURE 3.** Final flexible single-element antenna with dimensions. (a) Top view, (b) bottom view [34].

stage, the obtained reflection coefficient at  $|S_{11}| > 10$  dB is 28.80–31.90 GHz, with resonance at 30.70 GHz, as shown in Fig. 2(e). The dimensions of final single-element antenna as follows:  $R1 = 1.95$ ,  $R2 = 1.7$ ,  $R3 = 1.45$ ,  $R4 = 1.25$ ,  $R5 = 2.4$ ,  $L1 = 3$ ,  $L2 = 2$ ,  $L3 = 2.09$ ,  $SL2 = Dw = 0.2$ ,  $Fw = 0.25$ ,  $FL = 1.8$ ,  $CC = 0.62$ ,  $GS1 = 1.6$ ,  $GS2 = 0.6$ ,  $GS3 = 1.24$ ,  $GS4 = 2.62$ ,  $SL1 = SW2 = 0.3$ ,  $Sw1 = 0.26$ , and  $Sw = SL = 6$  (all dimensions in mm, R4 circumference is aft by 0.18 mm than of R3 in x-axis), as shown in Figs. 3(a & b).

The design equation to calculate the antenna resonance is a modified equation of [37] and [38]:

$$f_0 = \frac{c}{k \times \frac{2}{\pi} \times T_A \times \sqrt{\epsilon_r}} \quad (1)$$

where  $k$  is a tolerance value calculated using (2),  $c$  is the speed of light in free space ( $3 \times 10^{11}$ ) in mm, and  $T_A$  is the total conducting area, which is the summation of the total area of the radiator ( $T_{AR}$ ) and ground plane ( $T_{AG}$ ) (3).

$$k = \sqrt{\frac{14 \times T_A}{\pi \times T_A^2}} \quad (2)$$

$$T_A = T_{AR} + T_{AG} \quad (3)$$

$$T_{AR} = (\pi R1^2 - \pi R2^2) + (\pi R3^2 - \pi R4^2) + (FL \times Fw) + (L1 \times Dw) + (L2 \times Dw) + (L3 \times Dw) \quad (4)$$

$$T_{AG} = (SL \times Sw) - (\pi R5^2 - A_{SEG}) \quad (5)$$

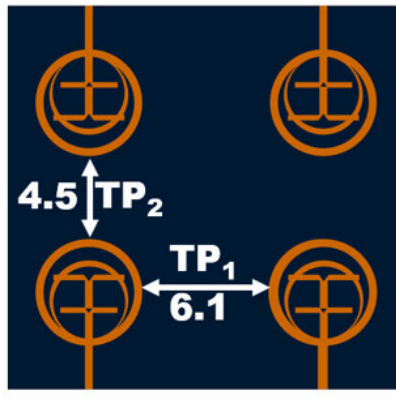
$$A_{SEG} = \left( \frac{\theta}{360^\circ} \right) \times \pi R5^2 - \frac{1}{2} \times R5^2 \sin \theta \quad (6)$$

The conductive area of the ground plane is etched with a circular slot, where the minor segment of the circle is excluded. Therefore, in calculating the area of the ground plane minor segment of the circle is to be added. From the above-given dimensions in Fig. 3, the  $\theta$  result in  $66^\circ$ , from which the  $A_{SEG} = 0.71$  (Note: all dimensions are in mm) from (6). Further, the total area of the ground plane  $T_{AG} = 18.62$  from (5), and the total area of the radiator  $T_{AR} = 6.43$  from (4). Adding both the conducting area  $T_A$  results in 25.05. Here,  $k$  is the tolerance value, which results in 0.42 from equation (2). Substituting all these values to calculate the theoretical value of resonance  $f_0$  in (1) results in 30.06 GHz, which is close to the desired resonance frequency.

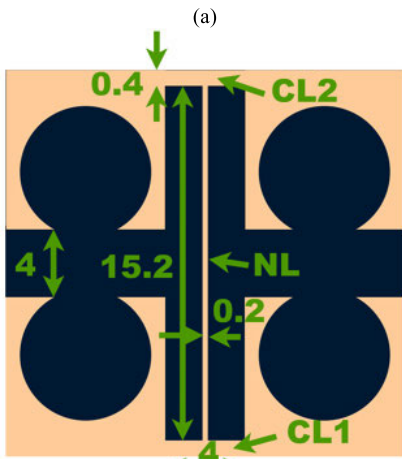
### III. FOUR-ELEMENT MIMO ANTENNA

The above single-element is extended to a four-element MIMO antenna, as shown in Fig. 4(a). The two elements are adjacent at a distance  $TP_1 = 0.62\lambda_0$ , and the other two elements are mirrored vertically at a distance  $TP_2 = 0.41\lambda_0$ . The overall antenna profile is  $1.63\lambda_0 \times 1.63\lambda_0$ . The initial structure of the ground plane in Fig. 4(b) has a microstrip line  $NL$  connected to the ground for all ports. The  $NL$ ,  $CL1$ , and  $CL2$  form the initial decoupling structure (DCS). This structure provides good isolation between adjacent elements. In this case, the DCS has dual functionality: (i) giving all elements a common ground plane and (ii) behaving as a neutralization structure generating reverse current along the line, reducing the mutual coupling. The neutralization structure can be an arbitrary shape incorporated into the ground or radiator plane [39], [40].

To comprehend the DCS functionality of Fig. 4(b), let us consider the current vector diagram of Fig. 5(a) derived from the surface current vector of Fig. 5(b) when Port-1 (P1) is excited. The general analysis of DCS is as follows: the coupling current  $J_n^+$  indicates the current flowing from  $(n_{th})$  port to  $(n_{th} + m)$  port,  $J_m^+$  is the reverse current flowing from  $(m_{th})$  port, and  $J_m^-$  is the minor coupling current towards  $(m_{th})$  port (which is part of  $J_n^+$ ), when the port  $n$  is excited. In this case, the current  $J_2^-$  is the minor coupling current to Port-2 (P2) and  $J_2^+$  is reverse current from Port-2 (P2), generated from  $J_1^+$  on  $CL1$  line when P1 is excited. The magnitude of  $J_2^-$  and  $J_2^+$  are equal with out-of-phase, resulting in a cancellation, obtaining isolation  $|S_{21}|$  of 33 dB throughout the band, as displayed in Fig. 6. The current  $J_1^+$  is confronted with  $(J_3^+ + J_4^+)$ , which is out-of-phase on the  $NL$  line, canceling most of the current but generating two coupling currents on  $CL2$  as  $J_3^-$  and  $J_4^-$ . The current density  $J_4^-$  is low, so isolation between ports 1 and 4 is moderate at 30 dB. But  $J_3^-$  is high, affecting port 3. Therefore,



Top View



(b)

**FIGURE 4.** Proposed four-element MIMO antenna with initial decoupling structure (DCS). (a) Top view, (b) bottom view.

the isolation  $|S_{31}|$  obtained is 20 dB in Fig. 6. A similar analogy can be applied when Ports 2, 3, and 4 are excited individually. The initial DCS has provided good isolation on adjacent and diagonal ports but poor isolation on opposite ports.

Further, to improve the isolation between opposite elements, the DCS structure in the ground plane is modified, as illustrated in Fig. 7. It has a rectangular ring (*NRL*), open-ended strip lines *NL3* to *NL6*, and a ground plane connecting strips *NL1* and *NL2*. The *NL3* and *NL4* traps most of the coupling current between port-1 and port-3. Similarly, *NL5* and *NL6* trap the surface wave current between Ports 2 and 4. The modified DCS provides good isolation between adjacent and opposite elements.

Figs. 8(a & b) is the current model diagram derived from the current vector diagram when P1 is excited for the MIMO antenna with the proposed DCS. In this case, the proposed DCS perturbs the current flow in the structure. As a result, the current  $J_1^+$  in Fig. 8(a) and its coupling current  $J_2^-$ , density is higher compared to the reverse current  $J_2^+$  on

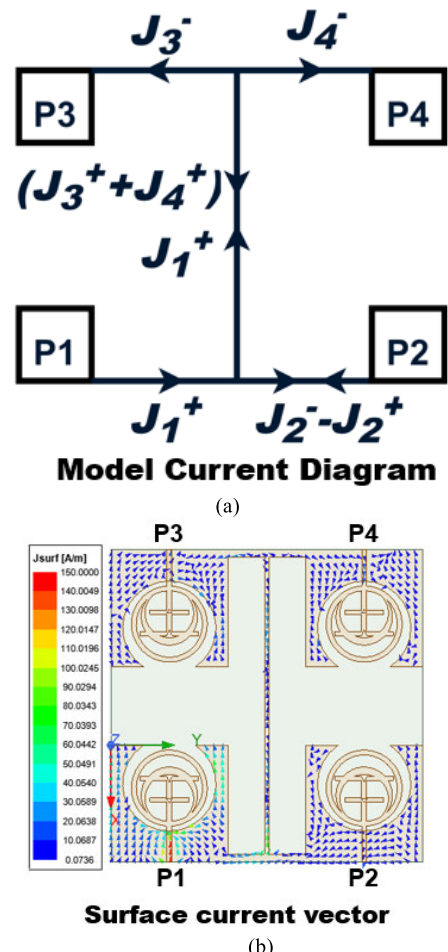


**FIGURE 5.** Current vector representation of initial DCS structure. (a) Derived model current diagram. (b) Surface current vector.

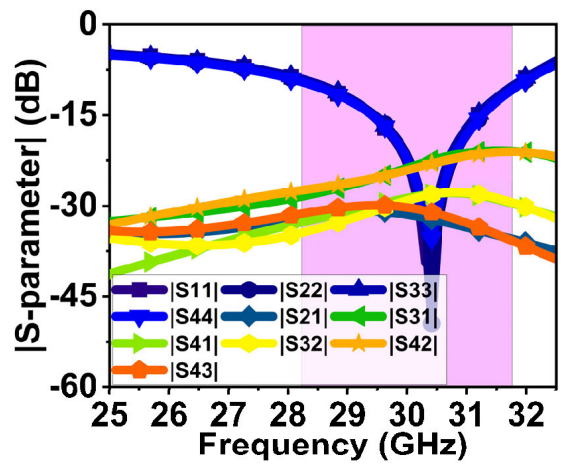


**FIGURE 6.** |S-parameter| of four-element MIMO antenna for initial DCS.

*CL1*, so a small coupling can be seen at port 2, resulting in an isolation  $|S_{21}|$  of 25 dB, as displayed in Fig. 9. On *NL1*, *NL2*, *NL3*, and *NL4*  $J_1^+$  is confronted with reverse current  $J_2^+$ ,  $J_3^+$ , and  $J_4^+$  which regulates the coupling between

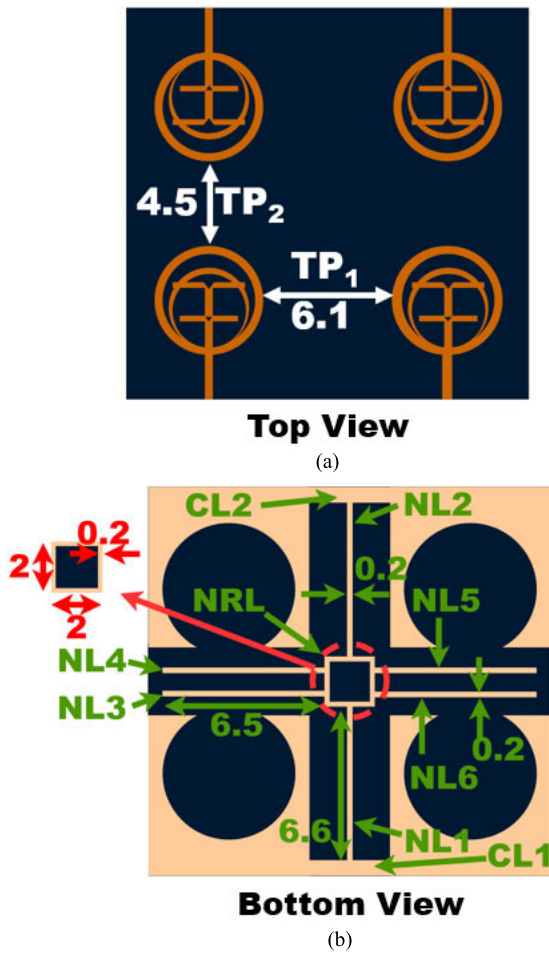


**FIGURE 7.** Proposed four-element MIMO antenna with final DCS. (a) Top view, (b) bottom view. (Note: all dimensions are in mm).

$|S_{31}|$  and  $|S_{41}|$ , resulting in isolation of 27 and 34 dB. The proposed DCS structure has slightly drifted the resonance to 30.10 GHz. However, it retained the desired bandwidth of 28.27-31.64 GHz, as shown in Fig. 9.

#### A. EQUIVALENT CIRCUIT OF DECOUPLING STRUCTURE

This section represents the behavior of the proposed DCS structure (i.e., Fig. 7(b)) in terms of distributed lumped  $LC$  equivalent circuits. The theoretical approach for equivalent circuits follows the transmission theory with impedance characteristics, as discussed in [41]. For the purpose of analysis, the DGS structure is considered lossless, so the resistance effect is considered negligible. The initial  $LC$  values are obtained using the equations presented in [41], which are further tuned to obtain a response close to the simulated results. The circuit is realized using AWR design software. The  $CL1$  &  $CL2$  in Fig. 7(b) is a microstrip line between Port-1 & 2 and between Port-3 & 4, represented by inductive components ( $L1$ ,  $L2$ ) and ( $L10$ ,  $L11$ ). The  $NL1$  &  $NL2$  are rectangular strip lines of DCS represented by inductance  $L3$  and  $L9$ . The narrow gap between these lines and port grounds

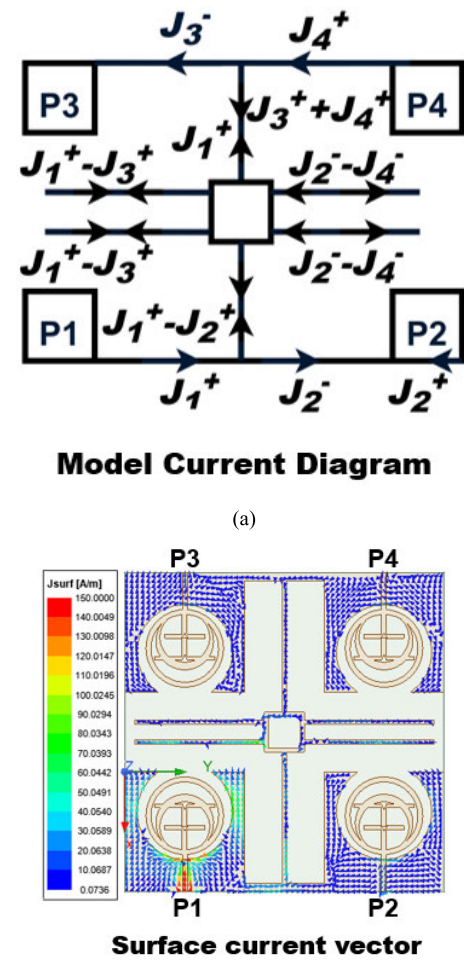


**FIGURE 8.** Current vector representation of proposed DCS structure. (a) Derived model current diagram. (b) Surface current vector.

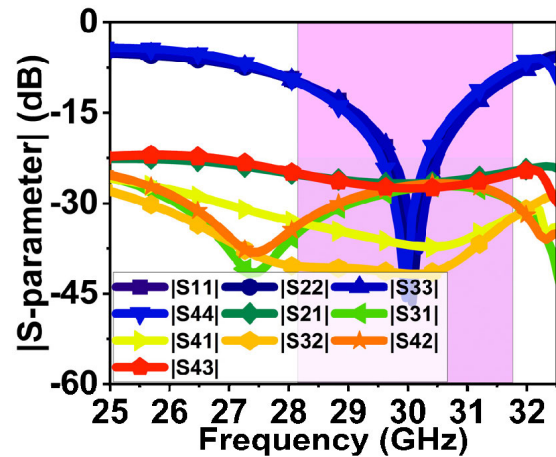


**FIGURE 9.**  $|S\text{-parameter}|$  of four-element MIMO antenna for final DCS.

has the capacitance effect, represented as  $C1$ ,  $C2$ ,  $C5$ , and  $C6$  in Fig. 10(a).

The rectangular ring  $NRL$  constitutes inductance ( $L12$  and  $L4$ ) and the gap by capacitance  $C7$ . The open-circuited strip line  $NL3$  to  $NL6$  is represented by inductance  $L5$  to  $L8$  and the gap by capacitance  $C3$  and  $C4$ . These inductance

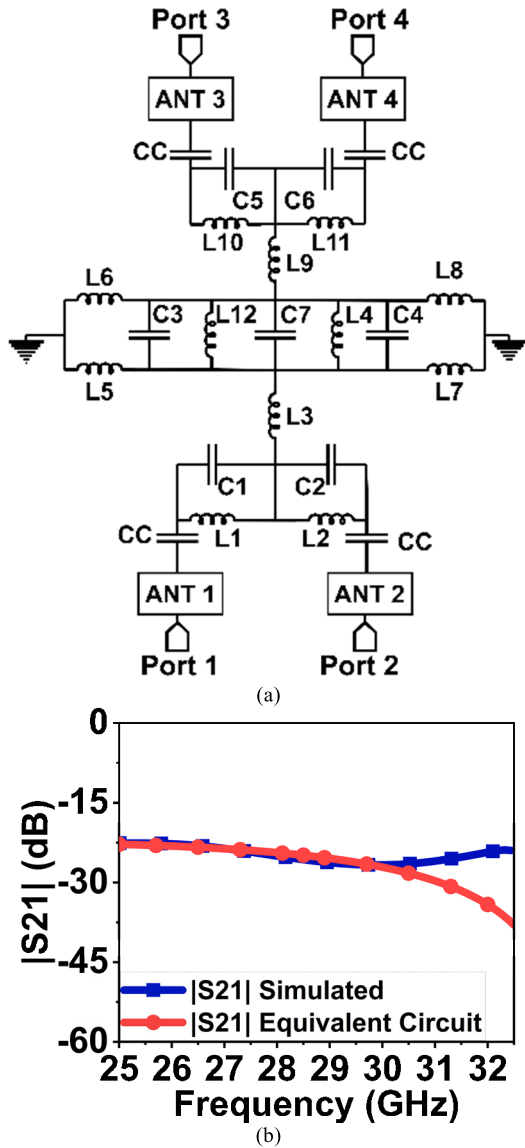


**FIGURE 10.** (a) Lumped equivalent circuit of proposed decoupling structure (DCS). (b) S-parameter comparison graph of simulated with an equivalent circuit.

and capacitance form the parallel resonance circuit, and the desired response can be obtained by tuning. For this case, the analysis is performed for isolation  $|S_{21}|$ . Therefore, the  $LC$  components primarily contributing to  $|S_{21}|$  are  $L_1$ ,  $L_2$ ,  $L_3$ ,  $C_1$ , and  $C_2$ , with values of  $0.074\text{ nH}$ ,  $0.20\text{ nH}$ ,  $0.018\text{ nH}$ ,  $0.30\text{ pF}$ , and  $0.06\text{ pF}$ . Whereas all other  $LC$  values are set to  $0.001\text{ nH}$  and  $0.001\text{ pF}$ . Likewise, to obtain the response for  $|S_{31}|$ ,  $L_1$ ,  $L_3$ ,  $L_{12}$ ,  $L_5$ ,  $L_6$ ,  $L_9$ ,  $L_{10}$ ,  $C_1$ ,  $C_3$ ,  $C_7$  and  $C_5$  need to be tuned. Therefore, the proposed  $LC$  circuit generates the closest response to the proposed four-port MIMO antenna isolation  $|S_{21}|$ , as shown in Fig. 10(b).

#### B. BENDING ANALYSIS OF THE PROPOSED MIMO ANTENNA

The polyimide substrate is more elastic than other substrates [42], which is why it is used in various RF antenna

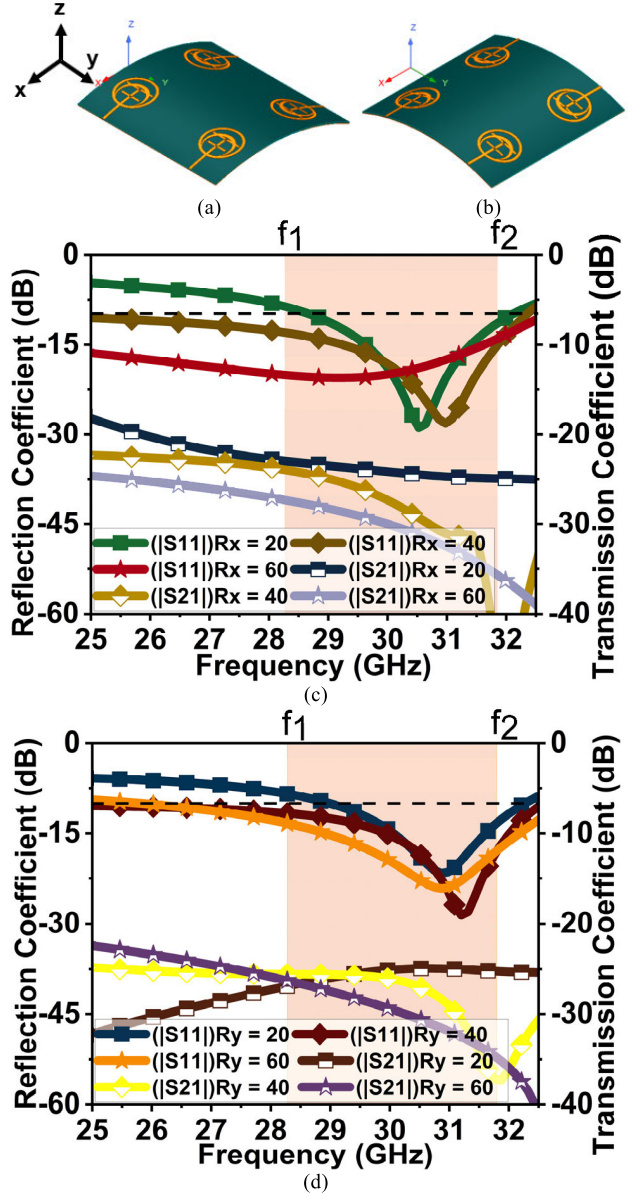


**FIGURE 11.** (a) Bending along the x-axis and its respective  $|S$ -parameter| in (c). (b) Bending along the y-axis and its respective  $|S$ -parameter| in (d).

applications [43]. As the proposed four-element MIMO antenna is for wearable applications, the performance of the antenna should not be affected much when it undergoes conformal orientation. Generally, wearable devices are worn on the wrist, forearm, neck, chest, and legs. Out of these, the wrist has the smallest circumference of 155 to 190 mm (for adults). For this reason, the bending analysis is performed along the x- and y-axis (Figs. 11(a &b)) with a radius of 20 to 60 mm in steps of 5 mm.

For the 20 to 50 mm radius along the x-axis, a slight change in resonance can be seen between 30.50 and 31 GHz. For 20 and 25 mm radii, the lower cut-off frequency ( $f_1$ ) is shifted from 28.30 to 28.72 GHz. The higher cut-off frequency ( $f_2$ ) is shifted for all the radii to more or less at 32 GHz. The

bandwidth at  $|S_{11}| < -10$  is 28.70-31.9 GHz and 28.72-32.1 GHz, respectively, with maximum isolation of 24.9 dB and 26.89 dB. However, for the 30 to 60 mm radius, the bandwidth at reflection coefficient  $|S_{11}| < -10$  dB has increased, which is 25-32 GHz, as shown in Fig. 11(c) (*due to brevity in the image, only a few plots are presented in Figs. 11(c & d)*). The isolation for all the radii is well above 20 dB. The result shows that the isolation is improved from 25 to 30 dB for higher radii (40 to 60 mm), which are linearly increasing with frequency.

For the y-axis bend (Fig. 11(b)), the  $f_2$  is increased to 32 GHz for all the radii. Meanwhile, for 20 mm and 25 mm radii, the  $f_1$  is shifted higher, resulting in a reduction in bandwidth of 28.80-32 GHz. For 30 to 60 mm radii, the  $f_1$  is shifted lower, increasing bandwidth from 26.50-32 GHz. The isolation at all the radii is well above 20 dB, as seen in Fig. 11(d). The results reveal that the structure design is versatile enough to give stable results for conformal orientation. The structure reasonably maintains the bandwidth compared to its non-conformal results.

#### **IV. METAMATERIAL REFLECTIVE SURFACE**

The metamaterial structures are well known for their equivalent negative permittivity, permeability, and/or refractive index properties. It has been implemented in some antennas as reflective surfaces, metasurface lenses, frequency-selective surfaces, and so on [44], [45]. The proposed four-element MIMO antenna has bidirectional radiation due to defected ground structure. A metamaterial reflective structure is designed to act as a bandstop filter at the resonance  $f_0$  [22], [28]. It is to reduce the back radiation, which in turn regulates the specific absorption rate (SAR).

## A. UNIT CELL STRUCTURE

The proposed unit cell has a feature of wide stop-band characteristics with double negative and refractive index properties. It combines rectangular and circular rings on a flexible polyimide substrate of 0.1 mm thickness. The unit cell size is in the range of  $\frac{\lambda_0}{10} < d < \frac{\lambda_0}{2}$  simulated by HFSS with primary and secondary boundary conditions. Two Fouquet port excitations are provided on the top and bottom of the boundary. The conductive surface on a substrate is assigned a perfect electric conductor (PEC), which acts as an inductor, and the gap between them gives the capacitance effect. Therefore, the unit cell resonance can be calculated using (7), where  $L_t$  and  $C_t$  are the total inductance and capacitance of the unit cell.

$$f_0 = \frac{1}{2\pi\sqrt{L_t C_t}} \quad (7)$$

The proposed unit cell with dimensions is shown in Fig. 12(a), and the generalized equivalent circuit in terms of a transmission line (TL) is shown in Fig. 12(b). Here, the substrate (DE) thickness acts as a TL, and the conducting surface of the substrate has  $L_t$  and  $C_t$  properties, which act as a series of RLC-equivalent circuit between TL. Since there is no conducting surface at the bottom of the substrate, the output

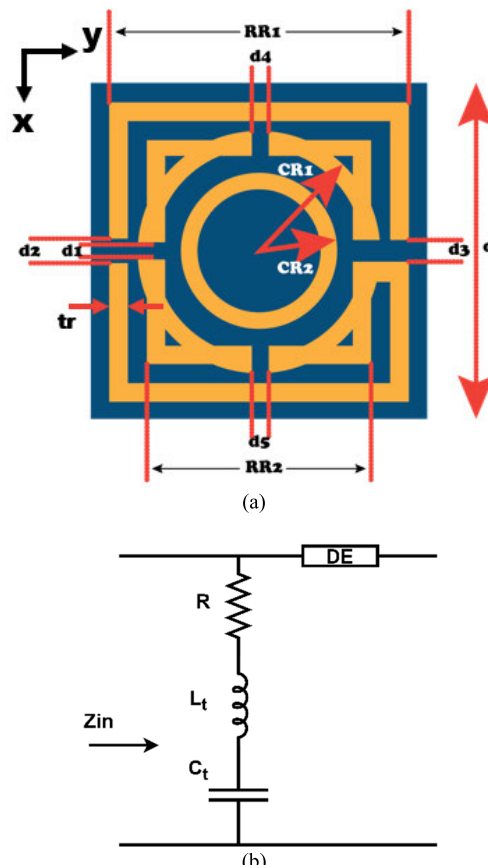


**FIGURE 12.** (a) Proposed unit cell structure with its dimension. RR1 = 1.8 mm, RR2 = 1.4 mm, CR1 = 0.75 mm, CR2 = 0.5 mm, d1 = d4 = d5 = 0.05 mm, d2 = d3 = 0.1 mm. (b) Generalized representation of unit cell in terms of transmission line.

impedance of the transmission line is open-circuited. The incident wave on the unit cell passes through it until  $L_t$  and  $C_t$  values are unequal. When these values become equal, the series RLC circuit acts as a short-circuit at the input of the transmission line and reflects the waves. Thus, the unit cell acts as a reflector.

To realize the equivalent permittivity ( $\epsilon_{eq}$ ), permeability ( $\mu_{eq}$ ), and refractive index (n) of the proposed unit cell, the simulated S-parameter from the HFSS is fed to an analytic or numeric model that uses the same volumetric parameters as the original cell (Thickness and reference plane position from the ports that provide the S-parameters for this model with its  $\epsilon_{eq}$  and  $\mu_{eq}$  varying the model provides similar S-parameters to that from HFSS). This is performed using the MATLAB tool. The unit cell impedance (z) and refractive index (n) are derived from the S-parameter using equations (8)-(10) [46].

$$z = \pm \sqrt{\frac{(1 + S_{11})^2 - S_{21}^2}{(1 - S_{11})^2 - S_{21}^2}} \quad (8)$$

$$e^{jnk_0d} = \frac{S_{21}}{1 - S_{11}\frac{z-1}{z+1}} \quad (9)$$

$$n = \frac{1}{k_0 d} \left[ \left\{ Im \left[ \ln \left( e^{j n k_0 d} \right) \right] + 2m\pi \right\} - j Re \left[ \ln \left( e^{j n k_0 d} \right) \right] \right] \quad (10)$$

where  $k_0$  is the wavenumber and  $d$  is the maximum length of the unit element. The permittivity ( $\epsilon_{eq}$ ) and permeability ( $\mu_{eq}$ ) derived from refractive index and impedance as:

$$\epsilon_{eq} = \frac{n}{z} \quad (11)$$

$$\mu_{eq} = nz \quad (12)$$

The unit cell evolved through three stages, as displayed in Figs. 13(a to c). In Stage 1, a rectangular ring  $RR2$  of  $1.4 \text{ mm}^2$  (thickness  $tr = 0.1 \text{ mm}$ ) is etched inside another ring  $RR1$  of  $1.8 \text{ mm}^2$  (thickness  $tr = 0.1 \text{ mm}$ ) with a separation of  $0.1 \text{ mm}^2$ . A circular ring  $CR1$  of  $0.12 \text{ mm}$  thickness (outer radius  $0.75 \text{ mm}$  and inner radius  $0.63 \text{ mm}$ ) is overlayed on  $RR2$ . The structure exhibits the stop band behavior at  $25.68 \text{ GHz}$  for the first stage. The surface current in Fig. 13(d) indicates that the electric field current is concentrated mostly in the outer ring and flows horizontally along the  $y$ -axis.

Further, in Stage 2 (Fig. 13(b)) structure is added with another circular ring  $CR2$  with  $0.1 \text{ mm}$  thickness (outer radius  $0.5 \text{ mm}$  and inner radius  $0.4 \text{ mm}$ ) at the center and slits  $d1$ ,  $d2$ , and  $d3$  at multiple points. Due to these slits, the current started flowing clockwise, mainly in the outer and inner circles (Fig. 13(e)). It resulted in a stopband at  $30.35 \text{ GHz}$  and a passband at  $31.68 \text{ GHz}$ . However, the obtained response has narrow stop-band attenuation.

Therefore, in Stage 3 (Fig. 13(c)), two vertical slits,  $d4$  and  $d5$  are etched, resulting in a wide stop-band from  $26.27$ - $36.49 \text{ GHz}$ . The surface current in Fig. 13(f) indicates the current concentration in the outer ring. The slit widths of  $d1$ ,  $d2$ ,  $d3$ ,  $d4$ , and  $d5$  are fine-tuned ( $0.05$ ,  $0.1$ ,  $0.1$ ,  $0.05$ , and  $0.05 \text{ mm}$ ) to obtain the resonance at  $f_0$ , as shown in Fig. 13(g). The designed unit cell has the material property of double negative, that is, negative permittivity ( $\epsilon$ ), permeability ( $\mu$ ), and refractive index in Fig. 13(h).

Due to the complexity of the unit cell, its detailed transmission line representation becomes more complicated. Therefore, an equivalent  $RLC$  circuit is designed in Fig. 14(a) to analyze its behavior ( $R$  is minimal; hence, it is neglected). However, the initial  $LC$  values are calculated using equations defined in [41]. The conducting surface has inductance represented by  $UL$  (unit cell inductor), and the gap between them is represented by  $UC$  (unit cell capacitors).  $UL11$ ,  $UL10$ ,  $UL12$ , and  $UL13$  represent the inductance of the outer ring ( $RR1$ ) and the gap  $d2$  and  $d3$  by  $UC17$  and  $UC18$  capacitance. The gap  $d1$ ,  $d3$ ,  $d4$ , and  $d5$  creates four internal structures ( $RR2$  and  $CR1$ ), where each of which constitutes an  $LC$  tank circuit ( $UL2$ ,  $UC7$ ,  $UL3$ ), ( $UL5$ ,  $UC8$ ,  $UL4$ ), ( $UL6$ ,  $UC10$ ,  $UL7$ ), ( $UL9$ ,  $UC12$ ,  $UL8$ )) and gap forms capacitance ( $UC11$ ,  $UC6$ ,  $UC18$ ,  $UC5$ ).  $UC15$ ,  $UC16$ ,  $UC13$ , and  $UC14$  form the gap between outer ( $RR1$ ) and internal ( $RR2$ ) ring structures. The center circle  $CR2$  is represented by inductor  $UL1$ , and its capacitance is minimal; hence, it is neglected

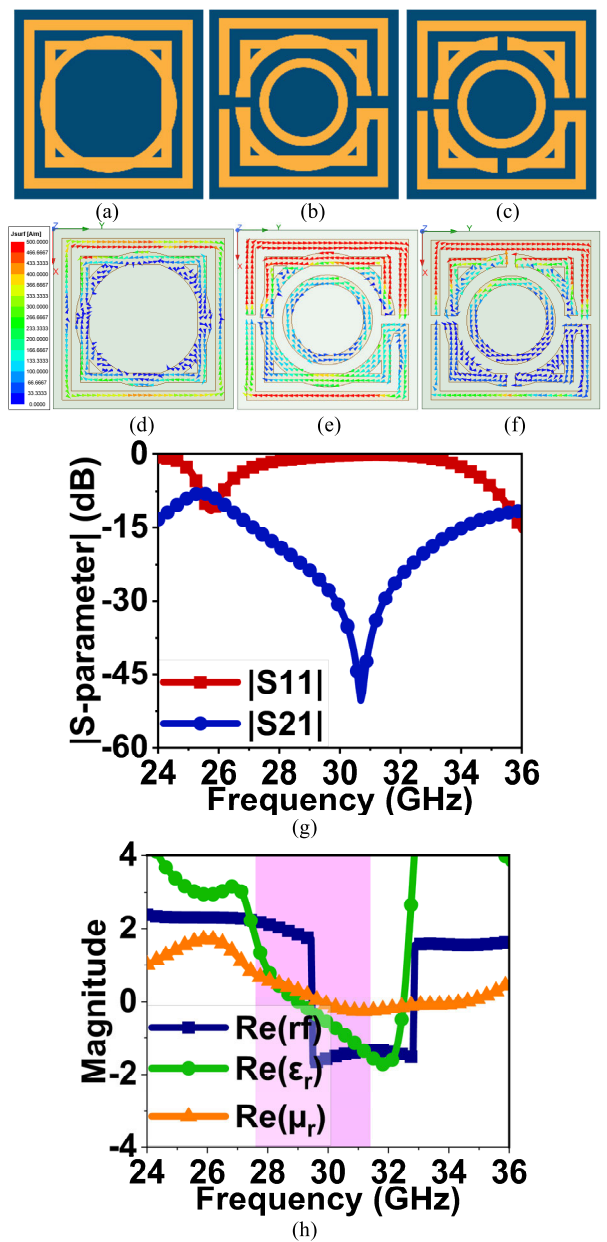


**FIGURE 13.** Evolution stages of metamaterial unit cell, (a) stage 1, (b) stage 2, (c) stage 3 - proposed unit cell. Surface current vector of a unit cell at various stages, (d) Stage 1 at  $25.68 \text{ GHz}$ , (e) Stage 2 at  $30.35 \text{ GHz}$ , (f) Stage 3 at  $30.7 \text{ GHz}$ , (g)  $|S\text{-parameter}|$  of proposed metamaterial unit cell, (h) Derived unit cell properties from S-parameters.

in the analysis. Ultimately, the unit cell is arranged in a periodic array structure with a certain gap in the  $x$  and  $y$  direction.  $UC19$ ,  $UC20$ ,  $UC21$ ,  $UC23$ , and  $UC24$  capacitance depict the gap between adjacent cells. The inductors and capacitors are tuned, and the desired S-parameter is similar to the simulated unit cell, as in Fig. 14(b).

## B. PARAMETRIC ANALYSIS OF METAMATERIAL LAYER

The unit cell is expanded to a  $2 \times 2$  periodic structures along the  $x$ -axis and  $y$ -axis, separated by distance  $d_x$  and  $d_y$ , as shown in Fig. 15(a). For  $d_x = d_y =$

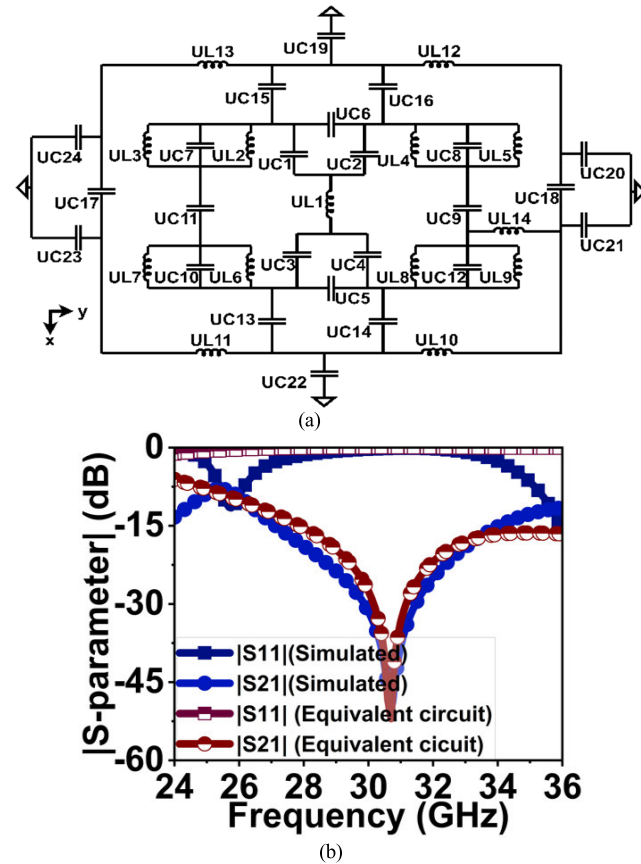


**FIGURE 14.** (a) Equivalent circuit of the unit cell with its inductance and capacitance values are:  $UC_1 = 0.032$ ,  $UC_2 = 0.001$ ,  $UC_3 = 0.001$ ,  $UC_4 = 0.018$ ,  $UC_5 = 1$ ,  $UC_6 = 0.872$ ,  $UC_7 = 0.08$ ,  $UC_8 = 0.095$ ,  $UC_9 = 0.032$ ,  $UC_{10} = 0.59$ ,  $UC_{11} = 0.001$ ,  $UC_{12} = 0.032$ ,  $UC_{13} = 0.132$ ,  $UC_{14} = 0.18$ ,  $UC_{15} = 0.1$ ,  $UC_{16} = 0.86$ ,  $UC_{17} = 0.001$ ,  $UC_{18} = 0.11$ ,  $UC_{19} = 0.2$ ,  $UC_{20} = 0.1$ ,  $UC_{21} = 0.13$ ,  $UC_{22} = 0.11$ ,  $UC_{23} = 0.23$ ,  $UC_{24} = 0.001$ ,  $UL_1 = 1.45$ ,  $UL_2 = 0.06$ ,  $UL_3 = 0.14$ ,  $UL_4 = 1.24$ ,  $UL_5 = 1.15$ ,  $UL_6 = 0.8$ ,  $UL_7 = 1.49$ ,  $UL_8 = 1.47$ ,  $UL_9 = 0.4$ ,  $UL_{10} = 0.23$ ,  $UL_{11} = 0.001$ ,  $UL_{12} = 0.68$ ,  $UL_{13} = 0.49$ , and  $UL_{14} = 0.1$  ( $UC$  are in pF and  $UL$  are in nH (except  $UL_{14}$ )). (b) S-parameter comparison of simulated and equivalent circuits of the unit cell.

0.2 mm, a single transmission zero (TZ) occurred at 30.45 GHz with a wide stop-band from 25.6–36 GHz. For 0.3 mm and 0.4 mm, two TZ are generated at 29.7 GHz and 30.7 GHz/31 GHz in Fig. 15(c) (due to brevity in the image, only a few plots are presented). Similarly, for  $d_x = d_y = 0.6/0.7$  mm, two TZ are generated at 29.7 GHz/29.25 GHz and 31.2 GHz/31.4 GHz. From the above parametric analysis, the  $d_x = d_y = 0.4$  mm is chosen to prepare the metamaterial reflective surface on  $2.25\lambda_0 \times 2.25\lambda_0$  substrate, as depicted in Fig. 15(b). The reason for selecting 0.4 mm is because the two TZ increase the attenuation; also, it has a transmission coefficient of -47 dB at both TZ. Further, the unit cell is expanded to an array of  $9 \times 9$  periodic structures.

The  $9 \times 9$  metamaterial reflective surface is placed below the antenna, separated by a distance of  $\frac{\lambda_0}{4} < d_{gap} < \frac{\lambda_0}{2}$  with air as a dielectric medium. The surface current on the unit cell in Fig. 13(f) indicates that the E-field orientation is

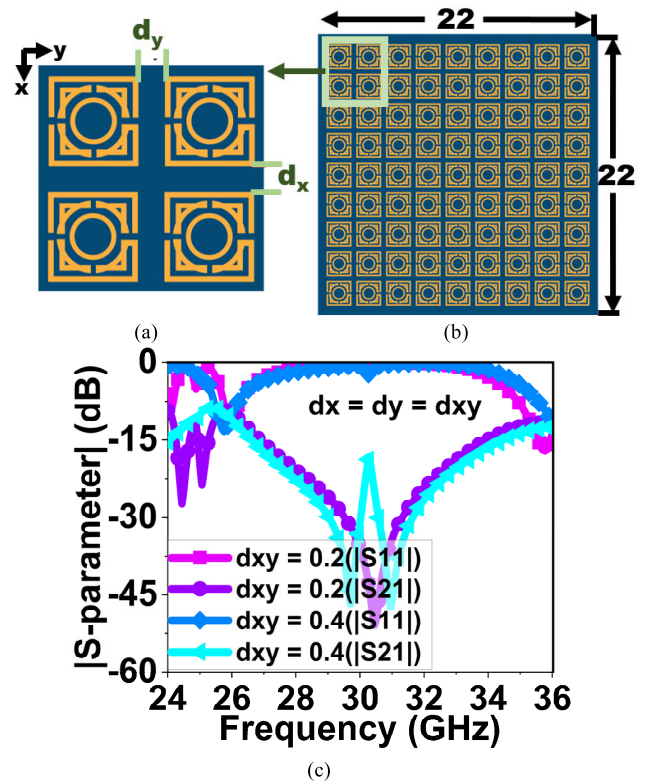


**FIGURE 15.** (a) Expanded view of four-unit cells along the x- and y-axis (b) A proposed  $9 \times 9$  periodic MTM structure. (c)  $|S\text{-parameter}|$  resultant of four-unit cells for varied distances of  $d_x$  and  $d_y$ .

along the y-axis, whereas the antenna E-field is along the x-axis (Fig. 8(b)). For the reflective surface to work correctly with the antenna, the E-field orientation of both structures should be aligned. Therefore, the reflective surface is rotated by  $90^\circ$  in line with the antenna when placed below. Multiple simulation iterations are performed at various  $d_{gap}$  distances between 3.44 mm to 3.49 mm to obtain the best results.

### C. MIMO ANTENNA PERFORMANCE WITH MTM REFLECTIVE SURFACE

With a  $d_{gap}$  of 3.45 mm, the MTM reflective surface has enhanced the antenna performance. The incident and reflected wave are in phase at this distance, leading to constructive radiation in the broadside direction with enhanced gain. It also improved impedance matching over a large spectrum, increasing the bandwidth. The 3D representation of this is shown in Fig. 1(a). The simulated  $|S\text{-parameter}|$  of the MIMO antenna with an MTM reflective surface without bend is shown in Fig. 16. It has achieved a bandwidth ranging from 23–32.77 GHz with an overall isolation of  $> 22$  dB.

As the antenna is designed for wearable applications, the  $|S\text{-parameter}|$  performance of the MIMO antenna with an MTM reflective surface is also studied. Fig. 17 shows the conformal along the x-axis and y-axis. The study is performed at three different radii: 40 mm, 50 mm, and 60 mm. When the antenna is bent along the x-axis, a slight drift in the resonance

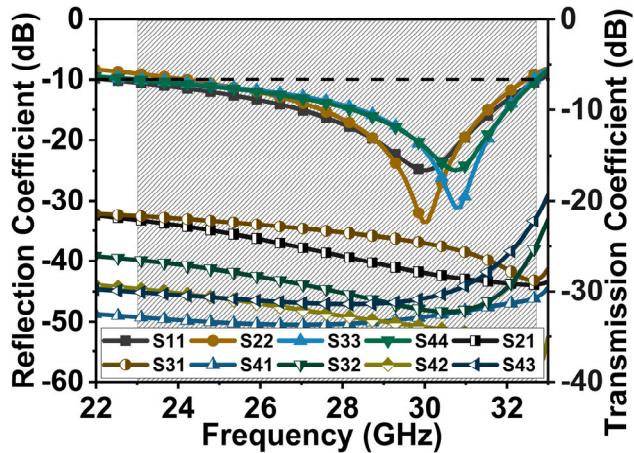


**FIGURE 16.** Simulated  $|S\text{-parameter}|$  results of proposed MIMO antenna with MTM reflective surface without bent.

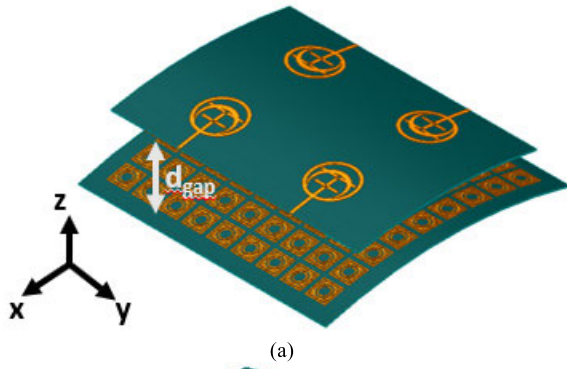


**FIGURE 17.** Bending analysis of the proposed MIMO antenna with MTM reflective surface. (a) Along the x-axis. (b) Along the y-axis.

is observed at 31.2 GHz. In the bent condition, the incident wave from the MIMO antenna on MTM surface reaches at different incident angles. The change in the incidence angle causes a variable phase in the reflected signal. Summation of this continuous phase-shift reflected wave with the incident wave leads to some distortion. Consequently, the resonance, bandwidth, and gain change are observed in Figs. 17(a), 17(b) and 18.

However, the bandwidth ranges from 26-33 GHz is achieved with an isolation  $|S_{21}| > 25$  dB. In the case of the y-axis bend, the proposed antenna has maintained bandwidth

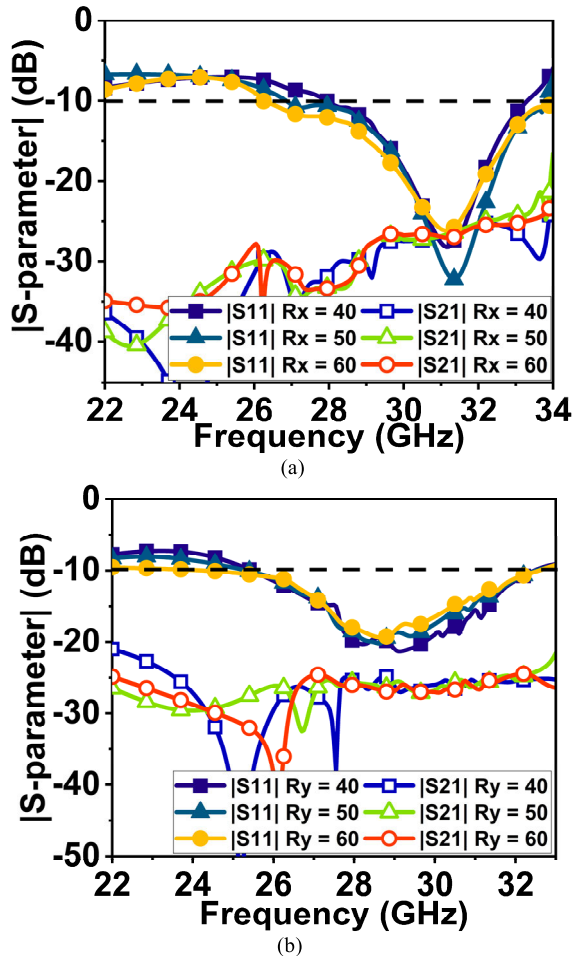


**FIGURE 18.** Simulated  $|S\text{-parameter}|$  results of the proposed MIMO antenna with MTM reflective surface with bent condition. (a) Along the x-axis. (b) Along the y-axis.

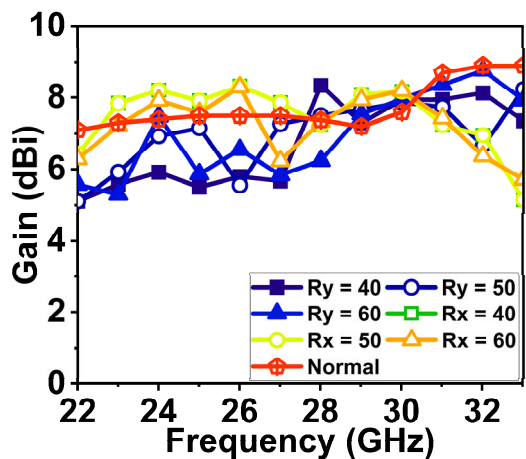


**FIGURE 19.** Simulated gain of proposed MIMO antenna with MTM under normal and bent conditions with different radii.

from 24.5-32 GHz with a shift in resonance close to 29 GHz. The isolation  $|S_{21}|$  is  $> 25$  dB even in the y-axis bend. Fig. 18 shows the simulated gain of the proposed antenna

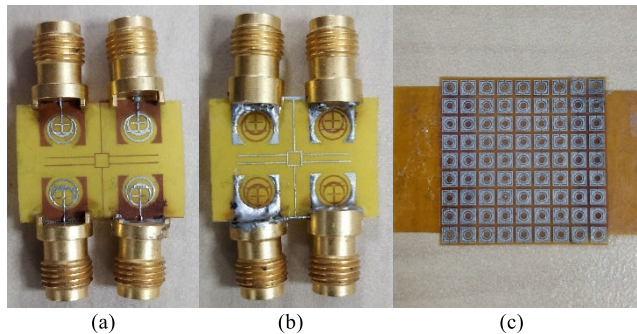


**FIGURE 20.** Prototype fabricated images. (a) Top view of proposed four-port MIMO antenna, (b) Bottom view of antenna. (c) A  $9 \times 9$  MTM reflective surface.

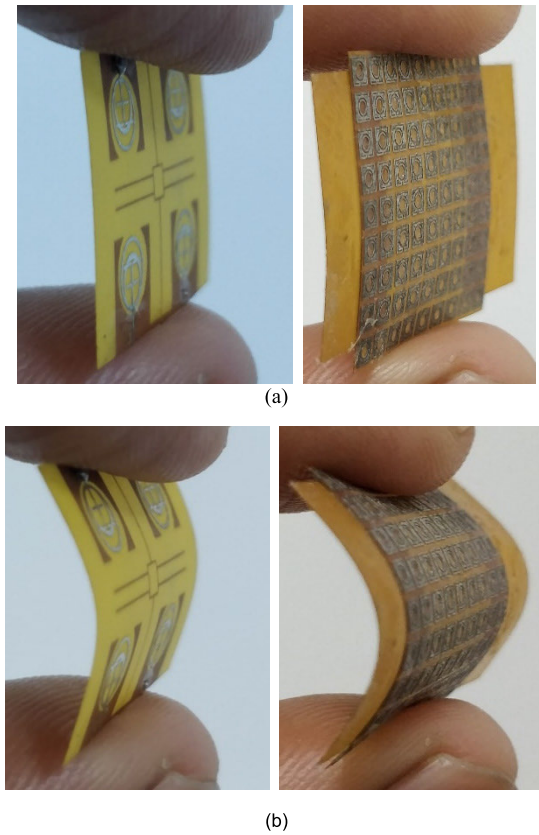


**FIGURE 21.** Illustration of the conformal orientation of the fabricated antenna. (a) Without conformal orientation. (b) Conformal orientation.

under normal and bent conditions. Under normal conditions, the gain is ranging from 7.2 to 8.7 dBi. However, the gain ranges from 5 to 8 dBi in the bend conditions.

## V. RESULTS AND DISCUSSION

The four-element MIMO antenna substrate dimension of Fig. 7 is slightly increased by 3 mm on either side of the y-axis. It provides the area to position spacers, which separates an antenna with an MTM reflective surface. Therefore, the final MIMO antenna dimension is  $1.63\lambda_0 \times 2.25\lambda_0$ , whereas

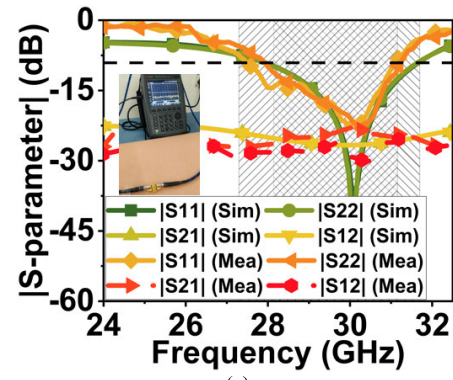


**FIGURE 22.** Simulated and measured  $|S\text{-parameter}|$  with gain plot. (a)  $|S\text{-parameter}|$  without MTM, (b)  $|S\text{-parameter}|$  with MTM reflective surface. (c) Gain plot.

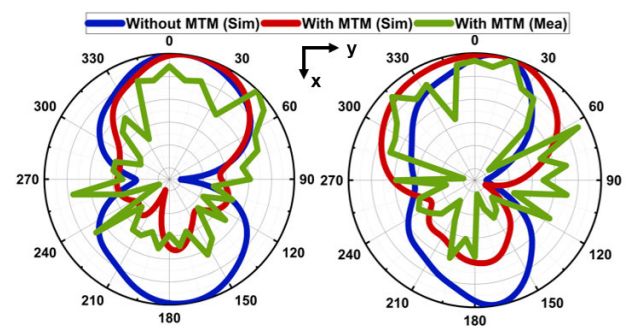


**FIGURE 23.** Normalized simulated and measured radiation pattern of four-element MIMO with and without MTM structure at  $f_0$ . (a) E-plane and (b) H-plane.

the size of the metamaterial reflective surface is  $2.25\lambda_0 \times 2.25\lambda_0$ .

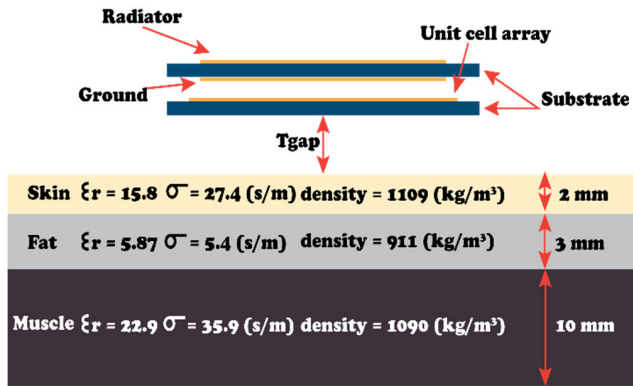


FIGURE 24. Phantom model of the human wrist for SAR analysis.

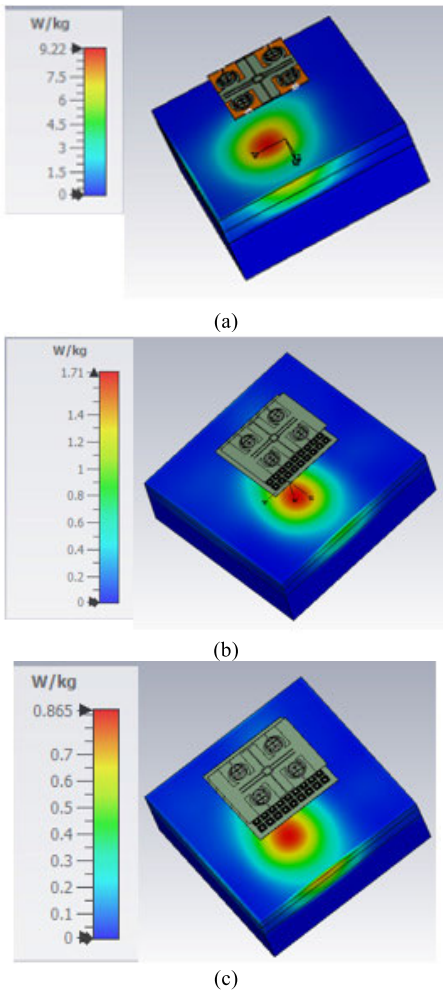
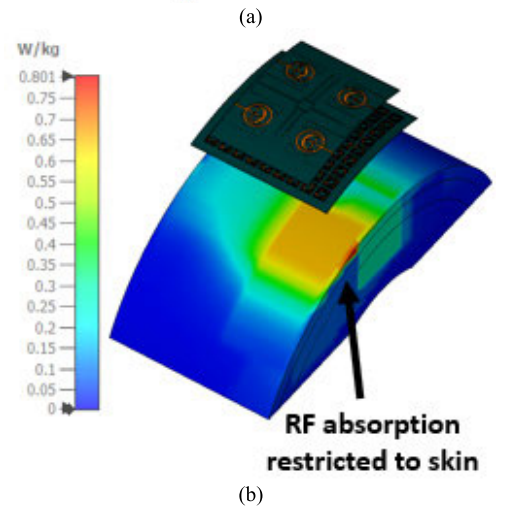
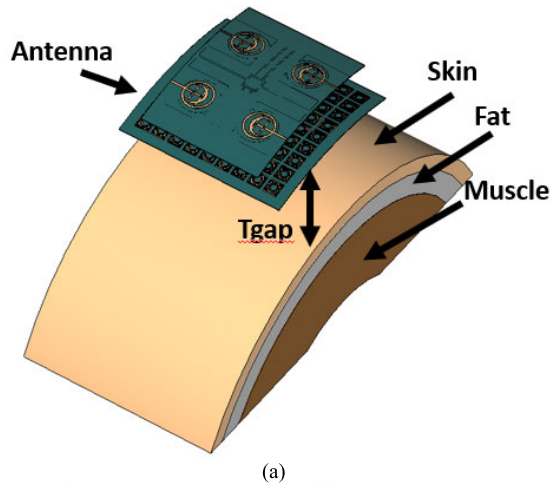
FIGURE 25. SAR results at 30.5 GHz: (a) Without MTM at  $T_{gap} = 10$  mm, (b) with MTM at  $T_{gap} = 10$  mm, input power 100mW, and (c) with MTM at  $T_{gap} = 10$  mm, input power 50mW.

FIGURE 26. Investigation of SAR performance under conformal orientation. (a) Antenna and phantom model representation. (b) Respective SAR results.

tion of the fabricated antenna and MTM reflective surface. The  $|S\text{-parameter}|$  is measured using VNA N9951A. A 2.4 mm end launch SMA connector (part no. 147-0701-261) from Johnson manufacturer (range 0-50 GHz) is used [47]. The simulation of a four-element MIMO antenna without an MTM reflective surface provided 28.27-31.64 GHz bandwidth with isolation  $> 25$  dB throughout the band, as shown in Fig. 22(a). The measured bandwidth is 27.60-31 GHz with an isolation of  $> 21$  dB.

The four-element MIMO antenna with MTM reflective surface at a distance  $d_{gap} = 3.45$  mm resulted in broadside radiation with enhanced bandwidth due to the summation of in-phase waves from the antenna and MTM reflected waves. Therefore, the simulated bandwidth range of the proposed MIMO antenna with MTM is 23-32.77 GHz with an isolation of 25 dB, and the measured bandwidth is 25.20-33.22 GHz with 22.5 dB isolation, as shown in Fig. 22(b). The slight deviation in results is due to fabrication, alignment, and testing tolerance. Also, the exact height of spacers in mm is difficult to achieve, which is why the deviation in measured results can also be seen. However, the variations are well

#### A. $|S\text{-PARAMETER}|$ AND RADIATION PATTERN MEASUREMENT

The proposed four-element MIMO antenna with a  $9 \times 9$  MTM reflective surface is fabricated, as shown in Fig. 20. Fig. 21 illustrates the conformal and non-conformal orienta-

**TABLE 1.** Comparative analysis of proposed work with existing designs.

Ref.	Dim	Port	Res (GHz)	BW	Iso (dB)	Gain (dBi)	RP	SAR (W/kg)	ECC	DG	CCL (b/s/Hz)	TARC (dB)	MEG (dB)
[13]	$1.83\lambda_0 \times 1.65\lambda_0$	8	11	5-40	22	5	Om	1.79	<0.01	-	<0.12	-	-
[21]	$1.9\lambda_0 \times 3\lambda_0$	2	25	23.9-31.4	21	6.1	Om	2.18/1.64	<0.003	>9.9	<0.26	23.4-30.5	0
[22]	$1.52\lambda_0 \times 1.2\lambda_0$	2	24	23.2-24.8	25	5	Dir	-	<0.2	>9.7	-	-	-
[23]	$0.48\lambda_0 \times 0.48\lambda_0$	8	6	4.8-30	18	6	Om	-	-	-	-	-	-
Proposed MIMO With MTM	$2.25\lambda_0 \times 2.25\lambda_0$	4	30.5	25.2-33	22.5	8.9	Dir	0.86/0.8	<0.3	>9.7	<0.28	22-33	0

Note: Ref – References, Dim – Dimensions, Res – Resonance, BW – Bandwidth, Iso – Isolation, RP – Radiation pattern, Bi – Bidirectional, Om – Omnidirectional, Dir – Directional, \*- Not available. (Note: Diversity metrics are marked for an entire band of interest)

within the acceptance limit. The maximum gain achieved by the proposed MIMO antenna without MTM is 6 dBi, with an average gain over the band is 5 dBi, as shown in Fig. 22(c). However, the gain of the antenna with the MTM reflective surface is increased to 8.9 dBi (maximum measured). However, the average gain is 7.8 dBi over the entire bandwidth.

The radiation pattern for the prototype antenna is measured in the anechoic chamber, where a millimeter wave horn antenna is used as a reference transmitting antenna. The testing antenna is a prototype fabricated four-element MIMO antenna with and without an MTM reflective surface. The four-element MIMO antenna without MTM reflective surface has bidirectional radiation with half-power beamwidth (HPBW) of  $63.56^\circ$  and  $64.86^\circ$  in E- and H-plane ( $\phi = 0^\circ$  and  $\phi = 90^\circ$  planes) (Figs. 23(a &b)), respectively. The simulated and measured radiation pattern of the proposed MIMO antenna with an MTM reflective surface has broadside radiation with HPBW of  $69.62^\circ$  and  $89.85^\circ$  in the E- and H-plane, as shown in Figs. 23(a & b), respectively.

### B. SPECIFIC ABSORPTION RATE (SAR) ANALYSIS AND MEASUREMENT

The various tissues of the human body have different compositions of water, fat, protein, and salt, which absorb the radio frequency (RF) energy differently. Absorption also depends on the frequency and strength of the electromagnetic energy. However, at mmWave frequencies, the absorption is restricted to the body surface (skin); thus, the penetration will be less [48]. The SAR standards defined by the Federal Communication Commission (FCC) and the International Commission on Non-Ionizing Radiation Protection (ICNIRP) are applicable for frequencies below 10 GHz (i.e., 1.6 W/kg and 2W/kg) [49]. For mmWave frequency, no specific standards are defined. So, the existing standards are being followed to validate the proposed MIMO antenna.

However, the SAR analysis of the proposed antenna is studied and compared with the existing standards. For this, a phantom model of three-layer tissue is created with a length and width of  $25 \times 25 \text{ mm}^2$ , as shown in Fig. 24. The

thickness of the tissue layer is as follows: skin = 2 mm, fat tissue = 3 mm, and muscle = 10 mm. The skin dielectric can be measured using an open-ended waveguide probe [50]. Its dielectric constant changes over the body at different regions [51]. Therefore, the dielectric constant and electrical conductivity of tissues at  $f_0$  are obtained from the ITIS Foundation database [52]. The permittivity ( $\epsilon_r$ ) is 15.80, 5.87, and 22.90, and the electrical conductivity  $\sigma$  (s/m) is 27.40, 5.40, and 35.90 for respective tissues.

The antenna structure is kept at varied distances  $T_{gap}$  above the phantom model to find the best SAR value. At  $T_{gap}$  of 10 mm and input power of 100 mW, the antenna without MTM resulted in a SAR value of 9.22 W/kg per 1g of tissue, as shown in Fig. 25(a) at 30.50 GHz. However, the proposed antenna with an MTM reflective surface at the same  $T_{gap}$  and input power resulted in a much reduced SAR of 1.72 W/kg (Fig. 25(b)). Further, the input power is reduced to 50 mW, which results in a reduced SAR of 0.86 W/kg with an MTM structure, as shown in Fig. 25(c). It can also be observed that the radiated energy is spread over the skin tissue and partly in the fat tissue, and there is no penetration to the muscle tissue.

Further, the RF energy absorption by the phantom model under conformal antenna orientation is investigated in Fig. 26(a). For this case, the bent condition of the antenna with MTM surface is taken at the radius of 40 mm, i.e.,  $R_y = 40$  mm. The same  $T_{gap}$  is maintained between the antenna and phantom model, as in Fig. 24. Under bent conditions, the proposed antenna with MTM reflective surface has demonstrated approximately similar SAR value as compared to the non-conformal orientation. It resulted in SAR of 0.801 W/kg for the input power of 50 mW. The results in Fig. 26(b) indicate that the RF energy penetration is restricted to the skin layer.

### C. ON-BODY MEASUREMENT

As the antenna is proposed for wearable applications, the reflection coefficient variation is studied for on-body measurement. The antenna is slightly bent when placed over the wrist, as shown in Fig. 27(a), resulting in a minor drift

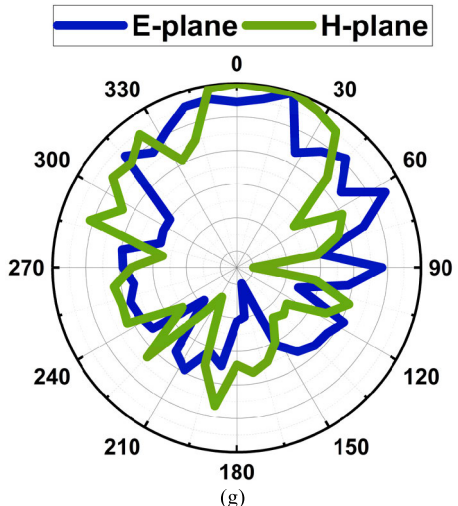
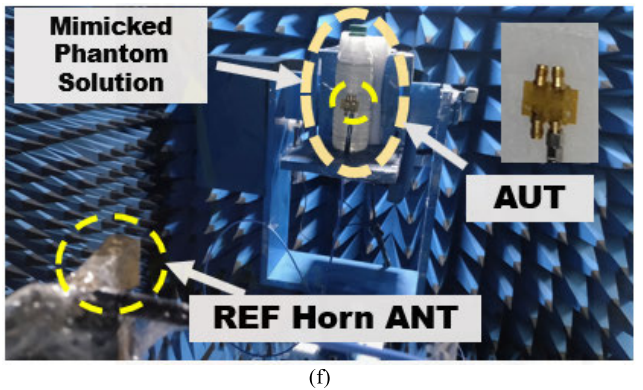
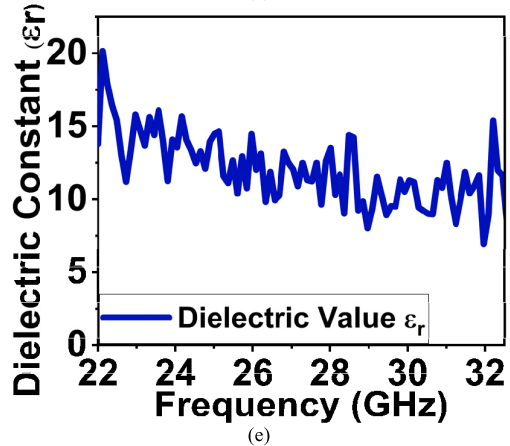
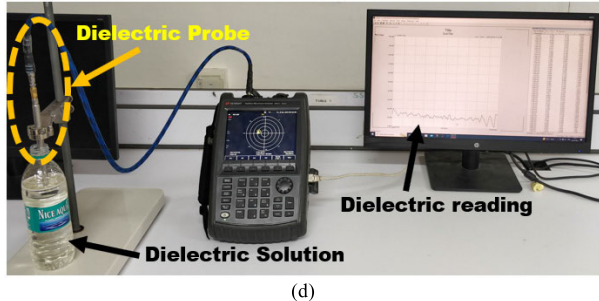
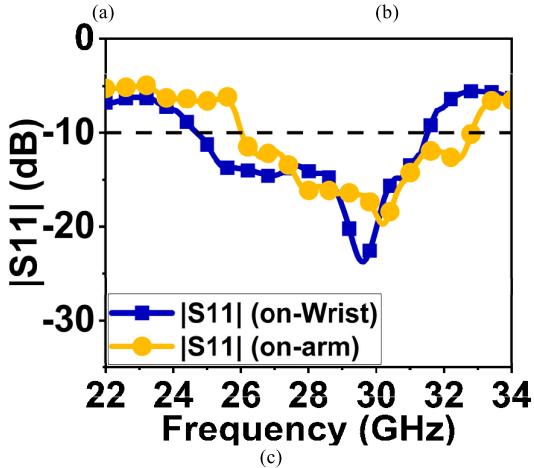


**FIGURE 27. (Continued.)** (a) Image of on-body measurement (wrist). (b) Image of on-body measurement (arm). (c)  $|S_{11}|$  results for on-body measurement. (d) Dielectric solution measurement setup. (e) Plot of dielectric value over frequency of prepared solution. (f) Anechoic chamber setup for radiation pattern measurement with a mimicked phantom. (g) Measured normalized radiation pattern of on-body measurement.

in bandwidth to 24.70–31.54 GHz, as shown in Fig. 27(c). However, the measurement at the arm, as shown in Fig. 27(b), resulted in a bandwidth of 26–32.80 GHz. Therefore, on-body measurement has reduced bandwidth by approximately 1.7 GHz due to the bending effect. The on-body measurement radiation pattern is performed by preparing a solution mimicking the dielectric value of the skin (approx. 15.8). The solution is prepared by a mixture of sucrose in dihydrogen oxide, which is measured using a dielectric probe kit and VNA, as shown in Fig. 27(d). The characteristic of the formulated solution has resulted in an average dielectric value ( $\epsilon_r$ ) of 12, as depicted in Fig. 27(e). Fig. 27(f) shows the anechoic chamber setup with a bottle filled with solution mimicking the phantom model for radiation pattern measurement. The on-body measurement radiation pattern of the proposed antenna with MTM reflective surface has broadside radiation with HPBW of  $62^\circ$  and  $61^\circ$  in E- and H-plane, as shown in Fig. 27(g).

**FIGURE 27.** (a) Image of on-body measurement (wrist). (b) Image of on-body measurement (arm). (c)  $|S_{11}|$  results for on-body measurement. (d) Dielectric solution measurement setup. (e) Plot of dielectric value over frequency of prepared solution. (f) Anechoic chamber setup for radiation pattern measurement with a mimicked phantom. (g) Measured normalized radiation pattern of on-body measurement.

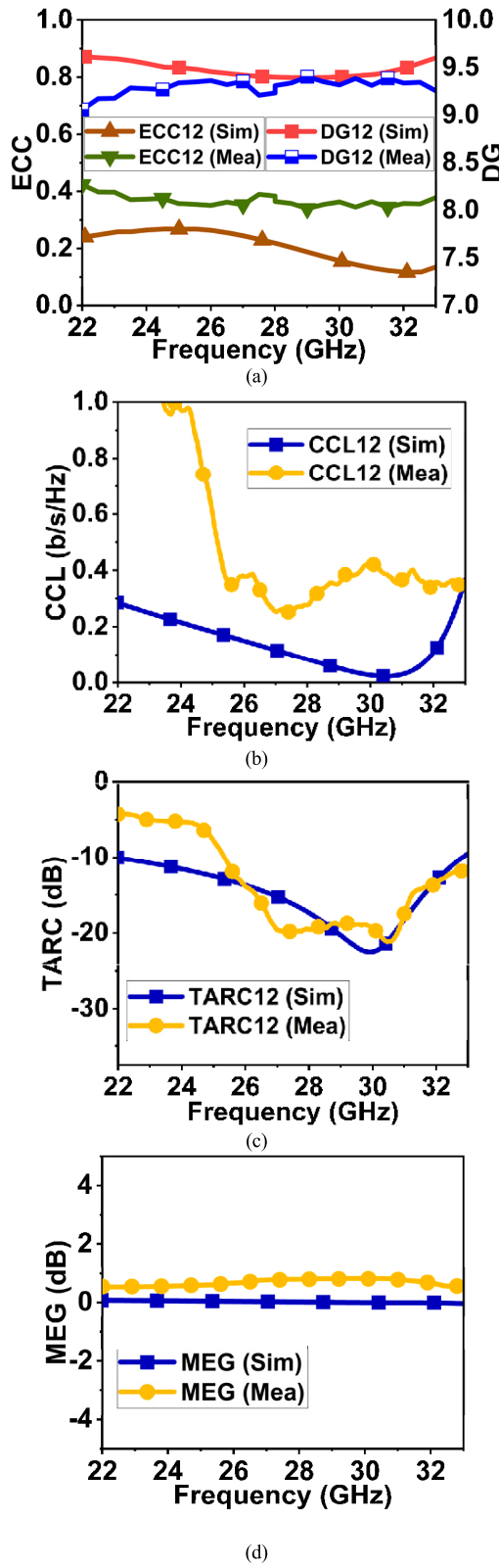


**FIGURE 28.** Diversity performance of MIMO antenna with MTM structure.  
(a) ECC and DG, (b) CCL, (c) TARC, and (d) MEG.

#### D. DIVERSITY PARAMETERS

The diversity parameters are evaluated for a proposed MIMO antenna loaded with MTM reflective surface. The envelope

correlation coefficient (ECC) is calculated using the equation defined in [22] from the radiation pattern.

The acceptable value of ECC is  $< 0.5$ ; for the proposed antenna, ECC resulted in  $< 0.4$ , as displayed in Fig. 28(a) (*due to brevity in the figures, only a few plots are shown*). The diversity gain is derived from the ECC; ideally, it should be 10. For the proposed structure,  $DG > 9.3$ , as obtained in Fig. 28(a). The channel capacity loss (CCL) of the MIMO antenna should have a bit error rate  $< 0.4$  b/s/Hz and be calculated as mentioned in [53]. For the proposed design,  $CCL < 0.25$  b/s/Hz, as shown in Fig. 28(b). The total active reflection coefficient (TARC) is calculated as proposed in [53]. The TARC should be  $< -10$  dB for the band of interest. The proposed antenna is well below the threshold range, as indicated in Fig. 28(c). The mean effective gain (MEG) is calculated using the equation defined in [53]. The proposed structure MEG is zero dB throughout the band of interest, as illustrated in Fig. 28(d).

#### E. COMPARATIVE ANALYSIS

The performance of the proposed MIMO antenna loaded with an MTM reflective surface is summarized and compared with the existing designs in Table 1. There are very few fully flexible MIMO antenna designs exist to-date. Hence, the comparison is performed with fully flexible and semi-flexible MIMO antennas. The proposed antenna has improved the directivity to broadside direction compared to [13], [21], and [23]. The obtained SAR value is much less than all other designs in Table 1. The proposed antenna has improved the gain compared to all other designs in Table 1. The proposed structure has also improved the bandwidth compared to [22], which also used a reflective surface. The proposed antenna has slightly improved the isolation compared to [13], [21], and [23]. The diversity parameters of the antenna are comparable with [13], [21], [22], and [23].

#### VI. CONCLUSION

The article has presented a four-element MIMO antenna for wearable applications as it is highly conformal and partially transparent due to the use of a polyimide substrate of 0.1 mm thickness. The single-element structure is a complex combination of circular rings and T-shape structures. Further, the single-element structure has been extended to a four-element MIMO antenna. The isolation of a four-element MIMO antenna has been improved using a decoupling structure in the ground plane, which consists of a rectangular ring, four open-ended strip lines, and two strip lines connecting the ground plane. The overall MIMO antenna profile was  $1.63\lambda_0 \times 2.25\lambda_0$ . The MIMO antenna has achieved a bandwidth of 27.60–31 GHz. The antenna performance has been improved by using a  $9 \times 9$  MTM reflective surface with stop-band characteristics from 26.27–36.49 dB with two transmission zeros. The size of the MTM reflective surface was  $2.25\lambda_0 \times 2.25\lambda_0$ . The four-element MIMO antenna with MTM reflective surface has a wide bandwidth of 25.20–33 GHz with a maximum gain of 8.9 dBi with broadside

radiation. The proposed antenna with an MTM surface has also suppressed the radio frequency energy penetration on the human body, resulting in an SAR of 0.86 and 0.8 W/kg for 1g of tissue for a distance of 10 mm. The results of on-body measurement and diversity parameters have been satisfactory. The proposed antenna is well suited for wristwatches, wristbands, and clothing 5G applications.

## REFERENCES

- [1] (2030). *Wearable Technology Market Share & Trends Report, 2030*. Accessed: Mar. 11, 2023. [Online]. Available: <https://www.grandviewresearch.com/industry-analysis/wearable-technology-market>
- [2] S. Kumar, D. Nandan, K. Srivastava, S. Kumar, H. Singh, M. Marey, H. Mostafa, and B. K. Kanaujia, "Wideband circularly polarized textile MIMO antenna for wearable applications," *IEEE Access*, vol. 9, pp. 108601–108613, 2021, doi: [10.1109/ACCESS.2021.3101441](https://doi.org/10.1109/ACCESS.2021.3101441).
- [3] A. Iqbal, A. Smida, A. J. Alazemi, M. I. Waly, N. K. Mallat, and S. Kim, "Wideband circularly polarized MIMO antenna for high data wearable biotelemetry devices," *IEEE Access*, vol. 8, pp. 17935–17944, 2020, doi: [10.1109/ACCESS.2020.2967397](https://doi.org/10.1109/ACCESS.2020.2967397).
- [4] M. Ikram, K. Sultan, M. F. Lateef, and A. S. M. Alqadami, "A road towards 6G communication—A review of 5G antennas, arrays, and wearable devices," *Electronics*, vol. 11, no. 1, p. 169, Jan. 2022, doi: [10.3390/electronics11010169](https://doi.org/10.3390/electronics11010169).
- [5] M. Marcus and B. Pattan, "Millimeter wave propagation: Spectrum management implications," *IEEE Microwave Mag.*, vol. 6, no. 2, pp. 54–62, Jun. 2005, doi: [10.1109/MMW.2005.1491267](https://doi.org/10.1109/MMW.2005.1491267).
- [6] H. Qiu, H. Liu, X. Jia, Z.-Y. Jiang, Y.-H. Liu, J. Xu, T. Lu, M. Shao, T.-L. Ren, and K. J. Chen, "Compact, flexible, and transparent antennas based on embedded metallic mesh for wearable devices in 5G wireless network," *IEEE Trans. Antennas Propag.*, vol. 69, no. 4, pp. 1864–1873, Apr. 2021, doi: [10.1109/TAP.2020.3035911](https://doi.org/10.1109/TAP.2020.3035911).
- [7] M. Ur-Rehman, N. A. Malik, X. Yang, Q. H. Abbasi, Z. Zhang, and N. Zhao, "A low profile antenna for millimeter-wave body-centric applications," *IEEE Trans. Antennas Propag.*, vol. 65, no. 12, pp. 6329–6337, Dec. 2017, doi: [10.1109/TAP.2017.2700897](https://doi.org/10.1109/TAP.2017.2700897).
- [8] S. F. Filani, M. O. Munoz, Q. H. Abbasi, and A. Alomainy, "Millimeter-wave liquid crystal polymer based conformal antenna array for 5G applications," *IEEE Antennas Wireless Propag. Lett.*, vol. 18, pp. 84–88, 2019, doi: [10.1109/LAWP.2018.2881303](https://doi.org/10.1109/LAWP.2018.2881303).
- [9] S. A. Busari, K. M. S. Huq, S. Mumtaz, L. Dai, and J. Rodriguez, "Millimeter-wave massive MIMO communication for future wireless systems: A survey," *IEEE Commun. Surveys Tuts.*, vol. 20, no. 2, pp. 836–869, 2nd Quart., 2018, doi: [10.1109/COMST.2017.2787460](https://doi.org/10.1109/COMST.2017.2787460).
- [10] P. Kumar, T. Ali, and M. P. M. M., "Highly isolated ultrawideband multiple input and multiple output antenna for wireless applications," *Eng. Sci.*, vol. 17, pp. 83–90, 2021, doi: [10.30919/es8d570](https://doi.org/10.30919/es8d570).
- [11] M. Hussain, W. A. Awan, E. M. Ali, M. S. Alzaidi, M. Alsharef, D. H. Elkamchouchi, A. Alzahrani, and M. F. A. Sree, "Isolation improvement of parasitic element-loaded dual-band MIMO antenna for mm-wave applications," *Micromachines*, vol. 13, no. 11, p. 1918, Nov. 2022, doi: [10.3390/mi13111918](https://doi.org/10.3390/mi13111918).
- [12] A. A. Ibrahim and W. A. E. Ali, "High gain, wideband and low mutual coupling AMC-based millimeter wave MIMO antenna for 5G NR networks," *AEU Int. J. Electron. Commun.*, vol. 142, Dec. 2021, Art. no. 153990, doi: [10.1016/j.aeue.2021.153990](https://doi.org/10.1016/j.aeue.2021.153990).
- [13] A. R. H. Alhawari, T. Saeidi, A. H. M. Almawgani, A. T. Hindi, H. Alghamdi, T. Alsuwian, S. A. B. Awwad, and M. A. Imran, "Wearable metamaterial dual-polarized high isolation UWB MIMO Vivaldi antenna for 5G and satellite communications," *Micromachines*, vol. 12, no. 12, p. 1559, Dec. 2021, doi: [10.3390/mi12121559](https://doi.org/10.3390/mi12121559).
- [14] F. Wang, Z. Duan, X. Wang, Q. Zhou, and Y. Gong, "High isolation millimeter-wave wideband MIMO antenna for 5G communication," *Int. J. Antennas Propag.*, vol. 2019, pp. 1–12, May 2019, doi: [10.1155/2019/4283010](https://doi.org/10.1155/2019/4283010).
- [15] K. D. Ayinala and P. K. Sahu, "Isolation enhanced compact dual-band quad-element MIMO antenna with simple parasitic decoupling elements," *AEU Int. J. Electron. Commun.*, vol. 142, Dec. 2021, Art. no. 154013, doi: [10.1016/j.aeue.2021.154013](https://doi.org/10.1016/j.aeue.2021.154013).
- [16] M. Irshad Khan, S. Liu, M. Kabir Khan, and S. Ur Rahman, "Eight elements mm-wave MIMO antenna for anti-collision radar sensing application with novel hybrid techniques," *AEU Int. J. Electron. Commun.*, vol. 167, Jul. 2023, Art. no. 154687, doi: [10.1016/j.aeue.2023.154687](https://doi.org/10.1016/j.aeue.2023.154687).
- [17] D. A. Sehra, M. Asif, W. A. Shah, J. Khan, I. Ullah, M. Ibrar, S. Jan, M. Alibakhshikenari, F. Falcone, and E. Limiti, "Metasurface-based wideband MIMO antenna for 5G millimeter-wave systems," *IEEE Access*, vol. 9, pp. 125348–125357, 2021, doi: [10.1109/ACCESS.2021.3110905](https://doi.org/10.1109/ACCESS.2021.3110905).
- [18] K. C. Ravi and J. Kumar, "Multi-directional wideband unit-element MIMO antenna for FR-2 band 5G array applications," *Iranian J. Sci. Technol. Trans. Electr. Eng.*, vol. 46, no. 2, pp. 311–317, Jun. 2022, doi: [10.1007/s40998-022-00486-5](https://doi.org/10.1007/s40998-022-00486-5).
- [19] Z. Wani, M. P. Abegaonkar, and S. K. Koul, "Thin planar metasurface lens for millimeter-wave MIMO applications," *IEEE Trans. Antennas Propag.*, vol. 70, no. 1, pp. 692–696, Jan. 2022, doi: [10.1109/TAP.2021.3098571](https://doi.org/10.1109/TAP.2021.3098571).
- [20] S. Tariq, S. I. Naqvi, N. Hussain, and Y. Amin, "A metasurface-based MIMO antenna for 5G millimeter-wave applications," *IEEE Access*, vol. 9, pp. 51805–51817, 2021, doi: [10.1109/ACCESS.2021.3069185](https://doi.org/10.1109/ACCESS.2021.3069185).
- [21] R. N. Tiwari, V. Kaim, P. Singh, T. Khan, and B. K. Kanaujia, "Semi-flexible diversified circularly polarized millimeter-wave MIMO antenna for wearable biotechnologies," *IEEE Trans. Antennas Propag.*, vol. 71, no. 5, pp. 3968–3982, May 2023, doi: [10.1109/TAP.2023.3255507](https://doi.org/10.1109/TAP.2023.3255507).
- [22] A. Iqbal, A. Basir, A. Smida, N. K. Mallat, I. Elfergani, J. Rodriguez, and S. Kim, "Electromagnetic bandgap backed millimeter-wave MIMO antenna for wearable applications," *IEEE Access*, vol. 7, pp. 111135–111144, 2019, doi: [10.1109/ACCESS.2019.2933913](https://doi.org/10.1109/ACCESS.2019.2933913).
- [23] S. N. Mahmood, A. J. Ishak, A. Jalal, T. Saeidi, S. Shafie, A. C. Soh, M. A. Imran, and Q. H. Abbasi, "A bra monitoring system using a miniaturized wearable ultra-wideband MIMO antenna for breast cancer imaging," *Electronics*, vol. 10, no. 21, p. 2563, Oct. 2021, doi: [10.3390/electronics10212563](https://doi.org/10.3390/electronics10212563).
- [24] M. Ur-Rehman, M. Adekanye, and H. T. Chattha, "Tri-band millimetre-wave antenna for body-centric networks," *Nano Commun. Netw.*, vol. 18, pp. 72–81, Dec. 2018, doi: [10.1016/j.nancom.2018.03.003](https://doi.org/10.1016/j.nancom.2018.03.003).
- [25] U. Farooq and G. M. Rather, "A miniaturised Ka/V dual band millimeter wave antenna for 5G body centric network applications," *Alexandria Eng. J.*, vol. 61, no. 10, pp. 8089–8096, Oct. 2022, doi: [10.1016/j.aej.2022.01.044](https://doi.org/10.1016/j.aej.2022.01.044).
- [26] S. Ahmad, H. Boubakar, S. Naseer, M. E. Alim, Y. A. Sheikh, A. Ghaffar, A. J. A. Al-Gburi, and N. O. Parchin, "Design of a tri-band wearable antenna for millimeter-wave 5G applications," *Sensors*, vol. 22, no. 20, p. 8012, Oct. 2022, doi: [10.3390/s22208012](https://doi.org/10.3390/s22208012).
- [27] T. Govindan, S. K. Palaniswamy, M. Kanagasabai, T. R. Rao, M. G. N. Alsath, S. Kumar, S. Velan, M. Marey, and A. Aggarwal, "On the design and performance analysis of wristband MIMO/diversity antenna for smart wearable communication applications," *Sci. Rep.*, vol. 11, no. 1, p. 21917, Nov. 2021, doi: [10.1038/s41598-021-01326-y](https://doi.org/10.1038/s41598-021-01326-y).
- [28] E. M. Wissem, I. Sfar, L. Osman, and J.-M. Ribeiro, "A textile EBG-based antenna for future 5G-IoT millimeter-wave applications," *Electronics*, vol. 10, no. 2, p. 154, Jan. 2021, doi: [10.3390/electronics10020154](https://doi.org/10.3390/electronics10020154).
- [29] M. Wagih, G. S. Hilton, A. S. Weddell, and S. Beeby, "Millimeter-wave power transmission for compact and large-area wearable IoT devices based on a higher order mode wearable antenna," *IEEE Internet Things J.*, vol. 9, no. 7, pp. 5229–5239, Apr. 2022, doi: [10.1109/JIOT.2021.3107594](https://doi.org/10.1109/JIOT.2021.3107594).
- [30] A. Kavitha and J. N. Swaminathan, "Design of flexible textile antenna using FR4, jeans cotton and Teflon substrates," *Microsyst. Technol.*, vol. 25, no. 4, pp. 1311–1320, Apr. 2019, doi: [10.1007/s00542-018-4068-y](https://doi.org/10.1007/s00542-018-4068-y).
- [31] G. K. Soni, D. Yadav, and A. Kumar, "Design consideration and recent developments in flexible, transparent and wearable antenna technology: A review," *Trans. Emerg. Telecommun. Technol.*, vol. 35, no. 1, p. e4894, Jan. 2024, doi: [10.1002/ett.4894](https://doi.org/10.1002/ett.4894).
- [32] H. S. Haggerty and H. S. Lusted, "Histological reaction to polyimide films in the cochlea," *Acta Oto-Laryngologica*, vol. 107, nos. 1–2, pp. 13–22, Jan. 1989, doi: [10.3109/00016488909127474](https://doi.org/10.3109/00016488909127474).
- [33] H. R. Khaleel, H. M. Al-Rizzo, D. G. Rucker, and S. Mohan, "A compact polyimide-based UWB antenna for flexible electronics," *IEEE Antennas Wireless Propag. Lett.*, vol. 11, pp. 564–567, 2012, doi: [10.1109/LAWP.2012.2199956](https://doi.org/10.1109/LAWP.2012.2199956).
- [34] B. G. P. Shariff, S. Pathan, P. R. Mane, and T. Ali, "Characteristic mode analysis based highly flexible antenna for millimeter wave wireless applications," *J. Infr., Millim., Terahertz Waves*, vol. 45, nos. 1–2, pp. 1–26, Feb. 2024.

- [35] M. F. Abedin and M. Ali, "Modifying the ground plane and its effect on planar inverted-F antennas (PIFAs) for mobile phone handsets," *IEEE Antennas Wireless Propag. Lett.*, vol. 2, pp. 226–229, 2003, doi: [10.1109/LAWP.2003.819669](https://doi.org/10.1109/LAWP.2003.819669).
- [36] Z. Ning Chen, T. S. P. See, and X. Qing, "Small printed ultrawideband antenna with reduced ground plane effect," *IEEE Trans. Antennas Propag.*, vol. 55, no. 2, pp. 383–388, Feb. 2007, doi: [10.1109/TAP.2006.889823](https://doi.org/10.1109/TAP.2006.889823).
- [37] C. A. Balanis, *Antenna Theory: Analysis and Design*, 4th ed. Hoboken, NJ, USA: Wiley, 2016.
- [38] A. Toktas, M. B. Bicer, A. Kayabasi, D. Ustun, A. Akdagli, and K. Kurt, "A novel and simple expression to accurately calculate the resonant frequency of annular-ring microstrip antennas," *Int. J. Microwave Wireless Technol.*, vol. 7, no. 6, pp. 727–733, Dec. 2015, doi: [10.1017/s1759078714000890](https://doi.org/10.1017/s1759078714000890).
- [39] Y. Wang and Z. Du, "A wideband printed dual-antenna system with a novel neutralization line for mobile terminals," *IEEE Antennas Wireless Propag. Lett.*, vol. 12, pp. 1428–1431, 2013, doi: [10.1109/LAWP.2013.2287199](https://doi.org/10.1109/LAWP.2013.2287199).
- [40] M. Li, L. Jiang, and K. L. Yeung, "A general and systematic method to design neutralization lines for isolation enhancement in MIMO antenna arrays," *IEEE Trans. Veh. Technol.*, vol. 69, no. 6, pp. 6242–6253, Jun. 2020, doi: [10.1109/TVT.2020.2984044](https://doi.org/10.1109/TVT.2020.2984044).
- [41] T. Pei, L. Zhu, J. Wang, and W. Wu, "A low-profile decoupling structure for mutual coupling suppression in MIMO patch antenna," *IEEE Trans. Antennas Propag.*, vol. 69, no. 10, pp. 6145–6153, Oct. 2021, doi: [10.1109/TAP.2021.3098565](https://doi.org/10.1109/TAP.2021.3098565).
- [42] M. U. A. Khan, R. Raad, F. Tubbal, P. I. Theoharis, S. Liu, and J. Foroughi, "Bending analysis of polymer-based flexible antennas for wearable, general IoT applications: A review," *Polymers*, vol. 13, no. 3, p. 357, Jan. 2021, doi: [10.3390/polym13030357](https://doi.org/10.3390/polym13030357).
- [43] M. L. S. N. S. Lakshmi, B. T. P. Madhav, H. Khan, and P. V. V. Kishore, "A frequency and pattern reconfigurable asymmetric ground antenna on flexible polyimide material for LTE, Wi-Fi, WLAN and fixed satellite applications," *Flexible Printed Electron.*, vol. 5, no. 2, Jun. 2020, Art. no. 025007, doi: [10.1088/2058-8585/ab8f35](https://doi.org/10.1088/2058-8585/ab8f35).
- [44] P. Kumar, T. Ali, and M. M. M. Pai, "Electromagnetic metamaterials: A new paradigm of antenna design," *IEEE Access*, vol. 9, pp. 18722–18751, 2021, doi: [10.1109/ACCESS.2021.3053100](https://doi.org/10.1109/ACCESS.2021.3053100).
- [45] M. Pallavi, P. Kumar, T. Ali, and S. B. Shenoy, "Modeling of a negative refractive index metamaterial unit-cell and array for aircraft surveillance applications," *IEEE Access*, vol. 10, pp. 99790–99812, 2022, doi: [10.1109/ACCESS.2022.3206358](https://doi.org/10.1109/ACCESS.2022.3206358).
- [46] A. B. Numan and M. S. Sharawi, "Extraction of material parameters for metamaterials using a full-wave simulator [Education Column]," *IEEE Antennas Propag. Mag.*, vol. 55, no. 5, pp. 202–211, Oct. 2013, doi: [10.1109/MAP.2013.6735515](https://doi.org/10.1109/MAP.2013.6735515).
- [47] SMA Connector. Accessed: Feb. 1, 2024. [Online]. Available: <https://www.belfuse.com/resources/catalogs/cinchconnectivitysolutions/johnson/ca-ccs-john-mmwave-catalog.pdf>
- [48] D. K. Ghodgaonkar, O. P. Gandhi, and M. F. Iskander, "Complex permittivity of human skin in vivo in the frequency band 26.5–60 GHz," in *Proc. IEEE Antennas Propag. Soc. Int. Symp.*, UT, USA: IEEE, Jul. 2000, pp. 1100–1103, doi: [10.1109/APS.2000.875414](https://doi.org/10.1109/APS.2000.875414).
- [49] G. Ziegelberger, R. Croft, M. Feychting, A. C. Green, A. Hirata, G. D'Inzeo, K. Jokela, S. Loughran, C. Marino, S. Miller, G. Oftedal, T. Okuno, E. van Rongen, M. Röösli, Z. Sienkiewicz, J. E. H. Tattersall, and S. Watanabe, "Guidelines for limiting exposure to electromagnetic fields (100 kHz to 300 GHz)," *Health Phys.*, vol. 118, no. 5, pp. 483–524, 2020, doi: [10.1097/HP.00000000000001210](https://doi.org/10.1097/HP.00000000000001210).
- [50] Y. Gao, M. T. Ghasr, M. Nacy, and R. Zoughi, "Towards accurate and wideband in vivo measurement of skin dielectric properties," *IEEE Trans. Instrum. Meas.*, vol. 68, no. 2, pp. 512–524, Feb. 2019, doi: [10.1109/TIM.2018.2849519](https://doi.org/10.1109/TIM.2018.2849519).
- [51] S. A. R. Naqvi, M. Manoufali, B. Mohammed, A. T. Mobashsher, D. Foong, and A. M. Abbosh, "In vivo human skin dielectric properties characterization and statistical analysis at frequencies from 1 to 30 GHz," *IEEE Trans. Instrum. Meas.*, vol. 70, pp. 1–10, 2021, doi: [10.1109/TIM.2020.3036767](https://doi.org/10.1109/TIM.2020.3036767).
- [52] (2023). TISSUE DB? IT'S Foundation. Accessed: Apr. 4, 2023. [Online]. Available: <https://itis.swiss/virtual-population/tissue-properties/database/>
- [53] K. Vasu Babu, S. Das, G. Varshney, G. N. J. Sree, and B. T. P. Madhav, "A micro-scaled graphene-based tree-shaped wideband printed MIMO antenna for terahertz applications," *J. Comput. Electron.*, vol. 21, no. 1, pp. 289–303, Feb. 2022, doi: [10.1007/s10825-021-01831-3](https://doi.org/10.1007/s10825-021-01831-3).



**B. G. PARVEEZ SHARIFF** (Graduate Student Member, IEEE) received the B.E. degree in telecommunication engineering and the M.Tech. degree in digital electronics and communication systems from Visvesvaraya Technological University, Belagavi, India, in 2007 and 2009, respectively. He is currently pursuing the Ph.D. degree with the Department of Electronics and Communication Engineering, Manipal Institute of Technology, Manipal, India. His research interests include microstrip antenna, array antenna, flexible antenna, and metamaterial structure. He is a member of LMISTE, India.



**TANWEER ALI** (Senior Member, IEEE) is currently an Associate Professor with the Department of Electronics and Communication Engineering, Manipal Institute of Technology, Manipal Academy of Higher Education, Manipal. He is an active researcher in the field of microstrip antennas, wireless communication, and microwave imaging. He has been listed in the top 2% scientists across the world for the years 2021 and 2022 by the prestigious list published by Stanford University, USA, indexed by Scopus. He has published more than 130 papers in reputed Web of Science (SCI) and Scopus-indexed journals and conferences. He has led seven Indian patents, of which three have been published. He is on the Board of a Reviewer of journals, such as the IEEE TRANSACTIONS ON ANTENNAS AND PROPAGATION, IEEE ANTENNAS AND WIRELESS PROPAGATION LETTERS, and IEEE ACCESS.



**PALLAVI R. MANE** (Senior Member, IEEE) received the B.E. degree in electronics and communication engineering from the Gogte Institute of Technology, India, in 1996, the M.Tech. degree in digital electronics and advanced communication from the National Institute of Technology, Surathkal, Karnataka, India, in 2002, and the Ph.D. degree in electronics and communication engineering from Manipal Institute of Technology (MIT), Manipal Academy of Higher Education (MAHE), Manipal, in 2014, for the thesis in network coding. She is currently a Professor with the Department of ECE, MIT, MAHE. She has authored several papers at international conferences and journal proceedings. Her research interests include network coding, source, channel coding, communication engineering, and artificial intelligence.



**MOHAMMED GULAM NABI ALSATH** (Senior Member, IEEE) received the B.E. and M.E. degrees from the College of Engineering Guindy, Anna University, Chennai, and the Ph.D. degree in automotive antennas from Anna University. He is currently an Associate Professor with the Department of Electronics and Communication Engineering, College of Engineering Guindy, Anna University. His research interests include microwave components and circuits, antenna engineering, signal integrity analysis, and solutions to EMI problems.



**PRADEEP KUMAR** received the bachelor's, M.E., and Ph.D. degrees in electronics and communication engineering, in 2003, 2005, and 2009, respectively. He was a Postdoctoral Researcher with the Autonomous University of Madrid, Spain. He is currently with the University of KwaZulu-Natal, South Africa. He has over 15 years of experience in academics and research. He has held various positions, such as a lecturer, a senior lecturer, an assistant professor, and an associate professor. He is the author of many research papers published in various peer-reviewed journals/conferences. His current research interests include antennas, antenna arrays, and wireless communications. He is registered as a Professional Engineer with the Engineering Council of South Africa. He is serving as a Reviewer/a TPC Member for many journals/conferences, such as IEEE TRANSACTIONS ON ANTENNAS AND PROPAGATION and IEEE ACCESS.



**AHMED A. KISHK** (Life Fellow, IEEE) has been a Professor with Concordia University, Montreal, QC, Canada, since 2011, and the Tier 1 Canada Research Chair of Advanced Antenna Systems. He has published more than 430 refereed journal articles and 520 international conference papers, and 125 local and regional conference papers. He has coauthored four books and several chapters and was the editor of six books. He offered several short courses at international conferences. His current research interest includes electromagnetic applications. He has recently worked on millimeter-wave antennas for 5G/6G applications, analog beamforming networks, electromagnetic bandgap, phased array antennas, reflectors/transmit arrays, and wearable antennas. In addition, he is a pioneer in dielectric resonator antennas, microstrip antennas, small antennas, microwave sensors, multi-function antennas, microwave circuits, and feeds for parabolic reflectors. He was a member of the AP-S AdCom, from 2013 to 2015, and the 2017 AP-S President. He is a member of several IEEE societies, such as the Antennas and Propagation Society, Microwave Theory and Techniques, Electromagnetic Compatibility, Communications, Vehicular Technology Society, and Signal Processing. He is a Senior Member of the International Union of Radio Science Commission B.



**SAMEENA PATHAN** is currently an Assistant Professor with the Department of Information and Communication Technology, Manipal Institute of Technology, Manipal Academy of Higher Education, Manipal. Her research interests include pattern recognition, medical image analysis, artificial intelligence, and machine learning.



**TAIMOOR KHAN** (Senior Member, IEEE) received the Diploma (Polytechnic) degree in electronics engineering from the Board of Technical Education, Uttar Pradesh, India, in 2001, the Graduate degree in electronics and communication engineering from the Institution of Engineers, Kolkata, India, in 2005, the master's degree in communication engineering from the Shobhit Institute of Engineering and Technology, Meerut, India, in 2009, and the Ph.D. degree in electronics and communication engineering from the National Institute of Technology Patna, India, in 2014. He is currently an Associate Professor with the Department of Electronics and Communication Engineering, National Institute of Technology Silchar, India. His research interests include printed microwave and millimeter-wave circuits, electromagnetic bandgap structures, dielectric resonator antennas, and artificial intelligence paradigms in electromagnetics.

Received June 18, 2020, accepted June 23, 2020, date of publication June 30, 2020, date of current version July 20, 2020.

Digital Object Identifier 10.1109/ACCESS.2020.3006076

# Design of Smartwatch Integrated Antenna With Polarization Diversity

BUYUN WANG<sup>ID</sup><sup>1</sup> AND SEN YAN<sup>ID</sup><sup>1,2</sup>, (Member, IEEE)

<sup>1</sup>School of Information and Communications Engineering, Xi'an Jiaotong University, Xi'an 710049, China

<sup>2</sup>Shenzhen Research School, Xi'an Jiaotong University, Shenzhen 518057, China

Corresponding author: Sen Yan (sen.yan@xjtu.edu.cn)

This work was supported in part by the National Natural Science Foundation of China under Grant 61901351, in part by the Technology Program of Shenzhen under Grant JCYJ20180306170841629, and in part by the Outstanding Scientific and Technological Programs Foundation for the Returned Overseas Chinese Scholars of Shaanxi province under Grant 2018014.

**ABSTRACT** A design of smartwatch integrated antenna with polarization diversity is proposed. An annular ring is integrated in the framework of smartwatch, and excited by two ports. One port is fed by a coplanar waveguide (CPW) line loaded with a T-shaped matching network, and the other is fed by a coplanar strip line (CPS). The overall model of the proposed antenna has a cylindrical shape with 38 mm diameter and 7.5 mm thickness. A metallic plate is located at the backside of the antenna to mimic the shell of smartwatch. The prototype is fabricated and measured, and the measured results agree well with the numerical ones. The two ports have orthometric radiation patterns and can cover the 2.4 GHz wireless local area network (WLAN) band. The gain of the antenna is higher than 3.2 dBi in free space. The proposed antenna is also analyzed with a cubic tissue model and a wrist model in different distances between the proposed antenna and human models. The performances on body scenarios are also acceptable. The values of specific absorption rate (SAR) in the cubic tissue model and wrist model are below the limitations set by both the Federal Communication Commission (FCC) and the European Telecommunication Standards Institute (ETSI). Envelope correlation coefficient (ECC) shows proposed antenna can be used in multiple input multiple output (MIMO) applications. The influence of battery and printed circuits board assembly (PCBA) on S parameters is obvious, and gain and radiation efficiency are not much affected.

**INDEX TERMS** Wireless body area network (WBAN), wearable antenna, smartwatch integrated antenna, polarization diversity, cubic tissue model, wrist model, specific absorption rate (SAR), Envelope correlation coefficient (ECC).

## I. INTRODUCTION

Wireless body area network (WBAN) is a small communication network attached to the body. In recent years, it has attracted increasing attention because it can play an important part in medical detection, fitness training, health care and emergency rescue [1]. As one of the critical components in wearable smart devices, wearable antenna can transmit the microwave signals in the wireless communication systems between the devices and sensors [2]. Smartwatch is one of the most favorite wearable smart devices. It can inform their users of their current location, current time, the steps and the distance they have walked, the prospective weather situation, their physiology parameters, and etc. Normally, most of these data need to be synchronized with other smart

The associate editor coordinating the review of this manuscript and approving it for publication was Weiren Zhu<sup>ID</sup>.

devices, e.g. smartphones and personal computers, for deep analysis and long-term storage [3]. However, due to the size of the normal devices and the crowded arrangement of the inner components, antenna design is a challenge work in smartwatches, especially considering the strong coupling between the antenna and the human body. One of the popular antenna types for smartwatch was planar Inverted-F antenna (PIFA) [4]–[6], which was easy to cover a single band, usually the 2.4 GHz WLAN band, with a compact size. To realize multifunction, several modified multi-band PIFAs or monopole antennas were also proposed [7]–[12]. However, these structures could hardly be integrated with the framework of smartwatch and thus, were not suitable for the designs with totally metallic frame. Recently, the antennas integrated in the structures of smartwatches were proposed and studied, such as several antenna designs with metallic frame of smartwatches [13]–[17]. Although these designs

had some special advantages, none of them used diversity technology. Besides, some designs proposed the solutions of locating antennas and feeding ports on watch straps [18]–[20]. However, these designs were completely ingenious but not very practical due to the various deformations when worn on the user's wrist and also the unrealizable feeding connection between the antennas on the belt and the RF circuits in the body of the watches.

Antenna diversity technologies can significantly improve the performance of wireless communication systems in multi-reflection environments. Several scholars proposed dual-port antennas with polarization diversity and high port isolation [21]–[26]. However, due to their topologies and sizes, these designs could hardly be applied to real smartwatch and body scenarios. Most of these designs did not consider the integration between antenna and smartwatch, and the coupling between antenna and human tissue.

We propose a design of smartwatch integrated antenna with polarization diversity for 2.4 GHz WLAN applications. The proposed antenna has a simple structure because smart watch antenna is generally limited by its structure, and the proposed antenna compared to the existing antennas realizes diversity technology, which has not been realized in the previous smart watch antenna. The initial design idea is that two ports excite the odd and even modes of a ring resonator respectively, which has been presented in our previous work [27]. In this paper, the complete design and structure, operating mechanism, experimental and measured results, SAR results, ECC, and influence of battery and PCBA are fully analyzed which were not shown in [27], together with the measured results in free space and on the human body models (including cubic tissue model and wrist model). The final topology of the proposed antenna has a cylindrical shape. The diameter of the proposed antenna is 38 mm, and the height is 7.5 mm referring to the general height of the smart watch, which makes it easy to be integrated in the frame of normal smartwatch. The commercial simulation solver HFSS and CST are used in the design and calculation.

## II. CONFIGURATION AND STRUCTURE

In this chapter, the configurations of the simulation model in free space, with the cubic tissue model, and with wrist model are proposed.

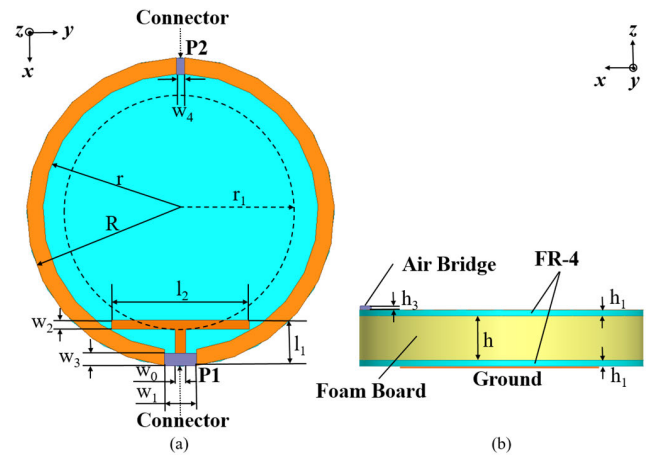
### A. ANTENNA DESIGN

Fig. 1 shows the geometry of the proposed antenna. The overall model has three layers. The top layer and the bottom layer are both FR-4 circuit boards ( $\epsilon_r = 4.3$ ,  $\tan \delta = 0.02$ ), and the antenna is located on the surface of the top FR-4 board. The middle layer is a foam board ( $\epsilon_r = 1.1$ ) which is used to pad the antenna up. All the values of the geometry parameters are shown in Fig. 1 and TABLE 1.

A split ring resonator plays the main body of the antenna [21], [27]. As shown in Fig. 1 (a), the antenna is composed of a T-shaped line and two metallic arcs. The T-shaped line for impedance matching is the extension of the inner signal

**TABLE 1. Geometry parameters of the proposed antenna.**

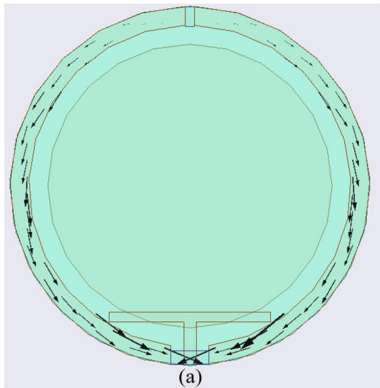
Geometry Parameter	Length (mm)	Geometry Parameter	Length (mm)
R	19	h	5.9
r	17	h <sub>1</sub>	0.8
r <sub>1</sub>	15	h <sub>3</sub>	0.5
w <sub>0</sub>	1.3	l <sub>1</sub>	5.6
w <sub>1</sub>	4	l <sub>2</sub>	17
w <sub>2</sub>	1.1	w <sub>3</sub>	1.5
w <sub>4</sub>	1		



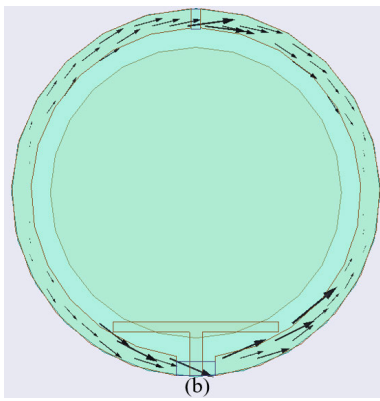
**FIGURE 1. Geometry of proposed antenna. (a)Top view. (b)Side view.**

line of the feeding CPW (port 1). The two metallic arcs are connected to the two outer ground planes of the CPW, and the electric length of one arc is about a half wavelength at 2.4 GHz. There is an air bridge wire across the port 1, which connects the two outer ground planes of the CPW together, shown in Fig. 1 (b), thus the annular ring is constructed. The annular ring connected to a CPS is excited by the port 2 at the other side of the antenna. A circular metallic shell is located under the bottom FR-4 board to mimic the backed shell of smartwatch, called 'Ground'. The design procedure: choosing appropriate values of 'h', 'R', 'r', 'r<sub>1</sub>' can realize impedance matching of port 2. Then, designing the geometry of T-shaped line can realize impedance matching of port 1.

Fig. 2 shows the simulated current distributions at 2.4 GHz. Port 1 is a CPW port. It is a common mode feed port which can excite the even mode. When port 1 is excited, the currents are distributed on the side metallic arcs with the current node at port 2 position, as shown in Fig. 2 (a), which will bring a low coupling between the two ports. Actually, the symmetric structure is the main reason for the good isolation. The current excited by port 1 is along the x- axis. Port 2 is a CPS port. It is a differential mode feed port which can excite the odd mode. When port 2 is excited, the currents are distributed on the side metallic arcs with the current node at the middle position of the metallic arcs, as shown in Fig. 2 (b). The current excited by port 2 is along the y- axis. Thus, the current on both the x- and the y- axis could be expected of this design from different feeding ports at 2.4 GHz, so the proposed antenna can realize orthometric radiation patterns in far field. Fig. 3 and Fig. 4 show the fabricated antenna



(a)



(b)

**FIGURE 2.** Simulated current distributions. (a) When P1 excited. (b) When P2 excited.

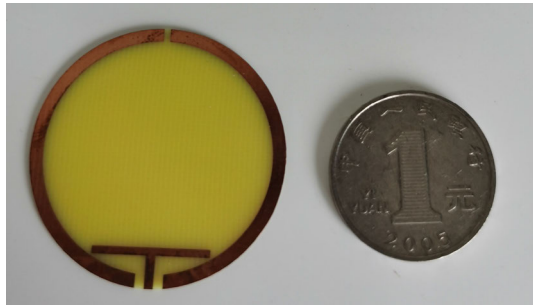


**FIGURE 3.** The fabricated antenna.

and the experimental environment in the microwave chamber for measurement. Two FR-4 boards are fabricated as printed circuits boards (PCB).

#### B. STRUCTURE WITH CUBIC TISSUE MODEL

Fig.5 shows the structure of the proposed antenna with the cubic tissue model. The cubic tissue model is constructed to three cuboid layers. They are skin, fat and muscle from top to bottom, respectively [28]. The thickness is 2 mm of skin, 5 mm of fat, and 20 mm of muscle. The length of the cuboid is 150 mm. These geometry parameters are to mimic the human body tissue. The parameters of each tissues are set from the material library in CST.

#### C. STRUCTURE WITH WRIST MODEL

Fig. 6 shows the structure of the proposed antenna with the wrist model. The wrist model is constructed to four cylindroid



**FIGURE 4.** The antenna in microwave chamber for measurement.

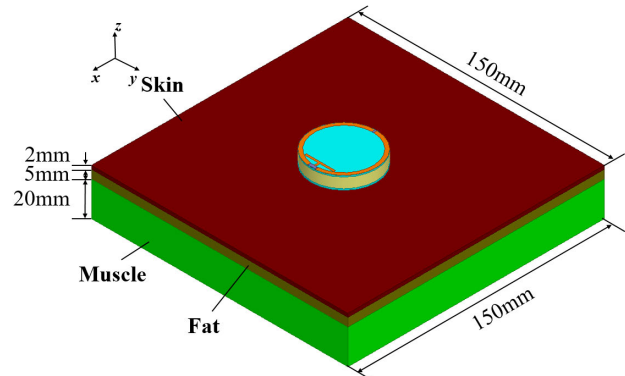


**FIGURE 5.** Geometry with the cubic tissue model.

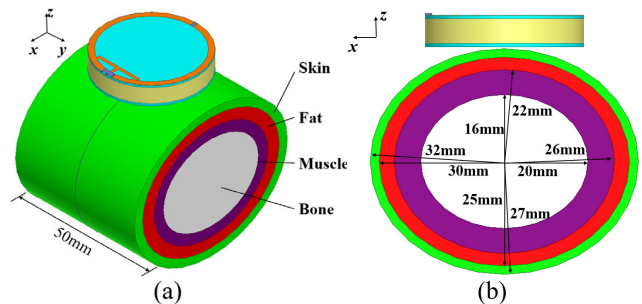


**FIGURE 6.** Geometry with the wrist model. (a) Full view. (b) Side view.

layers which are skin, fat, muscle and bone from its out to core [18]. The material parameters of the human tissue model are shown in TABLE 2 at 2.4 GHz. The distance between the ‘Ground’ and the human tissue model is written as ‘d’(mm).

### III. PERFORMANCES AND RESULTS

The proposed antenna is fabricated and measured. The results of simulation and measurement are analyzed in free space, and with the cubic tissue model and wrist model.

#### A. S PARAMETERS

The S parameters in free space are shown in Fig. 7 (a). In free space, port 1 operating band ( $S_{11} < -10$  dB, VSWL < 2) is from 1.89 GHz to 2.93 GHz in simulation, and from 1.89 GHz

**TABLE 2.** Material parameters of body model (2.4 GHz).

Human Tissue	$\epsilon_r$	$\sigma$ (S/m)	$\tan \delta$
Skin	38.06	1.44	0.28
Fat	5.29	0.11	0.15
Muscle	52.79	1.71	0.24
Bone	18.49	0.82	0.25

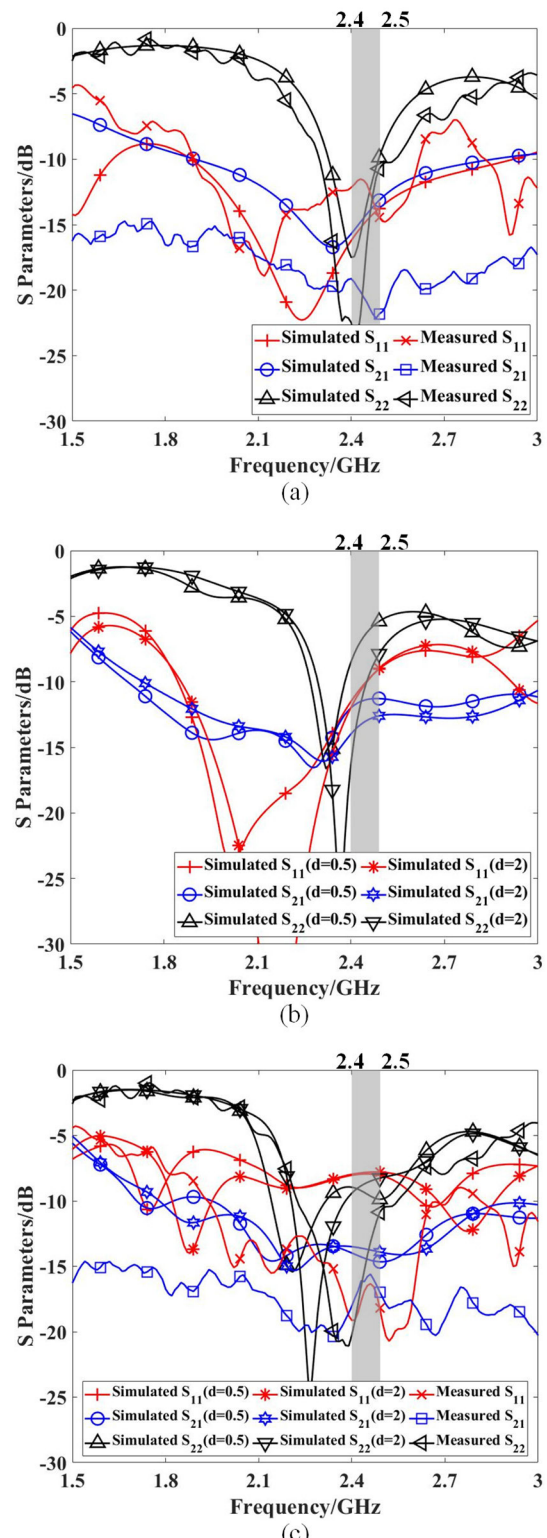
to 2.62 GHz in measurement. The overlapped bandwidth in free space is 1040 MHz in simulation, and 730 MHz in measurement, which can cover the band for 2.4 GHz WLAN applications. Port 2 operating band is from 2.33 GHz to 2.50 GHz in simulation, and from 2.31 GHz to 2.53 GHz in measurement. The overlapped bandwidth in free space is 170 MHz in simulation, and 220 MHz in measurement, which can also cover the band for 2.4 GHz WLAN applications. In the band range of 2.4 GHz – 2.5 GHz, the isolation between the two ports ( $S_{21}$ ) is lower than  $-13$  dB in free space.

Fig. 7 (b) shows the S parameters with the cubic tissue model when  $d$  is 0.5mm and 2mm. Fig. 7 (c) shows the S parameters with the wrist model when  $d$  is 0.5mm and 2mm, and especially the measurement results. The operating bands of both ports move to lower frequency because of the influence of human tissue, but they still cover 2.4 GHz WLAN bandwidth. The values of port isolation  $S_{21}$  is lower than  $-12$  dB on body scenario on the band range of 2.4 GHz to 2.5 GHz.

TABLE 3, TABLE 4 and TABLE 5 list all the values of operating band and bandwidth when antenna is in those three situations. When the antenna is put on the cubic model, its lowest bandwidth is 260 MHz when  $d$  is 0.5mm. When the antenna is put on the wrist model, the lowest bandwidth is 500 MHz when  $d$  is 2mm. These two lowest bandwidths are both sufficient for smartwatch antenna at 2.4 GHz WLAN. As for comparison between simulated results and measurement, there is little difference of the operating band between the simulation and measurement both in free space and on the wrist model, as shown in TABLE 3 and TABLE 5. The simulated results and measurements can cover the 2.4 GHz WLAN band. TABLE 6 shows that operating band is not much affected by the hand in measurement, because the ring is about 8 mm away from the hand, which reduces the impact.

## B. RADIATION PERFORMANCES

The simulated and measured radiation patterns of the proposed antenna in free space are shown in Fig. 8. The results are tested at 2.4 GHz. When one port is fed and tested, the other port is connected with a matched load. The radiation patterns between simulated results and measurement are close in Fig. 8. The results reveal that the realized gain of port 1 is 3.7 dBi in simulation and 3.2 dBi in measurement, while the realized gain of port 2 is 4.6 dBi in simulation and 4.7 dBi in measurement. It's close between the simulated and measured realized gain. Thus, the results of radiation pattern and realized gain between simulation and measurement are close. The cross-polarizations are below  $-10$  dB for both the



**FIGURE 7.** S parameters (a) in free space. (b) with cubic tissue model. (c) with wrist model.  $d$  (mm) is the distance between the antenna and the human tissue model. The same color represents the same S parameter: red is  $S_{11}$ ; blue is  $S_{21}$ ; black is  $S_{22}$ . The gray zone is the frequency band from 2.4 GHz to 2.5 GHz.

two ports. Furthermore, the radiations of the two ports have orthometric polarizations, which accords with the current

**TABLE 3.** Operating band ( $-10\text{dB}$ ) in free space.

Port	Operating Band (GHz)	Bandwidth (MHz)
Simulated Port 1	1.89 – 2.93	1040
Simulated Port 2	2.33 – 2.50	170
Measured Port 1	1.89 – 2.62	730
Measured Port 2	2.31 – 2.53	220

**TABLE 4.** Operating band ( $-6\text{dB}$ ) with cubic tissue model.

d	Port	Operating Band (GHz)	Bandwidth (MHz)
2mm	Simulated Port 1	1.68 – 2.62	940
	Simulated Port 2	2.24 – 2.54	300
0.5mm	Simulated Port 1	1.73 – 2.86	1130
	Simulated Port 2	2.22 – 2.48	260

**TABLE 5.** Operating band ( $-6\text{dB}$ ) with wrist model.

d	Port	Operating Band (GHz)	Bandwidth (MHz)
2mm	Simulated P1	1.72 – 3.22	1500
	Simulated P2	2.18 – 2.68	500
0.5mm	Simulated P1	1.92 – 3.15	1230
	Simulated P2	2.11 – 2.63	520
On Real Wrist	Measured P1	1.79 – 3.13	1340
	Measured P2	2.18 – 2.85	670

**TABLE 6.** Operating band ( $-10\text{dB}$ ) in measurement.

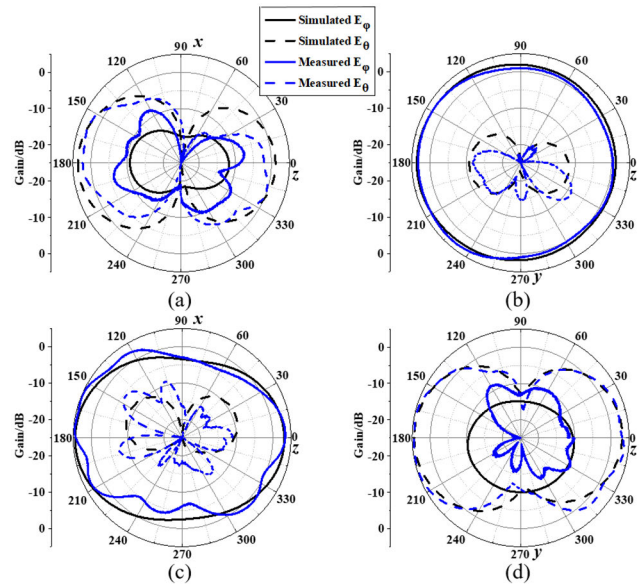
Environment	Port	$S_{ii}$ at 2.4 GHz	Operating Band (GHz)	Bandwidth (MHz)
Free Space	P1	-13 dB	1.89 – 2.62	730
	P2	-23 dB	2.31 – 2.53	220
Real Wrist	P1	-18 dB	1.96 – 2.65	690
	P2	-21 dB	2.25 – 2.51	260

distributions in Fig. 2. The values of measured radiation efficiency are higher than 80%, which is a bit lower than the simulated one, shown in TABLE 7. It is caused by processing loss and cable loss.

Fig. 9 shows the radiation patterns with the cubic tissue model and wrist model when  $d$  is 2 mm 0.5 mm at 2.4 GHz. The peak gain and efficiency of the same port with wrist model is higher than it with cubic tissue model when  $d$  is same. When  $d$  reduces from 2 mm to 0.5 mm, the gain and efficiency will be lower because the closer between antenna and human body, the more power human body absorbs. When the proposed antenna is on cubic tissue model, the values of peak gain and radiation efficiency are higher than 2.2 dBi and 32%, respectively, which are sufficient for smartwatch applications. When the antenna is put on wrist model, the values of peak gain and radiation efficiency are even higher than 4 dBi and 62%.

### C. SAR ANALYSES

The SAR is a value to represents the RF power-absorption rate by a unit mass of tissue within a unit time. The density ( $\rho$ ) of

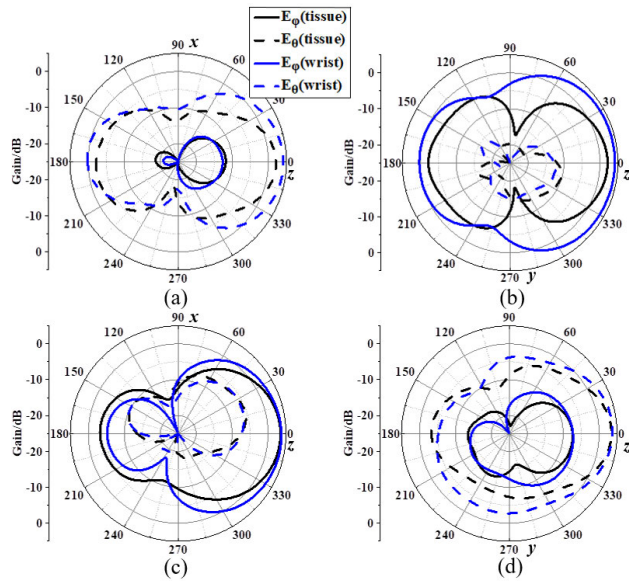
**FIGURE 8.** Radiation patterns in free space at 2.4 GHz. (a) xz-plane when P1 is excited; (b) yz-plane when P1 is excited; (c) xz-plane when P2 is excited; (d) yz-plane when P2 is excited.**TABLE 7.** Values of peak gain and radiation efficiency in free space and with human body model.

Environment	Situation	Peak Gain (dBi)		Radiation Efficiency	
		Port 1	Port 2	Port 1	Port 2
Free Space	Simulated	3.7	4.6	97%	98%
	Measured	3.2	4.7	88%	81%
Cubic Tissue Model	d=0.5	2.2	3.7	32%	44%
	d=2	3.9	4.9	52%	57%
Wrist Model	d=0.5	4.2	4.0	75%	62%
	d=2	4.7	4.9	77%	71%

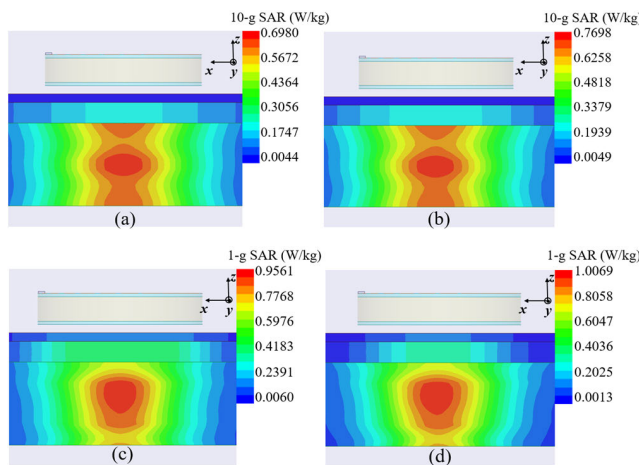
the human tissue is  $1000 \text{ kg/m}^3$ . According to the limitation that the maximum of equivalent isotropically radiated power (EIRP) is 20 dBm for 2.4 GHz band [29] and the peak gain which is more than 3 dBi of proposed antenna in foregoing results, we set the input power on both two ports of the proposed antenna to 17 dBm (50 mW). Measurement of SAR value is complicated. Our laboratory does not support it, but our fellows had a previous work to verify the accuracy and reliability of SAR value simulation [30]. Thus, we use simulation package HFSS and CST to calculate and analyze SAR results.

Fig. 10 shows the 10-g SAR and 1-g SAR distribution in xz-plane at 2.4 GHz with cubic tissue model when  $d$  is 2 mm. The peak SAR value appears in the center of the muscle layer in the cubic tissue model. The 10-g SAR peak value is about  $0.6980 \text{ W/kg}$  of port 1 and  $0.7698 \text{ W/kg}$  of port 2. The 1-g SAR peak value is about  $0.9561 \text{ W/kg}$  of port 1 and  $1.0569 \text{ W/kg}$  of port 2.

Fig. 11 shows the 10-g SAR and 1-g SAR distribution in xz-plane at 2.4 GHz with wrist model when  $d$  is 2 mm. The peak SAR value also appears in the center of the muscle layer



**FIGURE 9.** Radiation patterns on body scenarios at 2.4 GHz. (a) xz-plane when P1 is excited; (b) yz-plane when P1 is excited; (c) xz-plane when P2 is excited; (d) yz-plane when P2 is excited.



**FIGURE 10.** SAR distributions with cubic tissue model in HFSS when d is 2mm. (a)10-g SAR of port 1. (b)10-g SAR of port 2. (c) 1-g SAR of port 1. (d) 1-g SAR of port 2.

in the wrist model. The SAR values with cubic tissue model and wrist model when d is 0.5mm are also analyzed. All the specific values are shown in TABLE 7 and TABLE 8.

TABLE 8 lists SAR values with cubic tissue model and wrist model when d is 2 mm in both two software, and TABLE 9 lists SAR values when d is 0.5 mm. These two tables show the results calculated by HFSS and CST are similar. According to these two tables, when d reduces from 2 mm to 0.5 mm, the 10-g SAR value and 1-g SAR value will be higher, it is also because the closer between antenna and human body. The limitations about SAR values set by Federal Communication Commission (FCC) and European Telecommunication Standards Institute (ETSI) [31] are also listed in the two tables. According to the regulations, all the SAR values of proposed antenna are less than the corresponding SAR limitations set by both the FCC and ETSI. It means

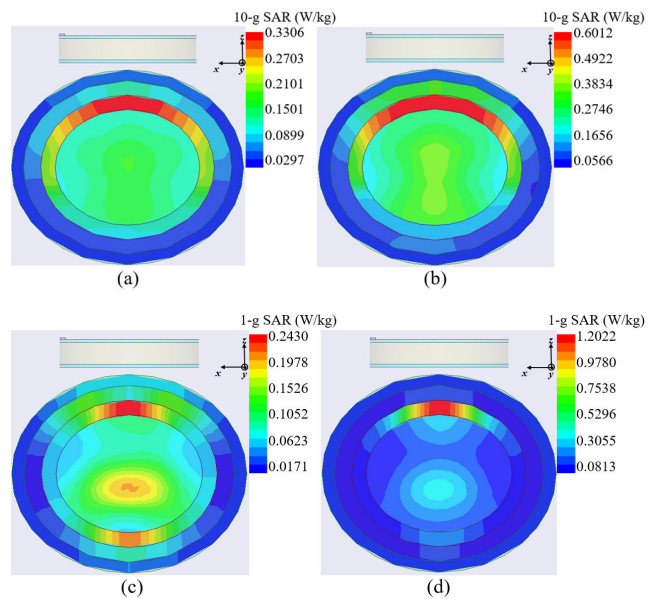


**FIGURE 11.** SAR distributions with wrist model in HFSS when d is 2mm. (a)10-g SAR of port 1. (b)10-g SAR of port 2. (c) 1-g SAR of port 1. (d) 1-g SAR of port 2.

**TABLE 8.** SAR values when d is 2 mm and limitations.

Limitations & Proposed Antenna Port	Simulation Software	10-g SAR (W/kg)	1-g SAR (W/kg)
FCC limitation	/	4.0	1.6
ETSI limitation	/	2.0	1.6
Port 1 with cubic model	HFSS	0.6980	0.9561
Port 2 with cubic model	HFSS	0.7698	1.0069
Port 1 with wrist model	HFSS	0.3306	0.2430
Port 2 with wrist model	HFSS	0.6012	1.2022
Port 1 with cubic model	CST	0.6254	0.5609
Port 2 with cubic model	CST	0.5692	0.7984
Port 1 with wrist model	CST	0.3191	0.3442
Port 2 with wrist model	CST	0.6607	1.2514

that the radiation effect on human body created by proposed antenna can be ignored. The proposed antenna will not make terrible effect on human health.

#### D. COMPARISON

TABLE 9 shows the comparison between the proposed antenna and other designs of smartwatch antennas in literatures. In size and structure, the planar dimension of the proposed antenna (diameter is  $0.3 \lambda$ ) is smaller than some of designs in references in TABLE 10. The height of proposed antenna (7.5 mm) refers to the size of the general smart watch, unlike antennas in [6], [8], [10], [11] whose heights were not suitable for a watch. In performance, the bandwidth, gain and radiation efficiency of the proposed antenna with hand

**TABLE 9.** SAR values when d is 0.5 mm and limitations.

Limitation & Proposed Antenna Port	Simulation Software	10-g SAR (W/kg)	1-g SAR (W/kg)
FCC limitation	/	4.0	1.6
ETSI limitation	/	2.0	1.6
Port 1 with cubic model	HFSS	0.8300	1.4850
Port 2 with cubic model	HFSS	0.5728	0.5837
Port 1 with wrist model	HFSS	0.2221	0.2922
Port 2 with wrist model	HFSS	0.4444	1.5867
Port 1 with cubic model	CST	0.7245	1.3942
Port 2 with cubic model	CST	0.4345	0.4104
Port 1 with wrist model	CST	0.2894	0.3547
Port 2 with wrist model	CST	0.4255	1.5393

**TABLE 10.** Comparison between proposed antenna and other smartwatch antennas in references. ' $\lambda'$  means the wavelength corresponding to the lowest operating frequency. ' $\varphi$ ' means diameter.

Ref.	Dimensions ( $\lambda^3$ )	Bandwidth at 2.4 GHz WLAN band on hand model (MHz)	Operating frequency (GHz)
[6]	0.29×0.25×0.004	Not given	2.4/3.5/5.2
[7]	0.21×0.21×0.028	Not given	1.57/1.94/2.4
[8]	0.25×0.25×0.008	160	2.4/5.2
[9]	0.30×0.21×0.03	Not given	1.57/1.8/2.4
[10]	0.4×0.27×0.009	Not given	2.4/5.2
[11]	0.27×0.27×0.003	Not given	2.4/3.5/5.0
[13]	0.35( $\varphi$ )×0.35×0.08	95	2.4
[15]	0.42×0.33×0.042	400	2.4
[16]	0.3×0.3×0.042	Not given	1.57/2.4/3.5
<b>proposed</b>	<b>0.3(<math>\varphi</math>)×0.3×0.058</b>	<b>500</b>	<b>2.4</b>

Ref.	Gain at 2.4 GHz on hand model (dBi)	Radiation efficiency on hand model	Polarization diversity
[6]	Not given	Not given	No
[7]	Not given	Not given	No
[8]	Not given	Not given	No
[9]	Not given	Not given	No
[10]	Not given	Not given	No
[11]	Not given	Not given	No
[13]	2.79	57%	No
[15]	-0.89	26%	No
[16]	Not given	Not given	No
<b>proposed</b>	<b>4.0</b>	<b>62%</b>	<b>Yes</b>

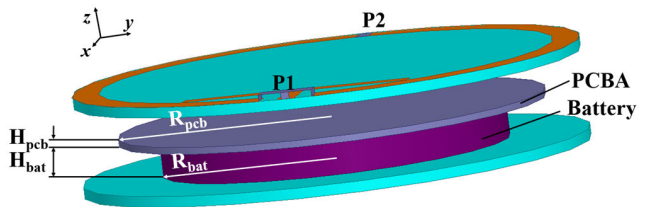
model are also the highest one, 500 MHz, 4.0 dBi and 62%, respectively. Most importantly, the proposed antenna is with polarization diversity which was not realized in the existing smart watch antenna, and it can be well integrated in the framework of smartwatch because of its annular shape.

#### IV. DISCUSSION

This chapter calculates the ECC to determine whether the proposed antenna can be used in MIMO applications, and adds the battery and PCBA into the inner structure to analyze the influence of them.

**TABLE 11.** ECC at 2.4 GHz.

Situation	$\rho_{12}$ by simulated S parameters	$\rho_{12}$ by measured S parameters	Measured $\rho_{12}$ in far field
Free Space	$1.126 \times 10^{-3}$	$7.794 \times 10^{-4}$	$1.109 \times 10^{-2}$
Cubic Tissue (d=2)	$3.519 \times 10^{-3}$	/	/
Cubic Tissue (d=0.5)	$1.368 \times 10^{-2}$	/	/
Wrist (d=2)	$1.252 \times 10^{-2}$	/	/
Wrist (d=0.5)	$1.162 \times 10^{-2}$	/	/
Real wrist	/	$3.738 \times 10^{-3}$	/

**FIGURE 12.** Antenna model after adding the battery and PCBA.**TABLE 12.** Gain and Efficiency with battery and PCBA at 2.4 GHz.  $R_{bat}$ ,  $R_{pcb}$ ,  $H_{bat}$  are in millimeters.  $H_{pcb} = 0.5\text{mm}$ .

$R_{bat}$	$R_{pcb}$	$H_{bat}$	Gain (P1)	Gain (P2)	Radiation efficiency (P1)	Radiation efficiency (P2)
13	16	2.5	3.2dBi	4.2dBi	95.6%	94.8%
<b>16</b>	16	2.5	3.1dBi	4.2dBi	95.5%	94.8%
13	<b>19</b>	2.5	3.0dBi	4.1dBi	90.4%	88.9%
13	16	<b>3.0</b>	3.2dBi	4.2dBi	95.6%	94.8%

#### A. ECC

ECC is a parameter to evaluate whether the antenna can be used in MIMO applications. It can be calculated by S parameters [32] or by this formula in far field [33]:

$$\rho_{12} = \frac{\left| \iint_{4\pi} \vec{F}_1(\theta, \varphi) * \vec{F}_2(\theta, \varphi) d\Omega \right|}{\sqrt{\iint_{4\pi} |\vec{F}_1(\theta, \varphi)| d\Omega \iint_{4\pi} |\vec{F}_2(\theta, \varphi)| d\Omega}} \quad (1)$$

The results of ECC at 2.4 GHz are shown in TABLE 11. It lists ECC calculated by simulated S parameters, measured S parameters, and measured ECC in far field. As we can see, the results are all low in free space. When antenna is with cubic tissue model or wrist model, the results of  $d = 0.5\text{ mm}$  and  $d = 2\text{ mm}$  are also low. The maximum value in TABLE 11 is just  $1.368 \times 10^{-2}$ , which is enough low to be used in MIMO applications.

#### B. INFLUENCE OF BATTERY AND PCBA

Influences of the battery and PCBA (printed circuit board assembly) are studied. We replaced the foam board with a PEC and a lossy metal to mimic battery and PCBA, shown in the Fig. 12. The S parameters in free space are shown in Fig. 13. When the PCBA is not too close to the proposed antenna, the antenna can basically maintain the impedance matching. When the battery and PCBA are too large, the antenna needs to be redesigned. Gain and Radiation efficiency are listed in TABLE 12, which are not too much affected.

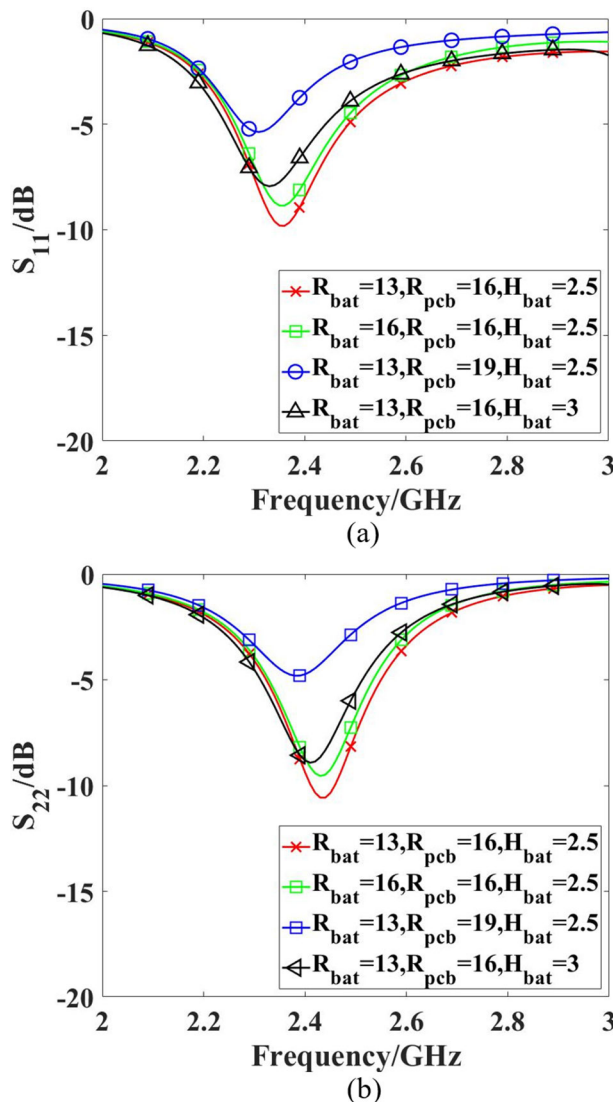


**FIGURE 13.** S parameters with battery and PCBA in free space. (a)  $S_{11}$ ; (b)  $S_{22}$ .  $H_{pcb}$  is 0.5mm.  $R_{bat}$ ,  $R_{pcb}$ ,  $H_{bat}$  are in millimeters.

## V. CONCLUSION

A design of smartwatch integrated antenna with polarization diversity is proposed. The annular shape and the size of the proposed antenna make it easy to be integrated in the frame of the normal smartwatch. The polarization diversity is realized by exciting the two ports. The antenna is also analyzed with cubic tissue model and wrist model when the d is 2 mm and 0.5 mm respectively. According to the simulation and measurement results, the band ranges can cover 2.4 GHz WLAN band. The peak gains are higher than 2 dBi of both ports in free space and on body scenarios. The port isolation  $S_{21}$  is lower than  $-13$  dB from 2.4 GHz to 2.5GHz, and the cross-polarization is below  $-10$  dB. The radiation efficiency is higher than 32% on cubic tissue model at 2.4 GHz, which is sufficient for smartwatch application, and it is even higher than 62% on wrist model. Besides, the 10-g SAR values and the 1-g SAR values calculated by HFSS and CST are analyzed, which are both less than the limitations set by

FCC and ETSI. When the distance between the proposed antenna and human body scenario get closer, the gain and radiation efficiency will get lower and the SAR value will get higher, but the performances are also acceptable. The low ECC results show the proposed antenna can be applied on MIMO applications. The influence of the battery and PCBA on the S parameter is large, but it is not much affected on gain and efficiency of the proposed antenna. The results prove the proposed design of smartwatch integrated antenna is a suitable candidate for smartwatches.

## REFERENCES

- [1] S. Yan, P. J. Soh, and G. A. E. Vandenbosch, "Compact all-textile dual-band antenna loaded with metamaterial-inspired structure," *IEEE Antennas Wireless Propag. Lett.*, vol. 14, pp. 1486–1489, 2015.
- [2] S. Yan, G. A. E. Vandenbosch, and P. J. Soh, "Wearable dual-band composite right/left-handed waveguide textile antenna for WLAN applications," *Electron. Lett.*, vol. 50, no. 6, pp. 424–426, Mar. 2014.
- [3] M. Haghi, R. Stoll, and K. Thurow, "Pervasive and personalized ambient parameters monitoring: A wearable, modular, and configurable watch," *IEEE Access*, vol. 7, pp. 20126–20133, 2019.
- [4] S. Kwak, D. Sim, J. H. Kwon, and Y. J. Yonn, "Design of PIFA with metamaterials for body-SAR reduction in wearable applications," *IEEE Trans. Electromagn. Compat.*, vol. 59, no. 1, pp. 297–300, Feb. 2017.
- [5] H. T. Chattha, Y. Huang, S. J. Boyes, and X. Zhu, "Polarization and pattern diversity-based dual-feed planar Inverted-F antenna," *IEEE Trans. Antennas Propag.*, vol. 60, no. 3, pp. 1532–1539, Mar. 2012.
- [6] A. J. Khalilabadi and A. Zadehgol, "An ultra-thin triple-band smartwatch antenna with support of several wireless application bands," in *Proc. IEEE Int. Symp. Antennas Propag. USNC-URSI Radio Sci. Meeting*, Atlanta, GA, USA, Jul. 2019, pp. 1281–1282.
- [7] C.-M. Cheng, W.-S. Chen, G.-Q. Lin, and H.-M. Chen, "Four antennas on smart watch for GPS/UMTS/WLAN MIMO application," in *Proc. IEEE Int. Conf. Comput. Electromagn. (ICCEM)*, Kumamoto, Japan, Mar. 2017, pp. 346–348.
- [8] Y. N. Jin and J. Choi, "Bandwidth enhanced compact dual-band smart watch antenna for WLAN 2.4/5.2GHz application," in *Proc. Int. Appl. Comput. Electromagn. Soc. Symp.*, Suzhou, China, 2017, pp. 1–2.
- [9] H.-S. Huang, H.-L. Su, and S.-L. Chen, "Multiband antennas for GPS/GSM1800/bluetooth/Wi-Fi smart watch applications," in *Proc. IEEE Int. Conf. Comput. Electromagn. (ICCEM)*, Kumamoto, Japan, Mar. 2017, pp. 352–354.
- [10] C.-Y. Chiu, S. Shen, and R. D. Murch, "Transparent dual-band antenna for smart watch applications," in *Proc. IEEE Int. Symp. Antennas Propag. USNC/URSI Nat. Radio Sci. Meeting*, San Diego, CA, USA, Jul. 2017, pp. 191–192.
- [11] H. Zou, Y. Li, M. Peng, M. Wang, and G. Yang, "Triple-band loop antenna for 5G/WLAN unbroken-metal-rimmed smartwatch," in *Proc. IEEE Int. Symp. Antennas Propag. USNC/URSI Nat. Radio Sci. Meeting*, Boston, MA, USA, Jul. 2018, pp. 463–464.
- [12] M. I. Ahmed and M. F. Ahmed, "Design of 5G smart watch with millimeter wave wearable antenna," in *Proc. 7th Int. Japan-Africa Conf. Electron., Commun., Comput. (JAC-ECC)*, Alexandria, Egypt, Dec. 2019, pp. 132–135.
- [13] D. Wu and S. W. Cheung, "A cavity-backed annular slot antenna with high efficiency for smartwatches with metallic housing," *IEEE Trans. Antennas Propag.*, vol. 65, no. 7, pp. 3756–3761, Jul. 2017.
- [14] C.-Y. Hong and S.-H. Yeh, "Cellular antenna design with metallic housing for wearable device," in *Proc. IEEE 5th Asia-Pacific Conf. Antennas Propag. (APCAP)*, Kaohsiung, Taiwan, Jul. 2016, pp. 419–420.
- [15] S.-W. Su and Y.-T. Hsieh, "Integrated metal-frame antenna for smartwatch wearable device," *IEEE Trans. Antennas Propag.*, vol. 63, no. 7, pp. 3301–3305, Jul. 2015.
- [16] W.-Z. Lee and W.-S. Chen, "An antenna design on metal frame of smart watch," in *Proc. Int. Workshop Electromagn., Appl. Student Innov. Competition (iWEM)*, Qingdao, China, Sep. 2019, pp. 1–2.
- [17] Y. Jia, L. Liu, J. Hu, and L.-J. Xu, "Miniaturized wearable watch antenna for wristband applications," in *IEEE MTT-S Int. Microw. Symp. Dig.*, Nanjing, China, May 2019, pp. 1–3.

- [18] G. Li, G. Gao, J. Bao, B. Yi, C. Song, and L.-A. Bian, "A watch strap antenna for the applications of wearable systems," *IEEE Access*, vol. 5, pp. 10332–10338, 2017.
- [19] K. Zhao, Z. N. Ying, and S. L. He, "Antenna designs of smart watch for cellular communications by using metal belt," in *Proc. 9th Eur. Conf. Antennas Propag.*, Lisbon, Portugal, 2015, pp. 1–5.
- [20] G. Li, G. Gao, W. Liu, J. Su, and Y. Bai, "An on-body watchband antenna for the applications of wearable systems," in *Proc. IEEE Int. Symp. Antennas Propag. USNC/URSI Nat. Radio Sci. Meeting*, San Diego, CA, USA, Jul. 2017, pp. 585–586.
- [21] W. W. Li, J. H. Zhou, B. Zhang, and B. Q. You, "High isolation dual-port MIMO antenna," *Electron. Lett.*, vol. 49, no. 15, pp. 919–921, Jul. 2013.
- [22] S. Yan, P. J. Soh, and G. A. E. Vandenbosch, "Dual-band textile MIMO antenna based on substrate-integrated waveguide (SIW) technology," *IEEE Trans. Antennas Propag.*, vol. 63, no. 11, pp. 4640–4647, Nov. 2015.
- [23] S. Yan and G. A. E. Vandenbosch, "Wearable Antennas with Tripolarization Diversity for WBAN Communications," *Elec. Lett.*, vol. 52, no. 7, pp. 500–502, 2016.
- [24] S. Yan and G. A. E. Vandenbosch, "Low-profile dual-band pattern diversity patch antenna based on composite Right/Left-handed transmission line," *IEEE Trans. Antennas Propag.*, vol. 65, no. 6, pp. 2808–2815, Jun. 2017.
- [25] J. Zhang, S. Yan, and G. A. E. Vandenbosch, "Realization of dual-band pattern diversity with a CRLH-TL-Inspired reconfigurable metamaterial," *IEEE Trans. Antennas Propag.*, vol. 66, no. 10, pp. 5130–5138, Oct. 2018.
- [26] C. B. Dietrich, K. Dietze, J. R. Nealy, and W. L. Stutzman, "Spatial, Polarization, and Pattern Diversity for Wireless Handheld Terminals," *IEEE Trans. Antennas Propag.*, vol. 49, no. 9, pp. 1271–1281, Sep. 2001.
- [27] B. Wang, A. Zhang, and S. Yan, "A dual-port annular antenna with polarization diversity for smartwatches," in *Proc. Cross Strait Quad-Regional Radio Sci. Wireless Technol. Conf. (CSQRWC)*, Taiyuan, China, Jul. 2019, pp. 1–3.
- [28] Y.-S. Chen and T.-Y. Ku, "A low-profile wearable antenna using a miniature high impedance surface for smartwatch applications," *IEEE Antennas Wireless Propag. Lett.*, vol. 15, pp. 1144–1147, 2016.
- [29] *Electromagnetic Compatibility and Radio Spectrum Matters (ERM); Wideband Transmission Systems; Data Transmission Equipment operating in the 2.4GHz ISM band and Using Wideband Modulation Techniques; Harmonized EN Covering the Essential Requirements of Article 3.2 of the R&TTE Directive*, document 300 328 V1.8.1, Jul. 2012.
- [30] P. J. Soh, G. Vandenbosch, F. H. Wee, A. van den Bosch, M. Martinez-Vazquez, and D. Schreurs, "Specific absorption rate (SAR) evaluation of textile antennas," *IEEE Antennas Propag. Mag.*, vol. 57, no. 2, pp. 229–240, Apr. 2015.
- [31] S. Yan and G. A. E. Vandenbosch, "Design of wideband button antenna based on characteristic mode theory," *IEEE Trans. Biomed. Circuits Syst.*, vol. 12, no. 6, pp. 1383–1391, Dec. 2018.
- [32] Y. Zheng, G. A. E. Vandenbosch, and S. Yan, "Low-profile broadband antenna with pattern diversity," *IEEE Antennas Wireless Propag. Lett.*, early access, May 21, 2020, doi: [10.1109/LAWP.2020.2996196](https://doi.org/10.1109/LAWP.2020.2996196).
- [33] S. Blanch, J. Romeu, and I. Corbella, "Exact representation of antenna system diversity performance from input parameter description," *Electron. Lett.*, vol. 39, no. 9, pp. 705–707, May 2003.



**BUYUN WANG** received the bachelor's degree in information and telecommunication engineering from Xi'an Jiaotong University (XJTU), Xi'an, China, in 2019, where he is currently pursuing the master's degree with the Faculty of Electronics and Information Engineering, Institute of Electromagnetics and Information Technology.

His current research interests include wearable antennas and antenna diversity.



**SEN YAN** (Member, IEEE) received the bachelor's and master's degrees in information and telecommunication engineering from Xi'an Jiaotong University (XJTU), Xi'an, China, in 2007 and 2010, respectively, and the Ph.D. degree in electrical engineering from Katholieke Universiteit Leuven (KU Leuven), Leuven, Belgium, in 2015. From 2015 to 2017, he was a Postdoctoral Researcher with KU Leuven. He joined EPFL, Lausanne, Switzerland, in 2016. He was a Visiting Researcher with The University of Texas at Austin, Austin, TX, USA. Since 2017, he has been a Full Professor with XJTU. He has authored or coauthored 43 international journal articles and 40 conference contributions. His current research interests include metamaterials, metasurfaces, wearable devices, textile antennas, reconfigurable antennas, antenna diversity, and nano-antennas. He was successful in achieving the Postdoctoral Fellowship from KU Leuven and FWO, in 2015 and 2016, respectively. He received the Young Talent Support Plan from XJTU, in 2017, and the Young Scientist Award of the International Union of Radio Science (URSI), in 2019.

• • •

Received April 15, 2019, accepted May 19, 2019, date of publication May 29, 2019, date of current version June 11, 2019.

Digital Object Identifier 10.1109/ACCESS.2019.2919745

# Energy-Efficient Photoplethysmogram Compression to Estimate Heart and Respiratory Rates Simultaneously

CHANKI PARK<sup>1</sup>, (Student Member, IEEE), AND BOREOM LEE<sup>2</sup>, (Member, IEEE)

<sup>1</sup>School of Mechanical Engineering, Gwangju Institute of Science and Technology (GIST), Gwangju 61005, South Korea

<sup>2</sup>Department of Biomedical Science and Engineering (BMSE), Institute of Integrated Technology (IIT), Gwangju Institute of Science and Technology (GIST), Gwangju 61005, South Korea

Corresponding author: Boreom Lee (leebr@gist.ac.kr)

This work was supported in part by the Basic Science Research Program through the National Research Foundation of Korea (NRF) funded by the Ministry of Science and ICT under Grant 2017R1A2B4009068, and in part by the GIST Research Institute (GRI) Grant funded by the Gwangju Institute of Science and Technology (GIST), in 2019.

**ABSTRACT** A photoplethysmogram (PPG) sensor has been broadly used for smart watches and bands because it is easy to measure and contains many health information, such as heart rate (HR) and respiratory rate (RR). Because the PPG sensor blinks an LED at sampling instants, the rate for sampling and LED flashing should be reduced to extend the battery life. To reduce the rate, we employed two different compressive covariance sensing (CCS) techniques and applied them to HR and RR estimation. The CCS cannot recover a signal itself but reconstructs its covariance. We designed a signal processing technique to extract HR and RR from the reconstructed covariance. The estimation performance was evaluated by using the open-source data and the experimental data, and the power consumption of a wrist-type PPG sensor with respect to the compression ratio was evaluated. The proposed method acquired the covariance of the PPG with an average sampling rate of 1.79 Hz below the Nyquist rate for HR (10 Hz), and it significantly reduced the energy consumption for the PPG sampling. Moreover, its estimation accuracy was sufficient to be used for a wearable healthcare system. As a result, the proposed method showed that HR and RR can be estimated with an ultra-low-power PPG sensor.

**INDEX TERMS** Compressed sensing, health information and management, energy efficiency, photoplethysmogram.

## I. INTRODUCTION

Heart rate (HR) and respiratory rate (RR) are important information because they reflect various physical status. The change of HR is caused by sympathetic and parasympathetic nervous systems, the basic level of body metabolism, venous return determined by peripheral circulation, physical activity, age, and the size of the body. RR depends on chemical factor (blood oxygen level), nervous factor, and voluntary control [1]. According to the fast-growing usage of smart watches and smart bands with a photoplethysmogram (PPG) sensor, the technique to monitor users' HR and RR in daily life has attracted great attention [2]–[4]. HR can be estimated from the PPG by using frequency analysis techniques such as the Fourier transform, power spectral density, and an adaptive

The associate editor coordinating the review of this manuscript and approving it for publication was Sabah Mohammed.

notch filter. Because the respiratory component of the PPG is not clearly observed in the PPG, various signal processing techniques have been developed to estimate RR from the PPG.

There are three types of modulation of the PPG induced by respiration: amplitude, baseline, and pulse width modulations. Among these modulations, the baseline modulation can be understood as the presence of a frequency component; the frequency corresponds to RR. To extract the frequency component, digital filters were used [5]. For example, the respiratory component of PPG was acquired using a 0.6 Hz low-pass filter (LPF). An autoregressive (AR) model was frequently used for RR estimation [6], [7]. The poles of the AR model represent frequencies of the input signal and these are computed through a batch processing method. The concept was simple and the estimate was accurate. To implement a real-time operation, the AR model method

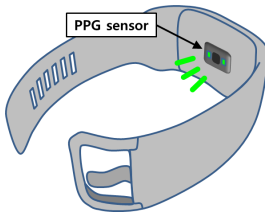


**FIGURE 1.** A smart band with a PPG sensor.

employed a moving-window technique yielding computational redundancy. In our previous study, we suggested an adaptive lattice-type respiratory rate estimator (ALRE) which utilizes an adaptive lattice notch filter (ALNF) as a frequency estimator [8]. The relation between designing a notch filter and finding AR model coefficients is theoretically similar and the ALRE can be interpreted as an adaptive version of the AR model method. As a result, it showed superior performance as well as has an efficient computational structure. Recently, the Holo-Hilbert spectral analysis based approach was proposed [9]. It can capture both frequency-modulated and amplitude-modulated features. However, it demands significant computational resources caused by an empirical mode decomposition (EMD). So far, many RR estimation algorithms have been developed using frequency analysis of PPG.

In spite of the development of smart watches, it is still important to extend battery life; the energy consumption of a PPG sensor determines the battery life. The PPG sensor illuminates the user's skin using a light-emitted diode (LED) and measures the change of blood volume by using the reflected light (see Fig. 1). Because the sensor should blink the LED at sampling instants to acquire a PPG, the rate for sampling and LED flashing is directly related to the energy consumption. A high rate will significantly reduce the battery life of smart watches or bands. To monitor the user's HR and RR for an extremely long time, an energy-efficient PPG sampling technique is required.

Compressed sensing (CS) is a representative technique that can analyze an original signal using a compressed signal sampled at a lower sampling rate than the Nyquist rate [10]. In previous studies, CS showed that electrophysiological signals (e.g., electromyogram and electrocardiogram) could be compressed with higher energy efficiency than wavelet-based compression techniques [11], [12]. Even though CS can compress a given analog signal through a measurement matrix, it cannot reduce the rate of LED pulses, for smart watches, because the light emission is essential to obtain the analog PPG [13].

As an alternative approach to CS, a new technique called compressive covariance sensing (CCS) has been proposed [14]. In the compression phase of CCS, the original signal is sampled with a specific pattern defined by a sparse ruler. Because no additional procedure is required for the compression (or sampling) phase of CCS, CCS can reduce

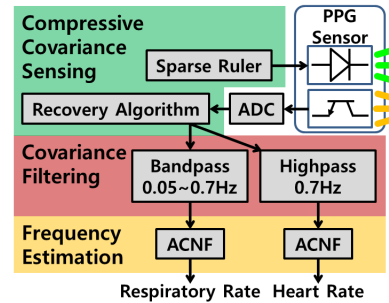


**FIGURE 2.** Block diagram representation of the proposed method.

the rate of sampling and LED flashing. Hence, we exploited the CCS to enhance the energy-efficiency of the PPG sensor. Daniel Romero and Greet Leus proposed the original CCS, which restores the covariance matrix of a non-sparse signal using a least square method [15]. We call it LS-CCS for convenience. Recently, we proposed an online CCS. Both the compression and recovery procedures of the online CCS are online processing [21]. It achieves a higher compression ratio than LS-CCS by using a circular sparse ruler (CSR). In this study, we considered only a covariance vector instead of the covariance matrix. Both CCS methods are described in section II in detail.

The CCS technique recovers the second-order statistics of an original signal from the compressed signal, but it cannot recover the original signal itself. Because covariance contains the frequency information of the original signal, CCS can be used to estimate HR and RR from a PPG. However, because the average sampling rate of CCS does not satisfy the Nyquist condition and the compressed signal is not equi-spaced data, conventional discrete-time signal processing techniques are unsuitable. Hence, we proposed an energy-efficient PPG sampling technique using CCS and designed new signal processing algorithms for CCS. The methods are explained in detail in the next section. In the results section, we compare the LS-CCS, online CCS, and ALRE using open-source data and wrist-type PPG signals. In the discussion section, the experimental results are interpreted and discussed.

## II. METHODS

The proposed PPG sampling technique consists of three steps as shown in Fig. 2. In the first step, the PPG makes the LED blink with the pattern of a sparse ruler, and then measures the reflected light; the sparse ruler determines the rate of LED pulses. From the measured samples (see Fig. 3), it reconstructs a covariance of PPG using a recovery algorithm. These processes correspond to the compression and recovery phases of CCS. We adopted two different CCSs (LS-CCS or online CCS) and these are explained in the next subsections. In the second step, cardiac and respiratory components are extracted from the reconstructed covariance, and then HR and RR are estimated using a frequency estimator.

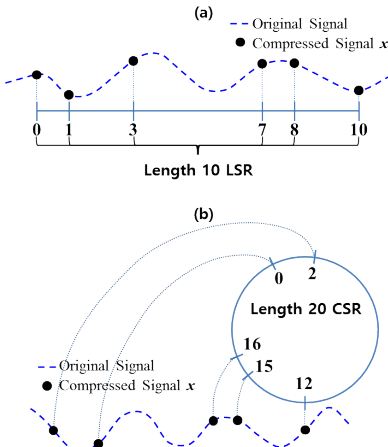


**FIGURE 3.** Sampling pattern and sparse rulers. (a) A length-10 LSR. (b) A length-20 CSR.

For computational efficiency, we designed an adaptive covariance notch filter (ACNF) to estimate the frequencies (HR and RR).

#### A. COMPRESSIVE COVARIANCE SENSING

CCS consists of a compression phase and a recovery phase. In the compression phase, CCS employs a sparse ruler as a sampling pattern. There are two kinds of sparse rulers (see Fig. 3): a linear sparse ruler (LSR) and a circular sparse ruler (CSR). A length- $(N - 1)$  sparse ruler has  $M$  marks, which are integers between 0 and  $N - 1$  ( $M \ll N$ ), and a set of the marks is  $S \subset \{0, \dots, N - 1\}$ .  $S$  is a length- $(N - 1)$  LSR when there exists at least one pair of elements  $s$  and  $s'$  in  $S$  for all integers  $l$  between 0 and  $N - 1$  such that

$$s - s' = l \quad (1)$$

where  $s \geq s'$ . In the same manner,  $S$  is a length- $(N - 1)$  CSR, if for any integer  $l$  from 0 to  $N - 1$  there is one or more pairs  $s$  and  $s'$  in  $S$  such that

$$(s - s') \% N = l \quad (2)$$

where  $\%$  is a modulo operator. The compression ratio is  $M/N$ . When a sparse ruler  $S$  has the least number of marks, then  $S$  has an optimal compression ratio and is called a minimal sparse ruler. By the concatenation of the same  $B$  sparse rulers, a length- $(L - 1)$  sparse ruler is implemented ( $L = B \times N$ ), and the number of marks  $K$  is  $B \times M$ . The  $L$  will be the length of the estimated covariance.

The compression phase is an underdetermined system, but it can be transformed into an overdetermined system by assuming that the covariance matrix has a specific structure such as Toeplitz and circulant. The original CCS solves the transformed overdetermined model using a least-square method; we call it LS-CCS. The original LS-CCS employed an LSR in the compression phase. The full procedure of LS-CCS is described in [14] in detail.

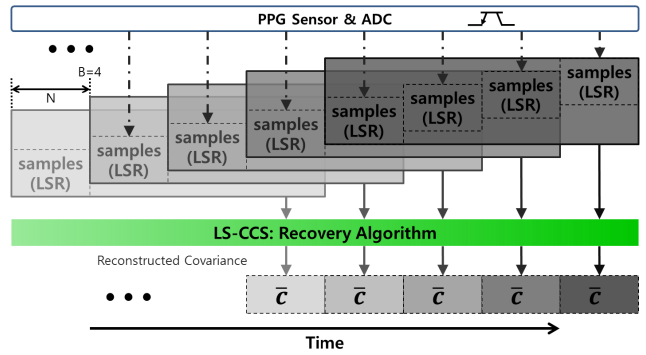


**FIGURE 4.** Real-time implementation of LS-CCS.

The LS-CCS assumes the original signal is wide-sense stationarity (WSS) and the estimated covariance is calculated over a length- $(L - 1)$  LSR; its temporal resolution is insufficient. To implement real-time estimation, we employ a moving window technique as shown in Fig 4. The length  $L$  covariance is calculated from recent  $B$  LSRs, and the estimate is updated at the end of each LSR. Because there is an overlap of  $(B - 1) \times N$  samples at each time window, this real-time implementation has computational redundancy.

#### B. ONLINE COMPRESSIVE COVARIANCE SENSING

In our previous study, we proposed an online CCS [21]. It has several advantages over the LS-CCS. First, it utilized a CSR having a higher compressibility than a length  $(N - 1)$  LSR, generally [16]. Second, its temporal resolution is better than that of LS-CCS, because the online CCS updates the estimate at every mark. Last, because the recovery algorithm of the online CCS is operated by a recursive formulation, there is no computational redundancy, unlike the real-time implementation of LSR.

In the compression phase, the online CCS samples the signal with the pattern of a CSR (see Fig. 3). Pairs of the new sample values and the corresponding mark indices are stored in a two-dimensional queue  $D = [\mathbf{x}, \mathbf{i}]$ .  $\mathbf{x}$  consists of sample values and  $\mathbf{i}$  represents their marks. After sampling and enqueueing, the covariance recovery algorithm is immediately operated using the updated queue  $D$ . The recovery algorithm is described in Algorithm 1.

#### C. COVARIANCE FILTERING

Because the feasible ranges of RR are HR are different, a digital filtering technique can extract cardiac and respiratory components. However, most discrete-time signal processing techniques are not applicable to CCS, because not only does the CCS not satisfy the Nyquist condition but also the samples are not uniformly spaced. To solve this problem, we exploit the relation between the covariance of the filtered signal  $\mathbf{y}$  and input signal  $\mathbf{x}$  [17] as follows:

$$\mathbf{y}[n] = h[n] * \mathbf{x}[n] \quad (3)$$

$$c_y[l] = c_x[l] * h[l] * h^*[-l] \quad (4)$$

**Algorithm 1** Covariance Recovery of Online CCS

---

**Input:** samples at iteration  $m \mathbf{x} = [x(1), \dots, x(K)]^T$ ,  
sample marks  $\mathbf{i} = [i(1), \dots, i(K)]^T$ ,  
and recovered covariance sequence at iteration  $m - 1$   
 $\bar{\mathbf{c}}(m-1) = [\bar{c}(0, m-1), \dots, \bar{c}(L-1, m-1)]^T$

**Output:** recovered covariance sequence at iteration  $m$   
 $\bar{\mathbf{c}}(m) = [\bar{c}(0, m), \dots, \bar{c}(L-1, m)]^T$

---

$\bar{\mathbf{c}}(m) = \bar{\mathbf{c}}(m-1)$   
**for**  $j = 0 : B - 1$   
    **for**  $k = 1 : M$   
         $l = (i(k + Mj) - i(1)) \% N + Nj$   
         $\bar{c}(l, m) = \lambda \bar{c}(l, m) + (1 - \lambda)x(1) \cdot x^*(k + Mj)$   
    **end**  
**end**  
\* %: modulo operator

---

where  $h[n]$  represents the impulse response of the digital filter.  $c_y$  and  $c_x$  are the covariances of the filtered signal  $y$  and the input signal  $x$ . As shown in (4), the covariance of the filtered signal can be calculated by forward-backward filtering of the reconstructed covariance [18]. In this study, a Butterworth filter was employed to enhance the HR and RR. A 0.7 Hz high pass filter and a 0.05–0.7 Hz bandpass filter were used for HR and RR estimation, respectively.

**D. FREQUENCY ESTIMATION**

Because the covariance contains the frequency information of the original signal, the HR and RR can be estimated by using a Fourier transform; the Fourier transform of covariance is the power spectral density. Maximum values of the spectrum will correspond to HR and RR, but it is inefficient to operate these processes at each iteration. Hence, we designed an adaptive covariance notch filter (ACNF) which serves as a frequency estimator. The ACNF is based on a 2<sup>nd</sup> order infinite impulse response (IIR) notch filter as follows:

$$H(z) = \frac{1 - 2az^{-1} + z^{-2}}{1 - (1+r)az^{-1} + rz^{-2}} \quad (5)$$

$$a = \cos(\omega_0) \quad (6)$$

where  $\omega_0$  represents notch frequency.  $a$  and  $r$  are the coefficients of the all-zero filter, and the pole-and-zero contraction factor ( $0 \leq r < 1$ ), respectively. The notch filter (5) can be expressed as difference equations as follows:

$$s[l] = c_y[l] + (1+r)as[l-1] - rs[l-2] \quad (7-1)$$

$$e[l] = s[l] - 2as[l-1] + s[l-2] \quad (7-2)$$

where  $s[l]$  is the output of the all-pole filter, and  $e[l]$  is the output of the notch filter. We set the cost function as follows:

$$J[l] \equiv E[e^2[l]] \quad (8)$$

where  $E[\cdot]$  means ensemble average. By optimization of the cost function  $J[l]$  with respect to  $a$ , we can find the optimal  $a$  as follows:

$$\frac{\partial J[l]}{\partial a} = E[-2e[l]s[l-1]] = 0 \quad (9)$$

$$a[l] = \frac{E[\{s[l] + s[l-2]\}s[l-1]]}{2E[s^2[l-1]]} \quad (10)$$

To compute  $a[l]$ , we replace the ensemble average with a sample mean. The estimated frequency is calculated as follows:

$$\hat{\omega}_0[l] = \cos^{-1}(a[l]) \quad (11)$$

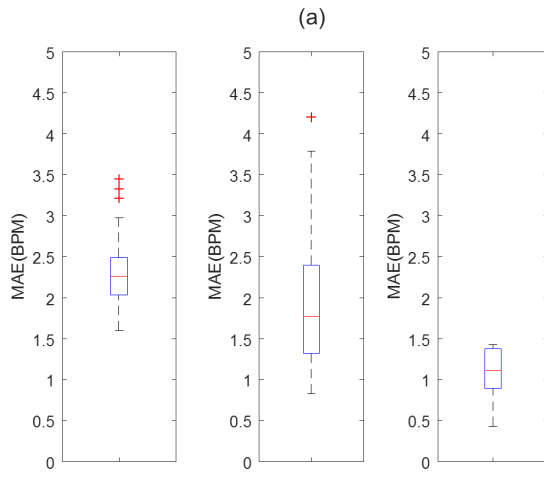
The input of the ACNF is the filtered covariance and its estimate corresponds to HR or RR (see Fig. 2). The ACNF can be interpreted as the batch version of ALNF [19].

**E. DATA COLLECTION**

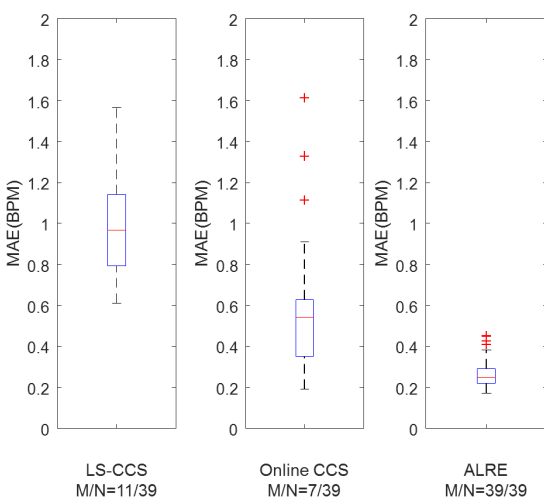
We used an MIT MIMIC Database and isolated 50 data sets which were less contaminated by artifacts [20]. Each data set was recorded at a sampling rate of 125 Hz for 9 min 40 s. It included the PPG, ECG, and respiratory signal. Because the feasible range of HR is 0.5–5 Hz, we down-sampled the signals to 10.4167 Hz. Additionally, we collected wrist-type PPG, ECG, and respiratory signals from four male and one female subjects (Age = 27 ± 2.6 years). All subjects were instructed to take a breath randomly and participated in six trials. In total, 30 data sets were collected. We utilized a SON1303 sensor as the wrist-type PPG sensor and the signal was sampled by an Atmel ATmega 328 with a sampling rate of 10 Hz. To implement energy-efficient sampling, we adjusted the intensity of the LED of the sensor as low as possible and set it to blink with a pulse width of 25 ms. The ECG and respiratory signal were measured by a BIOPAC® and its sampling frequency was 1000 Hz. All signals were recorded for 5 min and were synchronized. The peaks of the ECG were used to acquire the reference HR, and the reference RR was calculated from the zero crossing values of the respiratory signal. To evaluate energy consumption, we connected a 10.1 Ω resistor between a power source and the wrist-type PPG system and acquired the current by measuring the voltage across the resistor [11]. The LED flashing and sampling pattern, with a sparse ruler, were implemented on the Atmel ATmega328. The institutional review board of the Gwangju Institute of Science and Technology approved all procedures in this study.

**III. RESULTS**

We proposed an energy-efficient HR and RR estimation method using CCS and evaluated each result for two different types of CCS (LS-CCS and online CCS). The HR and RR estimation performance of the proposed method was compared with that of ALRE. Because there is no compression for ALRE, the compression ratio ( $M/N$ ) of ALRE is 1. We used a length-38 LSR ( $M/N = 11/39$ ) for LS-CCS and a length-38 CSR ( $M/N = 7/39$ ) for the online CCS. Both sparse rulers are minimal sparse rulers. To obtain sufficient covariance length, we set  $B = 5$ . Because convergence time is required for the frequency estimation, we excluded the initial 25 sec from our analysis. The performance of the method was evaluated through the mean absolute error (MAE) between estimated RR and reference RR, and between the estimated



(a)

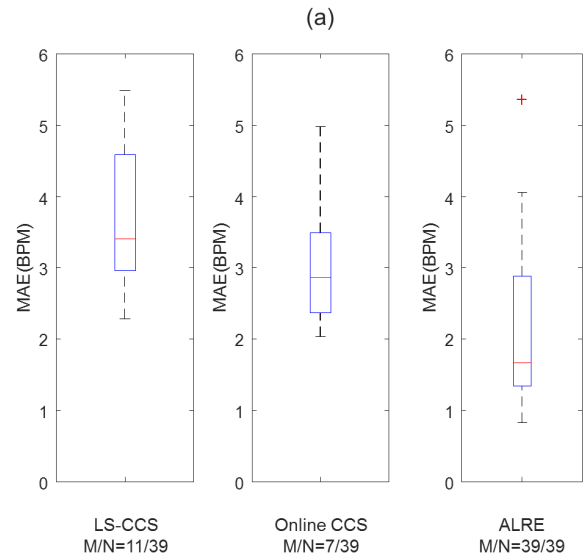


(b)

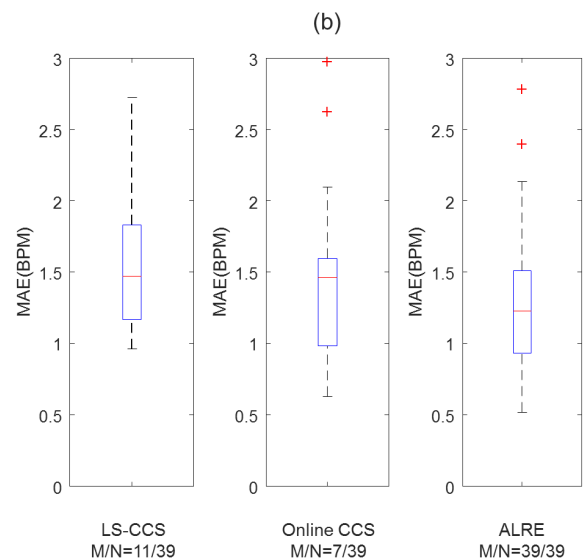
**FIGURE 5.** Distribution of MAE of HR and RR estimation for MIT MIMIC open source data. HR and RR are estimated by each method (LS-CCS, Online CCS, and ALRE). Upper and lower boxes represent the distribution of MAEs from 25th to 75th percentiles. Top and bottom lines indicate the 90th and 10th percentiles. (a) and (b) depict the results for HR and RR, respectively.

HR and reference HR. For a fair comparison, we adopted the parameters of each method, which minimized the MAE.

First, we evaluated the HR and RR estimation performance using the Massachusetts Institute of Technology (MIT) multiparameter intelligent monitoring in intensive care (MIMIC) data. As shown in Fig. 5, the HR and RR estimates of the ALRE ( $M/N = 1$ ) showed best estimation accuracy; however, its compression ratio  $M/N = 1$ . Although the proposed approach does not have better performance than ALRE, the compression ratio of LS-CCS is  $M/N = 11/39$  and that of online CCS is  $7/39$ . It was shown that the online CCS leads to better estimation performance than the LS-CCS. We performed statistical tests by using a paired t-test between the estimate of online CCS and that of other methods (the LS-CCS based method and ALRE). There was a significant



(a)



(b)

**FIGURE 6.** Distribution of MAE of HR and RR estimation for our experimental data. HR and RR are estimated by each method (LS-CCS, Online CCS, and ALRE). Upper and lower boxes represent the distribution of MAEs from 25th to 75th percentiles. Top and bottom lines indicate the 90th and 10th percentiles. (a) and (b) depict the results for HR and RR, respectively.

difference between the HR estimate of online CCS and that of LS-CCS ( $p < 0.05$ ), and there was an extremely significant difference between the HR estimate of online CCS and that of ALRE ( $p < 0.005$ ). In the case of RR estimation, all p-values were less than 0.005 for all comparisons (online CCS vs. LS-CCS and ALRE vs. online CCS). In our experimental data, the estimation performance of all methods shows the similar tendency as the result for the MIT MIMIC data (see Fig. 6). We performed statistical tests on our experimental data with the non-parametric Wilcoxon's two-sample signed-rank test between the estimate of online CCS and that of other methods. In the case of HR estimation, all p-values were less than 0.005 for all comparisons (online CCS vs. LS-CCS and ALRE vs. online CCS). There was an extremely significant

**TABLE 1.** The energy consumption necessary for flashing an led and sampling an analog Ppg.

Compression Ratio ( $M/N$ )	7/39	11/39	39/39
Energy Consumption (mW)	1.8	2.0	3.1

difference between the RR estimate of online CCS and that of ALRE ( $p < 0.005$ ), but there was no significant difference between the RR estimate of online CCS and that of LS-CCS.

We evaluated the energy consumption of each method for LED flashing and sampling. The average sampling rates of ALRE, LS-CCS, and online CCS were 10 Hz, 2.82 Hz, and 1.79 Hz, respectively. Table 1 shows the energy consumption for flashing an LED and sampling an analog PPG. A compression ratio of 39/39 denotes no compression.

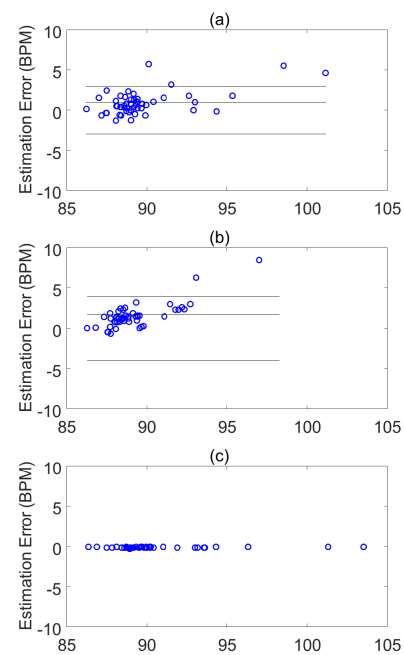
#### IV. DISCUSSION

HR and RR are the most crucial items of health information. It is difficult to estimate RR from a PPG because the respiratory component is not clearly observed in the PPG. Advanced signal processing techniques, such as digital filters [5], AR models [6], and adaptive filters [8], have been used to estimate RR. We proposed an energy-efficient PPG covariance sampling technique using CCS and designed an algorithm to estimate the HR and RR from the reconstructed covariance of PPG.

Because PPG is obtained by measuring the reflected light from the skin, the LED should flash at the timing for sampling. It is very important to reduce the rate for LED flashing and sampling to enhance the energy-efficiency of a PPG sensor. Conventional CS cannot reduce the number of LED flashes, but CCS can reduce the rate.

Daniel Romero and Greet Leus first proposed CCS using a least square method [15]. LS-CCS is an innovative sampling technique, but LS-CCS has several limitations. First, the temporal resolution is not good, because it is a batch process. Second, its huge dimensionality can lead an insufficient memory condition. Last, it was designed using an LSR. A CSR, generally, has a better compression ratio than an LSR. In order to compensate for the temporal resolution of LS-CCS, we designed a scheme for real-time implementation (see Fig. 4). The recently proposed online CCS not only compresses the signal through a CSR but also performs the covariance recovery with online processing [21]. Therefore, the online CCS has better compression and temporal resolution than LS-CCS. Although the real-time implementation scheme for LS-CCS causes computational redundancy, the online CCS does not have such redundancy and has lower computational complexity than LS-CCS.

Because the signal obtained by CCS is not equi-spaced data, conventional signal processing techniques cannot be applied; therefore, covariance filtering is proposed instead of digital filtering. Covariance filtering can be implemented by forward-backward filtering [18]. Although HR and RR can be estimated by analyzing the frequency of the reconstructed covariance, frequency analysis such as using the

**FIGURE 7.** Bland Altman plot for HR estimation (MIT-MIMIC data). (a) Online CCS; (b) LS-CCS; (c) ALRE.

Fourier transform is inefficient to trace HR and RR. The proposed ACNF can recursively track HR and RR with a light computation load. The ACNF can be interpreted as a batch version of ALNF [19].

Generally, the compressibility of compression methods (e.g., wavelet transform and compressed sensing) is inversely proportional to their performance. In the case of CCS, the number of marks of a sparse ruler determines the compression ratio of CCS. In this study, we used a minimal sparse ruler, which has the least number of marks. Even though the number of marks increases, all elements of the covariance are not uniformly restored, but only some elements are repeatedly reconstructed. Hence, there was no significant difference in estimation performance between sparse rulers with the same length and different compression ratios.

Unlike conventional compression techniques, CCS compresses a signal according to a sparse ruler without any criterion. This feature can implement an energy-efficient PPG compression system but results in loss of informative data and poor estimation accuracy. Hence, the estimate of CCS was shown to be less accurate than that of ALRE (see Fig. 7). Even though the estimation performance of online CCS is lower than that of ALRE, most of the estimation errors were less than 5% and it is sufficiently useful in healthcare applications [21]. We expect that advanced signal processing techniques will enhance the estimation accuracy of online CCS.

HR and RR estimation performance was evaluated using the MIT-MIMIC open source database and our experimental data. The estimation accuracy of ALRE was the best. The online CCS not only has better compression ratio than the LS-CCS but also showed good HR and RR estimation

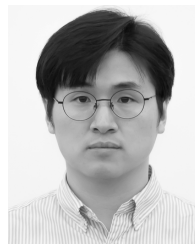
performance. The online CCS showed the highest efficiency in terms of energy consumption (see Table 1). The online CCS acquires the covariance of PPG with an average sampling rate of 1.79 Hz, below Nyquist rate for HR (10 Hz).

## V. CONCLUSION

We proposed an energy-efficient PPG compression technique and applied it to HR and RR estimation. The HR and RR estimation method based on the online CCS reduced the sampling and LED flash rate by 1.79 Hz and showed a high estimation accuracy. We expect that this energy-efficient PPG compression technique will be widely used for a smart watch and band. In future work, we will develop an advanced signal processing technique to enhance the estimation accuracy of the CCS technique.

## REFERENCES

- [1] A. Guyton and J. Hall, *Textbook of Medical Physiology*, 9th ed. Philadelphia, PA, USA: Elsevier Saunders, 1996.
- [2] T. Tamura, Y. Maeda, M. Sekine, and M. Yoshida, "Wearable photoplethysmographic sensors—Past and present," *Electronics*, vol. 3, no. 2, pp. 282–302, Apr. 2014.
- [3] Z. Zhang, Z. Pi, and B. Liu, "TROIKA: A general framework for heart rate monitoring using wrist-type photoplethysmographic signals during intensive physical exercise," *IEEE Trans. Biomed. Eng.*, vol. 62, no. 2, pp. 522–531, Feb. 2015.
- [4] P. Renevey, R. Delgado-Gonzalo, A. Lemkadem, C. Verjus, S. Combertaldi, B. Rasch, B. Leeners, F. Dammeier, and F. Kübler, "Respiratory and cardiac monitoring at night using a wrist wearable optical system," in *Proc. IEEE 40th Annu. Int. Conf. Eng. Med. Biol. Soc. (EMBC)*, Jul. 2018, pp. 2861–2864.
- [5] K. Nakajima, T. Tamura, and H. Miike, "Monitoring of heart and respiratory rates by photoplethysmography using a digital filtering technique," *Med. Eng. Phys.*, vol. 18, pp. 365–372, Jul. 1996.
- [6] S. G. Fleming and L. Tarassenko, "A comparison of signal processing techniques for the extraction of breathing rate from the photoplethysmogram," *Int. J. Biol. Med. Sci.*, vol. 2, no. 4, pp. 232–236, 2007.
- [7] J. Lee and K. H. Chon, "Respiratory rate extraction via an autoregressive model using the optimal parameter search criterion," *Ann. Biomed. Eng.*, vol. 38, no. 10, pp. 3218–3225, Oct. 2010.
- [8] C. Park and B. Lee, "Real-time estimation of respiratory rate from a photoplethysmogram using an adaptive lattice notch filter," *Biomed. Eng. Online*, vol. 13, no. 1, p. 170, Jan. 2014.
- [9] H.-H. Chang, C.-C. Hsu, C.-Y. Chen, W.-K. Lee, H.-T. Hsu, K.-K. Shyu, J.-R. Yeh, P.-J. Lin, and P.-L. Lee, "A method for respiration rate detection in wrist PPG signal using Holo-Hilbert spectrum," *IEEE Sensors J.*, vol. 18, no. 18, pp. 7560–7569, Sep. 2018.
- [10] D. L. Donoho, "Compressed sensing," *IEEE Trans. Inf. Theory*, vol. 52, no. 4, pp. 1289–1306, Apr. 2006.
- [11] H. Mamaghanian, N. Khaled, D. Atienza, and P. Vandergheynst, "Compressed sensing for real-time energy-efficient ECG compression on wireless body sensor nodes," *IEEE Trans. Biomed. Eng.*, vol. 58, no. 9, pp. 2456–2466, Sep. 2011.
- [12] A. M. R. Dixon, E. G. Allstot, D. Gangopadhyay, and D. J. Allstot, "Compressed sensing system considerations for ECG and EMG wireless biosensors," *IEEE Trans. Biomed. Circuits Syst.*, vol. 6, no. 2, pp. 156–166, Apr. 2012.
- [13] D. Craven, B. McGinley, L. Kilmartin, M. Glavin, and E. Jones, "Compressed sensing for bioelectric signals: A review," *IEEE J. Biomed. Health Inform.*, vol. 19, no. 2, pp. 529–540, Mar. 2015.
- [14] D. Romero, D. D. Ariananda, Z. Tian, and G. Leus, "Compressive covariance sensing: Structure-based compressive sensing beyond sparsity," *IEEE Signal Process. Mag.*, vol. 33, no. 1, pp. 78–93, Jan. 2016.
- [15] D. Romero and G. Leus, "Compressive covariance sampling," in *Proc. Inf. Theory Appl. Workshop (ITA)*, Feb. 2013, pp. 1–8.
- [16] D. Romero, R. López-Valcarce, and G. Leus, "Compression limits for random vectors with linearly parameterized second-order statistics," *IEEE Trans. Inf. Theory*, vol. 61, no. 3, pp. 1410–1425, Mar. 2015.
- [17] M. H. Hayes, *Statistical Digital Signal Processing and Modeling*. New York, NY, USA: Wiley, 1996.
- [18] C. Park, H. Shin, and B. Lee, "Blockwise PPG enhancement based on time-variant zero-phase harmonic notch filtering," *Sensors*, vol. 17, no. 4, p. 860, 2017.
- [19] N. I. Cho and S. U. Lee, "On the adaptive lattice notch filter for the detection of sinusoids," *IEEE Trans. Circuits Syst. II, Analog Digit. Signal Process.*, vol. 40, no. 7, pp. 405–416, Jul. 1993.
- [20] A. L. Goldberger, L. A. N. Amaral, L. Glass, J. M. Hausdorff, P. C. Ivanov, R. G. Mark, J. E. Mietus, G. B. Moody, C.-K. Peng, and H. E. Stanley, "PhysioBank, PhysioToolkit, and PhysioNet: Components of a new research resource for complex physiologic signals," *Circulation*, vol. 101, no. 23, pp. e215–e220, Jun. 2000.
- [21] A. Shcherbina, C. M. Mattsson, D. Waggett, H. Salisbury, J. W. Christle, T. Hastie, M. T. Wheeler, and E. A. Ashley, "Accuracy in wrist-worn, sensor-based measurements of heart rate and energy expenditure in a diverse cohort," *J. Pers. Med.*, vol. 7, no. 2, p. 3, May 2017.



**CHANKI PARK** received the B.S. degree in control and instrumentation engineering from the Seoul National University of Science and Technology, Seoul, South Korea, in 2011, and the M.S. degree from the School of Mechatronics, Gwangju Institute of Science and Technology (GIST), Gwangju, South Korea, in 2014, where he is currently pursuing the Ph.D. degree with the School of Mechanical Engineering. His current research interests include compressive sensing and biomedical signal processing.



**BOREOM LEE** graduated from the Seoul National University College of Medicine, Seoul, South Korea. He received the M.D. degree, in 1998 and the Ph.D. degree in biomedical engineering from Seoul National University, in 2007. He joined the faculty of the Gwangju Institute of Science and Technology (GIST), in 2011, where he is currently an Associate Professor with the Department of Biomedical Science and Engineering (BMSE). His current research interests include brain connectomics, healthcare systems, biomedical signal processing and instrumentation, and machine learning application in medical research areas.

Received September 4, 2018, accepted September 27, 2018, date of publication October 29, 2018,  
date of current version December 27, 2018.

Digital Object Identifier 10.1109/ACCESS.2018.2876763

# MIMO Antennas for Smart 5G Devices

**NOSHERWAN SHOAIB<sup>1</sup>, (Senior Member, IEEE), SULTAN SHOAIB<sup>ID2</sup>,**

**RIQZA Y. KHATTAK<sup>3</sup>, IMRAN SHOAIB<sup>ID2</sup>,**

**XIAODONG CHEN<sup>ID2</sup>, (Fellow, IEEE), AND AQIB PERWAIZ<sup>4</sup>**

<sup>1</sup>Research Institute for Microwave and Millimeter-Wave Studies, National University of Science and Technology, Islamabad 44000, Pakistan

<sup>2</sup>School of Electronic Engineering and Computer Science, Queen Mary University of London, London E1 4NS, U.K.

<sup>3</sup>Department of Electrical Engineering, HITEC University, Taxila 47080, Pakistan

<sup>4</sup>College of Electrical and Mechanical Engineering, National University of Science and Technology, Islamabad 44000, Pakistan

Corresponding author: Noshwan Shoaib (noshwan.shoaib@seecs.edu.pk)

This work was funded through Higher Education Commission (HEC), Pakistan Start-Up Research Grant Program Project no. 1319, titled “Design and Fabrication of 5G MIMO Antenna for Mobile Communication.”

**ABSTRACT** This paper presents the design of  $8 \times 8$  multiple-input multiple-output (MIMO) antennas for future 5G devices, such as smart watches and dongles. Each antenna of the MIMO configuration occupies  $3 \times 4 \text{ mm}^2$  and is printed on the top layer of the substrate in the form of a rotated H-shaped patch. The substrate used for the design is a  $31.2 \times 31.2 \times 1.57 \text{ mm}^3$ , Rogers RT-5880 board, with a dielectric constant of 2.2. The top layer of the substrate has eight MIMO antennas, whereas the bottom layer is composed of ground plane. The ground plane is an electromagnetic bandgap-based structure designed for the enhancement of gain and efficiency. Each antenna is fed from the bottom layer of the substrate through vias to avoid any spurious radiation. The MIMO antennas resonate at 25.2 GHz with a 6-dB percentage bandwidth of 15.6%. The gain attained by the antennas in the entire bandwidth is above 7.2 dB with a maximum value of 8.732 dB at the resonant frequency. Likewise, the value of efficiency attained by the antennas in the entire bandwidth is above 65% with a maximum value of 92.7% at the resonant frequency. The simulation and measurement results have substantiated a good performance of the MIMO antennas, thus making them suitable for compact 5G devices.

**INDEX TERMS** 5G, EBG, high gain, MIMO, smart watch.

## I. INTRODUCTION

With an increase in the number of users the frequency allocation is getting deficient due to limited channel bandwidth. Within in the same frequency bandwidth the number of users cannot exceed a specified limit. Also, the co-channel interference increases with an increase in number of users. After the evolution of high definition (HD) and quadruple high definition (QHD) video resolutions, it becomes quite difficult for the handheld devices to send or receive large volume videos on the 3G and 4G frequency channels. It thus becomes a necessity to have a wider bandwidth and a faster data rate for rapid transmission and reception of high quality multimedia wirelessly from one terminal to the other. To cater for this problem, 5G frequencies are under research due to their wider bandwidth. 5G offers greater bandwidth with more number of frequency channels as compared to 3G and 4G thus making it suitable for increased number of users who demand fast data rate on the go [1]. Besides its impressive features, 5G frequencies face a potential problem related to the low penetration power due to which the signal fades and gets weaker while reaching from transmitter to receiver using one antenna at each end. In order to enhance the range of the transmitted

signal, Multiple Input Multiple Output (MIMO) and/or array antennas can be a better solution especially when dealing with compact battery powered devices [2], [3]. Few designs of compact 5G antennas have been presented in [4]–[22]. It has been observed from the review that the antennas presented are mostly single antennas and few array antennas as it is very difficult to achieve high gain using a single antenna. The array antennas, however, being fed through single port have the same capacity performance as that of single antennas. Due to this reason, the frequency channel is busy most of the time thus reducing data transfer rate. Also, the proposed antennas possess poor bandwidth thus limiting the number of frequency channels. Another issue associated with the 5G designs, presented in the literature, is that the antennas are mostly not in MIMO configuration which makes them unsuitable for devices demanding a high data rate and throughput performance. An H-shaped antenna is presented by Kuo and Wong [23] for WLAN frequencies. The design covers dual band. However, it is not MIMO antenna, thus not suitable for high date rate smart devices. It is therefore a strong need to develop the MIMO antennas for 5G devices so that a higher data rate and a wider bandwidth can be made possible.

In this paper we present a printed MIMO antenna system for future smart 5G devices such as smart watches and dongles etc. The design presents eight similar antennas etched on the front of a Rogers RT-5880 substrate board. Each antenna of the MIMO system is a rotated H-shaped patch and covers a wide bandwidth for future 5G communication. The geometry of the proposed 5G MIMO antennas and their simulation and measurement results will be discussed in the upcoming sections.

## II. ANTENNA DESIGN

The MIMO antennas are modelled and simulated in CST Microwave Studio® [24], as presented in figure 1, whereas, the fabricated prototype is presented in figure 2.

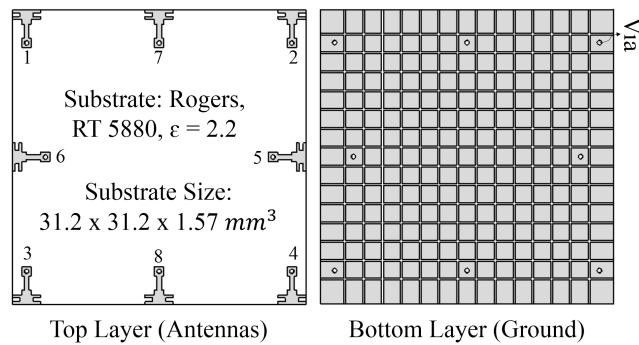


**FIGURE 1.** Simulated model of the 5G MIMO Antennas. (Front View: Top Layer; Back View: Bottom Layer).

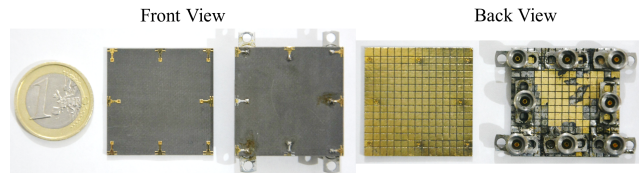


**FIGURE 2.** Fabricated prototype of the 5G MIMO antennas.

It can be seen from figure 1 that the design is comprised of eight H-shaped MIMO antennas printed on the top layer of Rogers RT-5880 board whereas, the bottom layer is composed of an EBG based ground plane which consists of slots each having a width of 0.2 mm. Each antenna has a microstrip feed line that is fed from the back through via hole to minimize spurious radiations. The RF coaxial connectors used in the fabricated prototype are 2.92 mm type female connectors. The simulations have been carried out at the Research Institute for Microwave and Millimeter-Wave Studies (RIMMS), National University of Science and Technology (NUST), Pakistan, whereas, the testing of the antennas is performed in the antenna laboratory at Beijing University of Posts and Telecommunications (BUPT), China. The proposed design is composed of four antennas at the corner and four at the center. The results of one of the corner antennas and one of the center antennas are presented for the ease of analysis. The results of only antenna # 1 and antenna # 5 are presented as the other antennas are similar to these. It can be anticipated that few discrepancies may incur between the simulation and

measurement results mainly due to soldering of RF connectors which extend outside ground boundary.

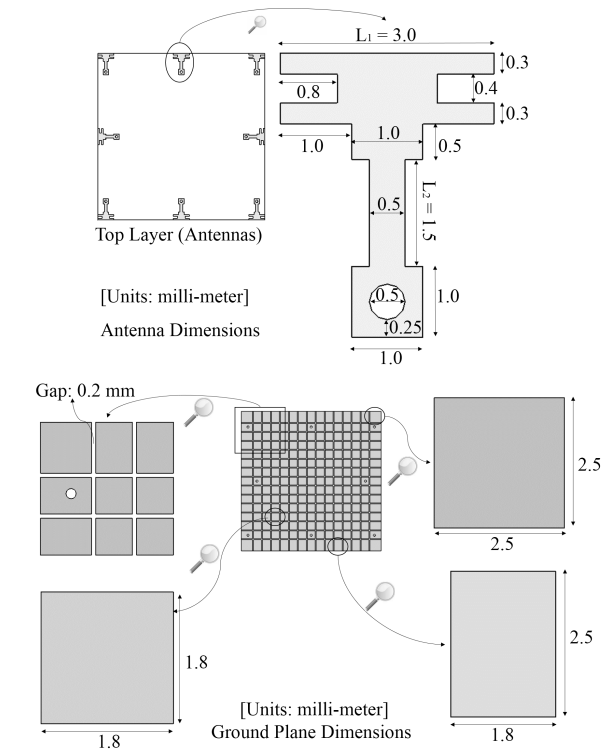


**FIGURE 3.** Detailed dimensions of the proposed MIMO antennas for smart 5G devices.

The detailed dimensions of the antennas and the ground plane are shown in figure 3. It can be seen that the size of the substrate used for the design is  $31.2 \times 31.2 \times 1.57 \text{ mm}^3$  which fits well within the housing of smart device as smart watch or internet dongle. The geometry of each antenna resembles a rotated H-shaped patch, which along with its feed line occupies a space of  $3 \times 4 \text{ mm}^2$  which makes it suitable small handheld future 5G devices. The via-holes drilled for the purpose of feeding have a diameter of 0.5 mm. The horizontal edge-to-edge spacing between the antennas is 11.1 mm which is approximately  $0.93\lambda$  at 25 GHz. Likewise, the vertical edge-to-edge spacing is 10.1 mm which is approximately  $0.84\lambda$  at 25 GHz. The dimensions of the antennas and the ground plane are optimized to achieve better s-parameter and radiation performances. The simulations have shown that the H-shaped patch gives a wider 6 dB bandwidth as compared to a rectangular patch.

The dimensions of the proposed H-shaped patch antenna are smaller than most of the designs from the literature. Also, the dimensions of the proposed MIMO configuration are smaller than other 8-element MIMO antennas. The MIMO antennas presented in this work are confined to a small area, whereas, most of the 5G MIMO designs are not confined to a small area thus making them not suitable to be implemented in current devices. The proposed design, with few modifications, can thus be etched within 3G/4G devices where we

have relatively large spacing (approaching half wavelength) between MIMO antennas.

### III. RESULTS AND DISCUSSIONS

This section will present and compare the simulation and measurement results of the 5G MIMO antennas.

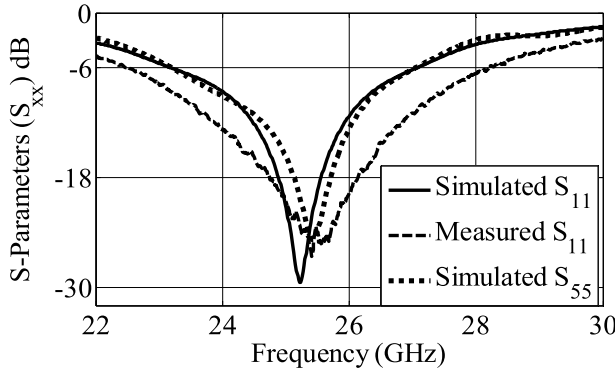


**FIGURE 4.** Simulated and measured  $S_{XX}$  of the proposed 5G MIMO antennas.

#### A. S-PARAMETERS ( $S_{XX}$ & $S_{XY}$ )

The S-parameters of the 5G MIMO antennas are presented in figure 4, wherein, the parameter  $S_{XX}$  represents the reflection loss of the antennas. The  $S_{XX}$  curves are shown for only antenna # 1 and antenna # 5, as all the other antennas are identical to these and are symmetrically placed. It can be seen that the antenna # 1 and antenna # 5 possess almost identical reflection coefficients in simulations due to which measurement result for only antenna # 1 is shown. For practical antennas with a compact profile, the bandwidth is usually defined with reference to  $S_{XX}$  value of  $-6$  dB whereas, for normal antennas it is usually defined with respect to  $-10$  dB. The antennas presented in this paper are compact and cover a very small geometry due to which the bandwidths are defined at  $-6$  dB mark. It can be seen that the antennas are resonating at approximately 25.2 GHz with a simulated bandwidth of 4.1 GHz (23.1 – 27.2 GHz) whereas, in the measurements, the antennas are resonating at 25.4 GHz with a bandwidth of 5.68 GHz. The antennas are thus covering 5G frequency band which ranges from 24.25 – 27.5 GHz [25]. A minor discrepancy has been observed between the simulation and measurement results which occurred mainly due to the substrate tolerances and fabrication imperfections.

The  $S_{XY}$  curves of the MIMO antennas are shown in figure 5. The  $S_{XY}$  parameter represents the isolation between individual elements. It was observed while simulations and measurements that the antennas possess an isolation performance better than 15 dB over the entire frequency bandwidth. The simulated minimum value of  $S_{XY}$  is 16.21 dB, whereas, the measured minimum is 16.19 dB.

#### B. CURRENT DISTRIBUTION

The simulated current distributions of the MIMO antennas are shown in figure 6. The current distribution element 5 is different from that of element 1 due to their different positions

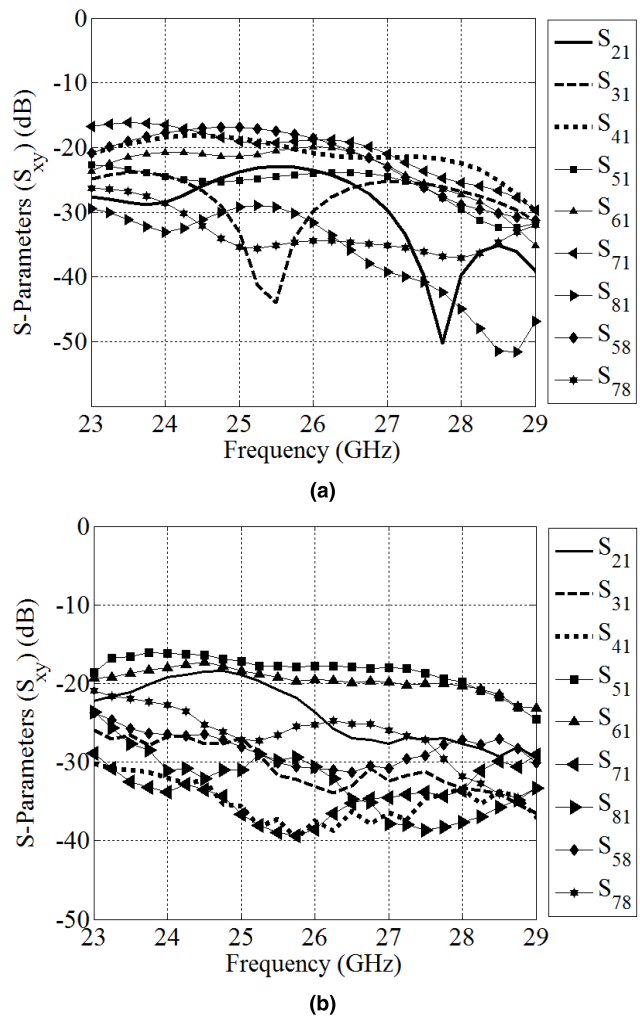


**FIGURE 5.**  $S_{XY}$  of the proposed 5G MIMO antennas. (a): Simulation results. (b): Measurement results.

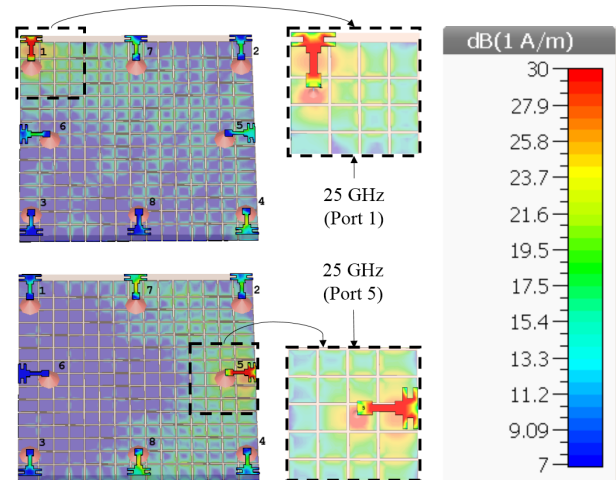


**FIGURE 6.** Surface current distributions of the 5G MIMO antennas.

on the substrate board. The antenna # 1 lies on the corner whereas, antenna # 5 lies between the other two antennas thus resulting in both elements having different radiation patterns.

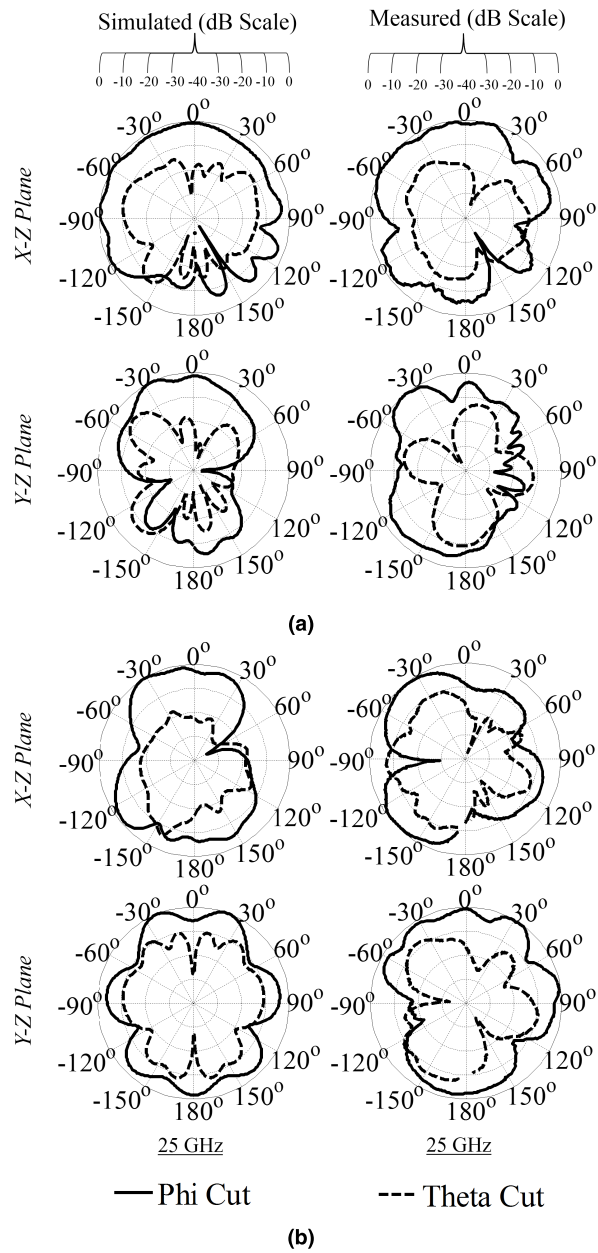


**FIGURE 7.** Radiation patterns of the MIMO antennas for smart 5G devices. (a): Polar patterns for antenna # 1 (b): Polar patterns for antenna # 5.

### C. RADIATION PATTERN

The simulated and measured radiation patterns of the 5G MIMO antennas at 25 GHz are shown in figure 7. The radiation patterns of only Antenna # 1 and Antenna # 5 are shown as other antennas are identical to these and are symmetrically placed. It can be seen that the antennas demonstrate an approximately directional radiation pattern. A discrepancy has been observed between simulation and measurement patterns which may have incurred due to soldering of SMA connectors as the housing of the connectors extends outside ground boundary. This might have been avoided if pig-tail connectors were used.

### D. GAINS & EFFICIENCIES

The gains and efficiencies of the MIMO antennas at different frequencies are shown in table 1. Gain is computed by the ‘Gain comparison method’ using standard gain Horn antenna [26], whereas, for the measurement of efficiency ‘Wheeler Cap method’ is used [27]. Some discrepancies have been observed between the simulated and the measured values which are mainly due to the imperfections in the fabrication of the antenna especially the flange connectors which extend outside ground boundary. The average difference between the simulated and measured gain of Antenna # 1 is 1.41 dB whereas, that for efficiency is 14.2 %. Similarly, the average difference between the simulated and measured gain of Antenna # 5 is 1.05 dB whereas, that for efficiency is 12.9 %.

**TABLE 1.** Gains and efficiencies of MIMO antennas for 5G devices.

Frequency	Gain (dB)		Efficiency (%)	
	Simulated Ant.1/Ant.5	Measured Ant.1/Ant.5	Simulated Ant.1/Ant.5	Measured Ant.1/Ant.5
23 GHz	7.21	6.45	5.85	5.45
24 GHz	7.86	7.44	6.41	6.24
25 GHz	8.73	7.43	7.17	6.41
26 GHz	8.22	6.74	6.77	5.63
27 GHz	7.22	6.52	5.97	5.38

**TABLE 2.** A comparison with the literature designs.

Published Work From Literature	No. of Ports	Bandwidth (GHz)	Average Gain (dB)
Mahmoud et. al. [31]	04	0.53	8 dB
Yevhen et. al [32]	01	0.60	6 dB
Ming et. al. [33]	12	0.20	3.5 dB
Wei et. al. [34]	01	2.20	2.2 dB
Proposed Design	08	5.68	6.4 dB

### E. PERFORMANCE COMPARISON

The gain and efficiency performance of the MIMO antennas is better than most of the 8-Element MIMO antennas in the literature [28]–[30]. Also, the design covers a smaller area than most of the designs which makes it distinctive and more suitable for small wearable and portable devices. Moreover, the MIMO configuration with eight rotated H-shaped patch antennas is rare and will give a better capacity and throughput performance than the other 2-element and 4-element MIMO antennas in the literature. A comparison with other 5G designs from the literature, [31]–[34], is illustrated in table 2. It can be seen that the proposed antenna gives a good value of gain over a wider bandwidth compared to the other designs included in the comparison.

### IV. MIMO PERFORMANCE ANALYSIS

The key parameters that have been studied for analyzing the MIMO performance of the proposed antennas include envelope correlation coefficient (ECC), mean effective gain (MEG) and effective diversity gain (EDG). Each parameter will be discussed in this section.

#### A. ENVELOPE CORRELATION COEFFICIENT (ECC)

The ECC curves between different MIMO pairs are shown in figure 8. The ECC values have been approximated using the S-parameters method [35]. It can be seen from the curves that in the bandwidth of 23 – 27 GHz, the relatively larger values of correlation coefficients exist between antenna 1 & antenna 5, antenna 1 & antenna 7 and antenna 6 & antenna 7. The peak value of correlation coefficient is 0.03 which is much smaller than the practically acceptable value. From figure 5, it is obvious that the measured  $S_{XY}$  is better than simulated  $S_{XY}$  which means that the measured correlation coefficients will be better than the simulation ones.

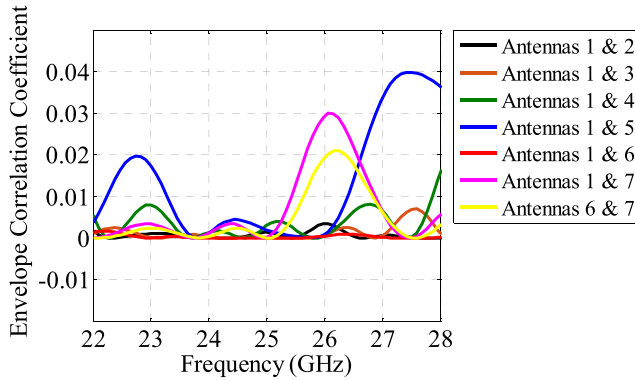


**FIGURE 8.** Envelope correlation coefficients of the proposed MIMO antennas for smart 5G devices.

**TABLE 3.** Simulated mean effective gains (MEG) of the 5G antennas.

Freq. (GHz)	#1	#2	#3	#4	#5	#6	#7	#8
23	4.85	4.78	4.75	4.81	4.28	4.29	4.28	4.28
24	4.04	4.12	4.17	4.19	3.71	3.76	3.73	3.74
25	3.34	3.37	3.36	3.39	3.47	3.42	3.41	3.39
26	3.68	3.73	3.67	3.68	4.01	3.97	4.03	4.02
27	4.41	4.46	4.44	4.42	4.65	4.64	4.63	4.62

#### B. MEAN EFFECTIVE GAIN (MEG)

The simulated and measured values of mean effective gain of the proposed 5G MIMO antennas are calculated using the efficiency method [36], and are shown in Table 3-4. It can be seen that the antennas possess good values of MEG which happened primarily due to a better isolation between MIMO antennas. Also, the ratios of MEG of different elements are approximately equal to 1 which validate a good diversity performance of the MIMO antennas. The measured mean effective gains are slightly smaller than the simulated ones. This is primarily due to substrate tolerances, fabrication and testing imperfections.

#### C. EFFECTIVE DIVERSITY GAIN (EDG)

The effective diversity gain of the proposed 5G MIMO antennas is calculated using the method presented in [37] and [38]. The diversity gain thus calculated ranges from 13.05 dB to 18.54 dB with an average value of 15.8 dB. The 5G antennas

**TABLE 4.** Measured mean effective gains (MEG) of the 5g antennas.

Freq. (GHz)	MEG (-dB) of Antenna Element No.							
	#1	#2	#3	#4	#5	#6	#7	#8
23	5.91	5.86	5.93	5.81	5.13	5.07	5.10	5.03
24	4.83	4.79	4.86	4.74	4.42	4.36	4.25	4.39
25	4.07	4.00	4.13	3.99	4.41	4.38	4.29	4.40
26	4.44	4.36	4.49	4.35	4.86	4.79	4.72	4.80
27	5.44	5.31	5.51	5.36	5.47	5.33	5.41	5.39

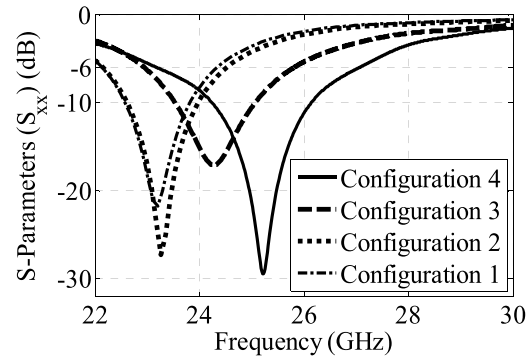


**FIGURE 9.** S-Parameter ( $S_{xx}$ ) of the different configurations of the proposed 5G MIMO antennas.

present a good diversity performance however, at the corner frequencies, the diversity performance is relatively poor which primarily happened due to lower efficiency values. This can be improved by employing efficiency enhancement techniques. For the calculation of the EDG, average value of correlation coefficients from figure 8 are used to analyze an average diversity performance.

#### V. PARAMETRIC ANALYSIS

A detailed parametric analysis was performed on different parameters of the MIMO design. The analysis was performed on antenna element 1 for the ease of understanding. The effect of variation of each parameter will be discussed in this section.

#### A. STEP-WISE DESIGN APPROACH

The design of the MIMO antennas proposed in this paper is composed of eight similar H-shaped patch antennas printed on the top layer of the substrate that comprises of an EBG based ground plane. This type of ground plane in the design improves its gain and reflection coefficient. The design can thus be divided into different configurations to understand the step-wise approach. Configuration 1 shows a single antenna (at the corner) with simple ground plane, configuration 2 shows single antenna (at the center) with simple ground plane, configuration 3 shows 8 antennas with simple ground plane, whereas, configuration 4 shows 8 antennas with EBG ground plane. The S-parameters of each configuration are shown in figure 9 whereas, the gain performance is shown in figure 10.

It can be seen that the EBG ground plane provides much better reflection performance as compared to a simple ground plane. Also, the gain performance of the configuration 4 is much better than the other configurations.

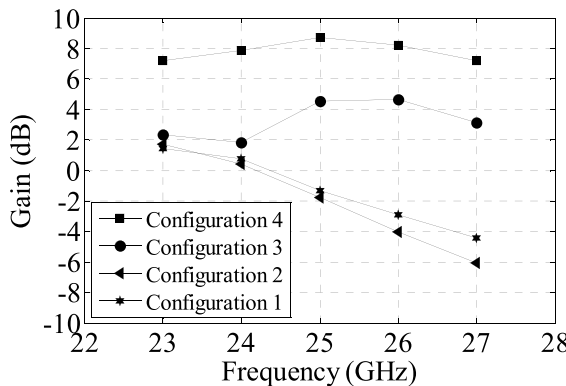


**FIGURE 10.** Gain performance of the different configurations of the proposed 5G MIMO antennas.

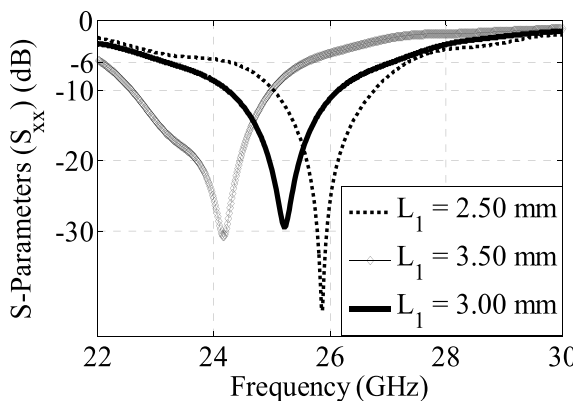


**FIGURE 11.** Effect of parameterization of the length ' $L_1$ ' on the S-Parameter ( $S_{xx}$ ) of the proposed 5G MIMO antennas.

### B. LENGTH ' $L_1$ '

The length ' $L_1$ ' in the design defines the resonant frequency and bandwidth at which MIMO antennas are operating. The value of parameter  $L_1$  is set at 3 mm. By increasing this length, the resonant frequency shifts to a lower value and vice versa, as can be seen from the  $S_{xx}$  curves in figure 11. The length  $L_1$  is optimized at 3 mm as at this value the MIMO antennas resonate at 25 GHz with a wider frequency bandwidth as compared to other values.

### C. LENGTH ' $L_2$ '

The parameter ' $L_2$ ' affects the resonant frequency and impedance matching in the design. By decreasing the length  $L_2$ , the resonant frequency shifts to a higher value and vice versa. It can be seen from the efficiency curves in figure 12 that at 25 GHz, the impedance matching is poor for  $L_2 = 1$  mm as well as for  $L_2 > 1.5$  mm. The parameter  $L_2$  is thus optimized at 1.5 mm as it gives an excellent efficiency and a better impedance matching at 25 GHz.

## VI. CONCLUSION

A design of  $8 \times 8$  MIMO antennas was presented for 5G communication. The antennas demonstrated a compact geometry and a wide bandwidth of 4 GHz ranging from

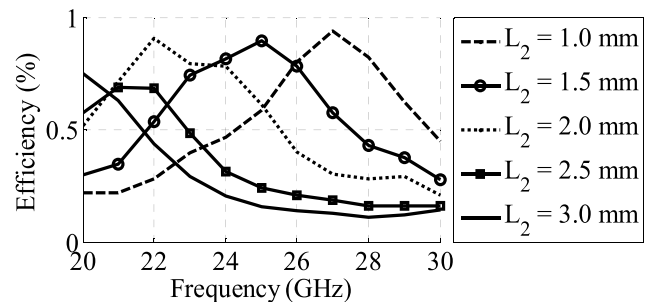


**FIGURE 12.** Effect of parameterization of the length ' $L_2$ ' on the total efficiency of the proposed 5G MIMO antennas.

23.1 – 27.2 GHz. There has been observed a good agreement between the simulation and the measurement results. The design presented in this paper displayed good return loss and radiation performances thus making it suitable for future 5G devices such as smart watches and dongles etc. Reduction in the size of the substrate, improvements in the fabrication of the antennas and measurements with new dimensions, will be a part of immediate future work.

## ACKNOWLEDGEMENT

The authors would like to thank Prof. Yuan Yao from BUPT, China, for his support in fabrication and testing of the design. This work was funded through Higher Education Commission (HEC), Pakistan Start-Up Research Grant Program Project no. 1319, titled "Design and Fabrication of 5G MIMO Antenna for Mobile Communication."

## REFERENCES

- [1] A GSA Executive Report from Ericsson, Huawei and Qualcomm, "The road to 5G: Drivers, applications, requirements and technical development," Global Mobile Suppliers Assoc., Ericsson, Stockholm, Sweden, GSA Executive Rep., Nov. 2015.
- [2] J. Sharony. (Nov. 15, 2006). *Introduction to Wireless MIMO—Theory and Applications*. [Online]. Available: [https://ieeeli/pdf/viewgr-aphs/introduction\\_to\\_wireless\\_mimo.pdf](https://ieeeli/pdf/viewgr-aphs/introduction_to_wireless_mimo.pdf)
- [3] J. P. Bevelacqua, "Antenna arrays: Performance limits and geometry optimization," Ph.D. dissertation, Arizona State Univ., Tempe, AZ, USA, May 2008. [Online]. Available: <http://www.antenna-theory.com/Bevelacqua-Dissertation.pdf>
- [4] D. Sarkar and K. V. Srivastava, "Compact four-element SRR-loaded dual-band MIMO antenna for WLAN/WiMAX/WiFi/4G-LTE and 5G applications," *Electron. Lett.*, vol. 53, no. 25, pp. 1623–1624, 2017.
- [5] L. Zhu, H. S. Hwang, E. Ren, and G. Yang, "High performance MIMO antenna for 5G wearable devices," in *Proc. IEEE Int. Symp. Antennas Propag. USNC/URSI Nat. Radio Sci. Meeting*, San Diego, CA, USA, Jul. 2017, pp. 1869–1870.
- [6] G. Oliveri et al., "Design of compact printed antennas for 5G base stations," in *Proc. 11th Eur. Conf. Antennas Propag. (EUCAP)*, Paris, France, Mar. 2017, pp. 3090–3093.
- [7] W. Hong, K. Baek, and Y. Lee, "Quantitative analysis of the effects of polarization and pattern reconfiguration for mmWave 5G mobile antenna prototypes," in *Proc. IEEE Radio Wireless Symp. (RWS)*, Phoenix, AZ, USA, Jan. 2017, pp. 68–71.
- [8] J. Park, J. Ko, H. Kwon, B. Kang, B. Park, and D. Kim, "A tilted combined beam antenna for 5G communications using a 28-GHz band," *IEEE Antennas Wireless Propag. Lett.*, vol. 15, pp. 1685–1688, 2016.
- [9] J.-S. Park, J.-B. Ko, H.-K. Kwon, B.-S. Kang, B. Park, and D. Kim, "Millimeter-wave tiny lens antenna employing U-shaped filter arrays for 5G," *IEEE Antennas Wireless Propag. Lett.*, vol. 17, no. 5, pp. 845–848, May 2018.

- [10] S. X. Ta, H. Choo, and I. Park, "Broadband printed-dipole antenna and its arrays for 5G applications," *IEEE Antennas Wireless Propag. Lett.*, vol. 16, pp. 2183–2186, 2017.
- [11] J. Holopainen, J.-M. Hannula, and V. Viikari, "A study of 5G antennas in a mobile terminal," in *Proc. 11th Eur. Conf. Antennas Propag. (EUCAP)*, Paris, France, Mar. 2017, pp. 3079–3081.
- [12] W. Hong, K.-H. Baek, and S. Ko, "Millimeter-wave 5G antennas for smartphones: Overview and experimental demonstration," *IEEE Trans. Antennas Propag.*, vol. 65, no. 12, pp. 6250–6261, Dec. 2017.
- [13] W. Hong, K.-H. Baek, Y. Lee, Y. Kim, and S.-T. Ko, "Study and prototyping of practically large-scale mmWave antenna systems for 5G cellular devices," *IEEE Commun. Mag.*, vol. 52, no. 9, pp. 63–69, Sep. 2014.
- [14] K. M. Mak, H. W. Lai, K. M. Luk, and C. H. Chan, "Circularly polarized patch antenna for future 5G mobile phones," *IEEE Access*, vol. 2, pp. 1521–1529, 2014.
- [15] Q. W. Lin, H. Wong, X. Y. Zhang, and H. W. Lai, "Printed meandering probe-fed circularly polarized patch antenna with wide bandwidth," *IEEE Antennas Wireless Propag. Lett.*, vol. 13, pp. 654–657, 2014.
- [16] C. H. Kuo, C. C. Lin, and J. S. Sun, "Modified microstrip Franklin array antenna for automotive short-range radar application in blind spot information system," *IEEE Antennas Wireless Propag. Lett.*, vol. 16, pp. 1731–1734, 2017.
- [17] K. R. Mahmoud and A. M. Montaser, "Performance of tri-band multi-polarized array antenna for 5G mobile base station adopting polarization and directivity control," *IEEE Access*, vol. 6, pp. 8682–8694, 2018.
- [18] Q.-X. Chu, X.-R. Li, and M. Ye, "High-gain printed log-periodic dipole array antenna with parasitic cell for 5G communication," *IEEE Trans. Antennas Propag.*, vol. 65, no. 12, pp. 6338–6344, Dec. 2017.
- [19] R. Hussain, A. T. Alreshaid, S. K. Podilchak, and M. S. Sharawi, "Compact 4G MIMO antenna integrated with a 5G array for current and future mobile handsets," *IET Microw. Antennas Propag.*, vol. 11, no. 2, pp. 271–279, 2017.
- [20] B. Yang, Z. Yu, Y. Dong, J. Zhou, and W. Hong, "Compact tapered slot antenna array for 5G millimeter-wave massive MIMO systems," *IEEE Trans. Antennas Propag.*, vol. 65, no. 12, pp. 6721–6727, Dec. 2017.
- [21] M. S. Sharawi, M. Ikram, and A. Shamim, "A two concentric slot loop based connected array MIMO antenna system for 4G/5G terminals," *IEEE Trans. Antennas Propag.*, vol. 65, no. 12, pp. 6679–6686, Dec. 2017.
- [22] H. W. Lai and H. Wong, "Substrate integrated magneto-electric dipole antenna for 5G Wi-Fi," *IEEE Trans. Antennas Propag.*, vol. 63, no. 2, pp. 870–874, Feb. 2015.
- [23] Y.-L. Kuo and K.-L. Wong, "Printed double-T monopole antenna for 2.4/5.2 GHz dual-band WLAN operations," *IEEE Trans. Antennas Propag.*, vol. 51, no. 9, pp. 2187–2192, Sep. 2003.
- [24] M. Rütschlin, (May 18–19, 2011). *Antenna Simulation Overview*. Computer Simulation Technology, 3D Electromagnetic Simulation Software. [Online]. Available: [https://www.cst.com/content/events/downloads/eugm2011/talk\\_3-1-1\\_cst\\_ugm\\_2011.pdf](https://www.cst.com/content/events/downloads/eugm2011/talk_3-1-1_cst_ugm_2011.pdf)
- [25] Ericsson, "5G radio access, capabilities and technologies," Ericsson, White Paper Uen 284 23-3204 Rev C, Apr. 2016. [Online]. Available: <https://www.ericsson.com/assets/local/publications/white-papers/wp-5g.pdf>
- [26] C. A. Balanis, *Antenna Theory: Analysis and Design*, 3rd ed. Hoboken, NJ, USA: Wiley, 2005.
- [27] D. M. Pozar and B. Kaufman, "Comparison of three methods for the measurement of printed antenna efficiency," *IEEE Trans. Antennas Propag.*, vol. AP-36, no. 1, pp. 136–139, Jan. 1988.
- [28] M. U. Khan and M. S. Sharawi, "A compact 8-element MIMO antenna system for 802.11ac WLAN applications," in *Proc. Int. Workshop Antenna Technol. (iWAT)*, Karlsruhe, Germany, 2013, pp. 91–94.
- [29] A. A. Reguna, T. Hariyadi, A. B. Pantjawati, and E. A. Juanda, "Design and simulation of omnidirectional MIMO microstrip antenna at 1.8 GHz for LTE applications," in *Proc. Int. Conf. Radar, Antenna, Microw., Electron., Telecommun. (ICRAMET)*, Jakarta, Indonesia, 2016, pp. 85–89.
- [30] X. Hua, D. Wu, S. W. Cheung, and Q. L. Li, "A planar 8-port MIMO antenna for 2.4-GHz WLAN applications," in *Proc. IEEE Int. Symp. Antennas Propag. USNC/URSI Nat. Radio Sci. Meeting*, San Diego, CA, USA, Jul. 2017, pp. 1653–1654.
- [31] K. R. Mahmoud and A. M. Montaser, "Synthesis of multi-polarised upside conical frustum array antenna for 5G mm-Wave base station at 28/38 GHz," *IET Microw. Antennas Propag.*, vol. 12, no. 9, pp. 1559–1569, 2018.
- [32] Y. Yashchyshyn et al., "28 GHz switched-beam antenna based on S-PIN diodes for 5G mobile communications," *IEEE Antennas Wireless Propag. Lett.*, vol. 17, no. 2, pp. 225–228, Feb. 2018.
- [33] M.-Y. Li, Y.-L. Ban, Z.-Q. Xu, J. Guo, and Z.-F. Yu, "Tri-polarized 12-antenna MIMO array for future 5G smartphone applications," *IEEE Access*, vol. 6, pp. 6160–6170, 2018.
- [34] W. Lin, R. W. Ziolkowski, and T. C. Baum, "28 GHz compact omnidirectional circularly polarized antenna for device-to-device communications in the future 5G systems," *IEEE Trans. Antennas Propag.*, vol. 65, no. 12, pp. 6904–6914, Dec. 2017.
- [35] R. G. Vaughan and J. B. Andersen, "Antenna diversity in mobile communications," *IEEE Trans. Veh. Technol.*, vol. VT-36, no. 4, pp. 149–172, Nov. 1987.
- [36] M. P. Karaboisikis, V. C. Papamichael, G. F. Tsachtsiris, C. F. Soras, and V. T. Makios, "Integrating compact printed antennas onto small diversity/MIMO terminals," *IEEE Trans. Antennas Propag.*, vol. 56, no. 7, pp. 2067–2078, Jul. 2008.
- [37] K. Fijimoto and J. R. James, *Mobile Antenna Systems Handbook*. Norwood, MA, USA: Artech House, 2000.
- [38] S. Shoaib. (May 2016). *MIMO Antennas for Mobile Handsets and Tablet Application*. [Online]. Available: <https://qmro.qmul.ac.uk/xmlui/handle/123456789/12921>



**NOSHERWAN SHOAIB** (SM'18) received the master's degree in electronics engineering and the Ph.D. degree in electronics and electrical measurements engineering from the Politecnico di Torino, Italy, in 2011 and 2015, respectively. He was a Post-Doctoral Research Fellow with the Istituto Nazionale di Ricerca Metrologica, Italy, and the Petroleum Institute University and Research Center, United Arab Emirates. He is currently an Assistant Professor with the Research Institute for Microwave and Millimeter-Wave Studies, National University of Sciences and Technology, Islamabad. He teaches RF and microwave related courses to electrical engineering students. He contributed to a patent, two books, and more than 45 leading international technical journals, peer-reviewed conference papers, and technical reports. His current research interests include RF energy harvesting, Internet of Things, RF metrology and design and development of 5G multiple-input multiple-output antennas, and microwave active circuits.

Dr. Shoaib is the Founder and the Chair of Pakistan's first ever IEEE joint Microwave Theory and Techniques, Antenna and Propagation and Electromagnetic Compatibility/Interference Chapter. He was elected as an Early Career Representative of the International Union of Radio Science (URSI) Commission-A in 2017. He was a recipient of the Best Ph.D. Graduate Award in 2015, the 4th International URSI Student Paper Competition in 2015, the ARFTG Ph.D. Student Sponsorship Award in 2013, the Best National Senior Year Graduate Project Gold Medal Award in 2010, and the President of Pakistan Gold Medal Award in 2008. He received the Young Scientist Awards from URSI at multiple occasions.



**SULTAN SHOAIB** received the Ph.D. degree from the Queen Mary University of London, U.K., in 2016. He is currently an Assistant Professor with the Department of Electrical Engineering, HITEC University, Taxila, Pakistan. He is also involved in collaborative research at the Queen Mary University of London, the University of Bedfordshire, Luton, U.K., and the National University of Science and Technology, Pakistan. His research interests include designing and testing multiple-input multiple-output and array antennas for satellite, mobile handsets, and future 5G terminals.



**RIQZA Y. KHATTAK** received the B.Sc. degree in electrical (electronics) engineering from COMSATS, Abbottabad, Pakistan, in 2015. Since 2015, she has been involved in research on antennas and wave propagation. She is currently the M.Sc. degree in electrical engineering with HITEC University, Taxila, Pakistan. Her M.Sc. thesis dissertation is on multiple-input multiple-output antennas for future 5G terminals.



**XIAODONG CHEN** is currently a Professor of microwave engineering with the School of Electronic Engineering and Computer Science, Queen Mary University of London, London, U.K. He is also the Director of the Joint Research Laboratory on Electromagnetic Theory and Applications, Queen Mary University of London and Beijing University of Posts and Telecommunications. He has co-authored two textbooks, over 100 journal papers, and 300 refereed conference papers. His research interests include microwave and THz antennas and devices, wireless communications, and bio-electromagnetics.



**IMRAN SHOAIB** received the B.S. degree in electrical (telecommunication) engineering from COMSATS University, Islamabad, Pakistan, in 2006, and the M.Sc. degree in electronic engineering from the Queen Mary University of London, London, U.K., in 2008, where he is currently pursuing the Ph.D. degree.

His research interests include antenna design for multiple-input multiple-output applications, smart and reconfigurable antenna systems, radio propagation modeling, RF circuit and system design, and aspects of microwave printed circuit design.



**AQIB PERWAIZ** received the Ph.D. degree from the National University of Sciences and Technology, Islamabad, Pakistan. He is currently the Assistant Director of research and development with the College of Electrical and Mechanical Engineering, National University of Sciences and Technology. He has hands on industrial working experience of 23 years and has designed many repair setups for world top ranking companies in Pakistan. He is currently involved in the development of Li polymer power pack systems. His research interests include optimization of software-defined radio modules, reverse engineering, design thinking, and data mining.

• • •